Università degli Studi di Palermo

AREA RICERCA E TRASFERIMENTO TECNOLOGICO
SETTORE DOTTORATI E CONTRATTI PER LA RICERCA
U. O. DOTTORATI DI RICERCA

Dottorato di Ricerca in Scienze Molecolari e Biomolecolari

Dipartimento di Scienze e Tecnologie Biologiche Chimiche e Farmaceutiche (STEBICEF)

SSD CHEM-05/A

A study on molecules promoting the readthrough of nonsense mutations (TRIDs)

IL DOTTORE
Dott. Ignazio Fiduccia

IL COORDINATORE
Prof.ssa Giovanna Pitarresi

IL TUTOR
Prof.ssa Ivana Pibiri

IL CO-TUTOR
Prof. Andrea Pace

CICLO XXXVII

ANNO CONSEGUIMENTO TITOLO 2024

Contents

ABBREVIATIONS

ABD – Actin-binding domain
AP – Adaptor protein
APC- Antigen-presenting cell
BDCP – BEACH domain-containing protein
BKR – Boulton-Katritzky thermal rearrangements
BMD – Becker muscular dystrophy
CBC – Cap binding complex
CF – Cystic Fibrosis
CHMP – Committee for medicinal products for human use
CR – Cysteine-rich
CT – C-terminal
CTL4 – Cytotoxic T-lymphocyte antigen 4
CYP – Cytochrome P450
DAPC – Dystrophin-associated protein complex
DDA – Data dependent acquisition
DDI – Drug-drug interaction
DGC – Dystrophin-glycoprotein complex
DM – Differentiation medium
DMD – Duchenne muscular dystrophy
ECM – Extracellular matrix
EGFR – Epidermal growth factor receptor
eIF3 – eukaryotic initiation factor 3
eIF4E – eukaryotic initiation factor 4E
EJC – Exon junction complex
EMA – European medicines agency
EPS – Electrical pulse stimulation
eRF1 – eukaryotic release factor 1
eRF3 – eukaryotic release factor 3
FTR – Fisher rat thyroid
GDP – Guanosine diphosphate
GGQ – Gly-Gly-Gln motif
GTP – Guanosine triphosphate

HLM – Human liver microsome

HTS – High throughput screening

LFQ – Limit of quantification

LOD – Limit of detection

LRBA – LPS responsive and beige-line anchor

mRNP – messenger ribonucleoprotein

nc-tRNA – near cognate tRNA

NMD – Nonsense mediated decay

nNOS – neuronal nitric oxide synthase

NTC – Natural termination codon

ORF – Open reading frame

PABP – Poly(A)-binding protein

PBMC – Primary peripheral blood mononuclear cell

PH- Pleckstrin homology

PIRD – Primary immune regulatory disorder

PTC - Premature termination codon

ROS – reactive oxygen species

RT – Translational readthrough

SDB – Shwachman-Diamond syndrome

TLC – Thin layer chromatography

Treg – Regulatory T cell

TRID – Translational readthrough inducing drug

UDP – Uridine diphosphate

uORF – Upstream open reading frame

UPF3b – Up-frameshift 3b

UTR – Untranslated region

ABSTRACT

Nonsense mutations account for roughly 11% of genetic diseases by introducing premature termination codons (PTCs) into mRNA sequences, resulting in truncated, non-functional proteins that are rapidly degraded. The aberrant mRNA activates the nonsense-mediated decay (NMD) pathway, reducing mRNA availability and thereby limiting the production of essential proteins.
Currently, there are no cures for genetic disorders associated with PTCs. A striking example of disorder that can be caused by nonsense mutations is Duchenne Muscular Dystrophy (DMD), which result in progressive muscle degeneration. Ataluren (PTC124), a Translational Readthrough Inducing Drug (TRID), is currently the only approved therapy for nonsense derived DMD, as it facilitates readthrough of PTCs, allowing protein synthesis to proceed to the natural termination codon (NTC) and restoring functional dystrophin protein.
In addition to DMD, rare disorders such as LPS Responsive Beige-like Anchor protein (LRBA) deficiency, a condition affecting immune regulation due to non-functional truncated proteins, are also associated with nonsense mutations.
Given the limited effective treatments for these conditions, recent research has focused on developing new TRIDs. Based on Ataluren as a parental drug, several oxadiazole-based TRIDs have been synthesized, showing enhanced readthrough capabilities and potential for use in a wider range of genes impacted by nonsense mutations.
Among these compounds, NV848, NV914, and NV930 demonstrate favorable safety, efficacy, and functionality profiles. Both *in vitro* studies and acute toxicity assessments in wild-type murine models indicate that these new TRIDs are well tolerated, offering promising therapeutic strategy for treating nonsense mutation-related disorders.
This research project aimed to carry on preclinical investigation to assess the potential of three novel TRIDs, NV848, NV914, and NV930, in addressing genetic disorders caused by nonsense mutations, with a specific focus on DMD and LRBA deficiency.
The initial phase of the study involved optimizing the synthesis of the three NV compounds, followed by a comprehensive evaluation of the metabolic stability of NV914 and NV930 in vitro, while the metabolic stability of NV848 had been already assessed. The results indicated that NV914 exhibited significant stability against hepatic metabolism, while NV930 demonstrated a tendency for rapid hydrolysis of its ester bond.
Subsequently, the biodistribution of the three molecules was studied in murine models to better understand their pharmacokinetics.

Furthermore, proteomic analyses were performed on cells harboring nonsense mutations in the LRBA gene to evaluate the overall impact of these three TRIDs on protein expression.
Finally, the project also included the development of a 3D-engineered skeletal muscle model derived from DMD patients, characterized by DMD-specific nonsense mutations, to test the efficacy of TRIDs in restoring dystrophin protein expression.

1 Introduction

1.1 Mendelian rare diseases characterized by nonsense mutations

Mendelian rare diseases constitute a class of genetic disorders caused by mutations in a single gene and follow inheritance patterns first described by Gregor Mendel. Depending on the affected gene and the specific characteristics of the mutation involved, these diseases can be inherited in autosomal dominant, autosomal recessive, or X-linked manners (Kmth and M, 2020).

A mutation can be defined as an alteration in the nucleotide sequence of a gene. When a mutation develops naturally within the cell, it is called spontaneous mutation, and often, that happens due to biochemical events and replication errors. Other times, mutations can be induced by external agents called mutagens, which include both chemical and physical agents, that can cause mutations mainly by acting as base analogs, which means they can be erroneously incorporated into newly synthesized DNA at the replication fork, causing alternations in the DNA sequence or still by interacting directly or indirectly with the DNA, leading to structural changes in the genetic material itself (Merrick et al., 2023).

Genetic diseases are classified as "rare", when they affect fewer than 1 in 2.000 individuals, underlining the limited frequency within the general population (Boycott et al., 2017). Despite their rarity, they often lead to significant morbidity and mortality due to their impact on fundamental biological functions. Among Mendelian rare diseases, those characterized by nonsense mutations are particularly significant at the molecular level, leading to the loss of a functional protein. The clinical manifestations of Mendelian rare diseases characterized by nonsense mutations are highly variable and depend on the specific gene affected and the protein's role within the body. For example, Duchenne muscular dystrophy (DMD) results from nonsense mutations in the dystrophin gene, leading to severe muscle wasting and early mortality. Also, nonsense mutations in the Cystic Fibrosis Transmembrane Conductance Regulator (CFTR) gene cause cystic fibrosis, a condition marked by chronic respiratory infections and pancreatic insufficiency due to defective ion transport across cell membranes. Another example includes nonsense mutation in the LPS-responsive and beige like anchor (LRBA) gene that causes LRBA deficiency, a severe primary immune regulatory disorder (PIRD) (Bladen et al., 2015; Neri et al., 2020; Lopez-Herrera et al., 2012; Wilschanski, 2012; Zhang et al., 2021) (**Figure 1**).

The study of Mendelian rare diseases characterized by nonsense mutations thus represents a crucial area of research, bridging molecular genetics and clinical science.

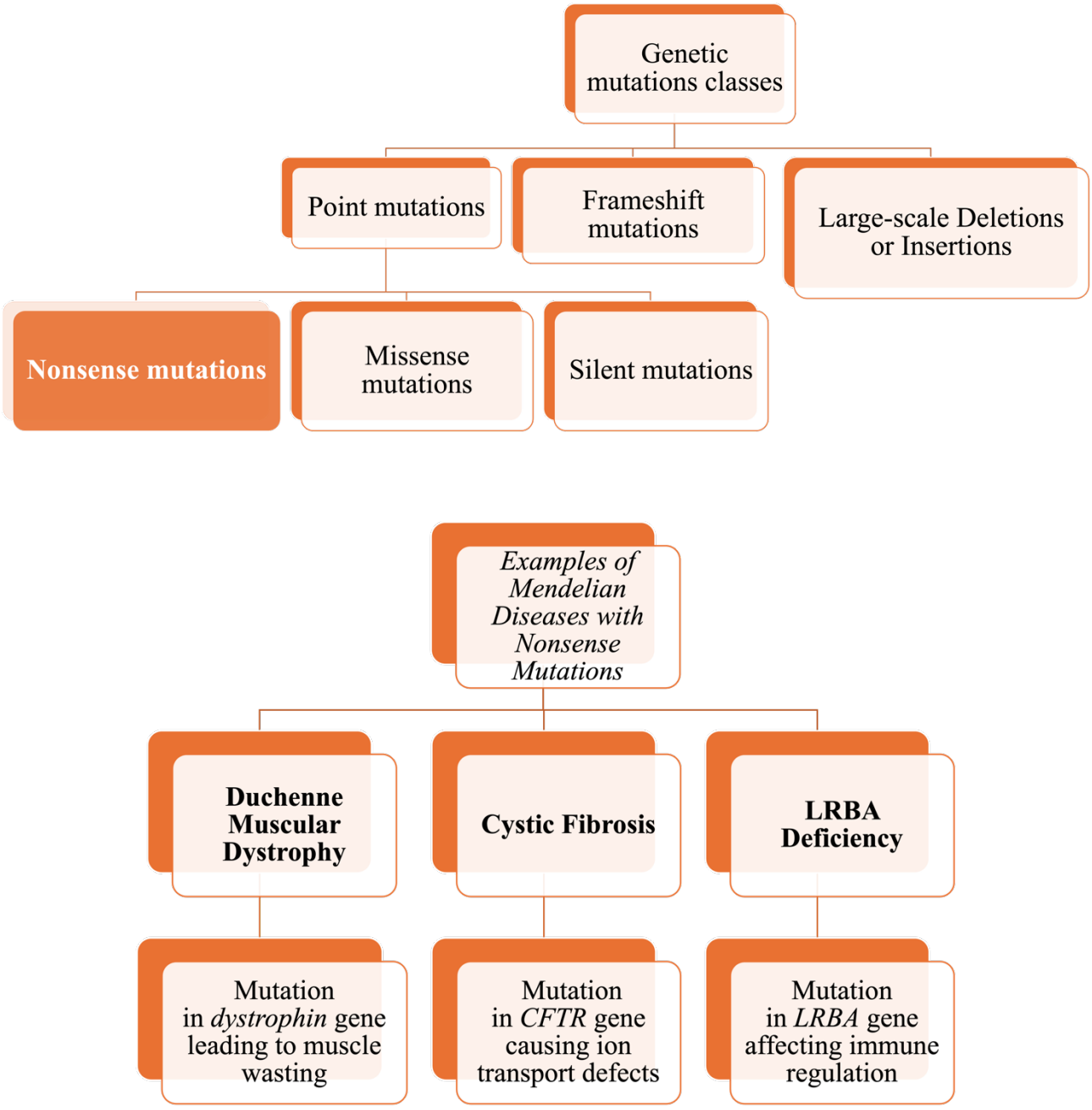

Figure 1. *Type of genetic mutation and examples of mendelian genetic diseases due to nonsense.*

1.2 Nonsense mutations

Nonsense mutations have long posed a formidable challenge in the treatment of genetic disorders. These mutations account for approximately 11% of inherited conditions and about 20% of mutations that involve single-base pair substitutions (Mort et al., 2008; Romanov and Sukhoverov, 2017; Ghelfi et al., 2023).

Nonsense mutations typically arise from a single nucleotide substitution that transforms a codon encoding for an amino acid into one of three stop codons: UAA (ochre), UAG (amber), or UGA (opal). This produces a premature termination codon (PTC) that prematurely stops the translation,

producing an incomplete polypeptide chain. The resulting truncated protein is often non-functional. Moreover, the nonsense-mRNA is quickly broken down by an mRNA surveillance system known as nonsense-mediated decay (NMD) (Frischmeyer and Dietz, 1999), thus preventing the making of possibly harmful abnormal protein and subsequent cellular stress from the unfolded protein response (Walter and Ron, 2011). Besides in-frame mutations, PTCs can also be introduced by frameshift or splicing mutations (Oren et al., 2017; Sanz et al., 2010; Clarke et al., 2019). This can result in a complete loss of protein function (Potapova, 2022). The severity of the phenotype depends on the premature stop codon's location within the gene, with mutations closer to the beginning of the sequence generally having more pronounced effects. This is because mutations near the start of the gene produce shorter, more severely truncated proteins that are less likely to retain functional domains. Conversely, mutations near the end of the gene may generate proteins that maintain some functionality, potentially resulting in milder phenotypes (Potapova, 2022).

Given the severe impact of PTCs on protein function, mechanisms that can bypass these codons, such as translational readthrough, offer potential therapeutic pathways for addressing these mutations.

1.3 Translational Readthrough mechanism

Translational readthrough (RT) is a process where ribosomes bypass a stop codon, continuing translation beyond the normal termination point. Although translation termination at Natural Termination Codon (NTC) is a very efficient process, it can rarely get suppressed with an estimated error of 0.001% to 0.1% in mammalian cells (Floquet et al., 2012). This error increases, going from 0.1% to 1%, in the case of translation termination suppression at PTCs (Keeling et al., 2012).

In eukaryotes, translation termination is triggered by a protein heterodimer consisting of two release factors: eukaryotic release factor 1 (eRF1) and eukaryotic release factor 3 (eRF3) (Bertram et al., 2000; Alkalaeva et al., 2006; Hellen, 2018).

eRF1 resembles a tRNA molecule (Song et al., 2000) that can recognize all three stop codons; it binds to the A-site of the ribosome, through its N-terminal domain, when one of the three stop codons is encountered (Bertram et al., 2000). The eRF1 middle (M) domain contains a highly conserved Gly-Gly-Gln (GGQ) motif that induces the release of the nascent polypeptide from peptidyl-tRNA in the P-site (Frolova et al., 1999) whilst its C-terminal (CT) domain binds to eRF3 (Mantsyzov et al., 2010).

eRF3 is made of a non-conserved N-terminal domain, which can bind to the poly(A)-binding protein (PABP) (Hoshino et al., 1999; Kozlov and Gehring, 2010) and the NMD factor UPF3b (up-frameshift 3b) (Neu-Yilik et al., 2017). eRF3 also contains a Guanosine-triphosphate (GTP)-binding domain, which is essential for binding and hydrolysis of GTP, as well as two β-barrel domains, which are homologous to GTP-binding translation factors (**Figure 2**) (Kong et al., 2004).

When the eRF1 binds to eRF3, the resulting complex displaces any previously bound Guanosine diphosphate (GDP) and increases eRF3's affinity for GTP over GDP by two orders of magnitude (Hauryliuk et al., 2006; Mitkevich et al., 2006). Once eRF3- GTP is hydrolyzed, eRF1 stretches its conformation, bringing the GGQ motif, which is located at the tip of the M-domain, into the peptidyl transferase center (Matheisl et al., 2015; Muhs et al., 2015; Shao et al., 2016). This repositioning of the GGQ motif induces conformational changes, that catalyzes the cleavage of the peptidyl-tRNA ester bond, exposing it to nucleophilic attack by water, and consequently releasing the polypeptide chain from the ribosome (**Figure 2**) (Salas-Marco and Bedwell, 2004).

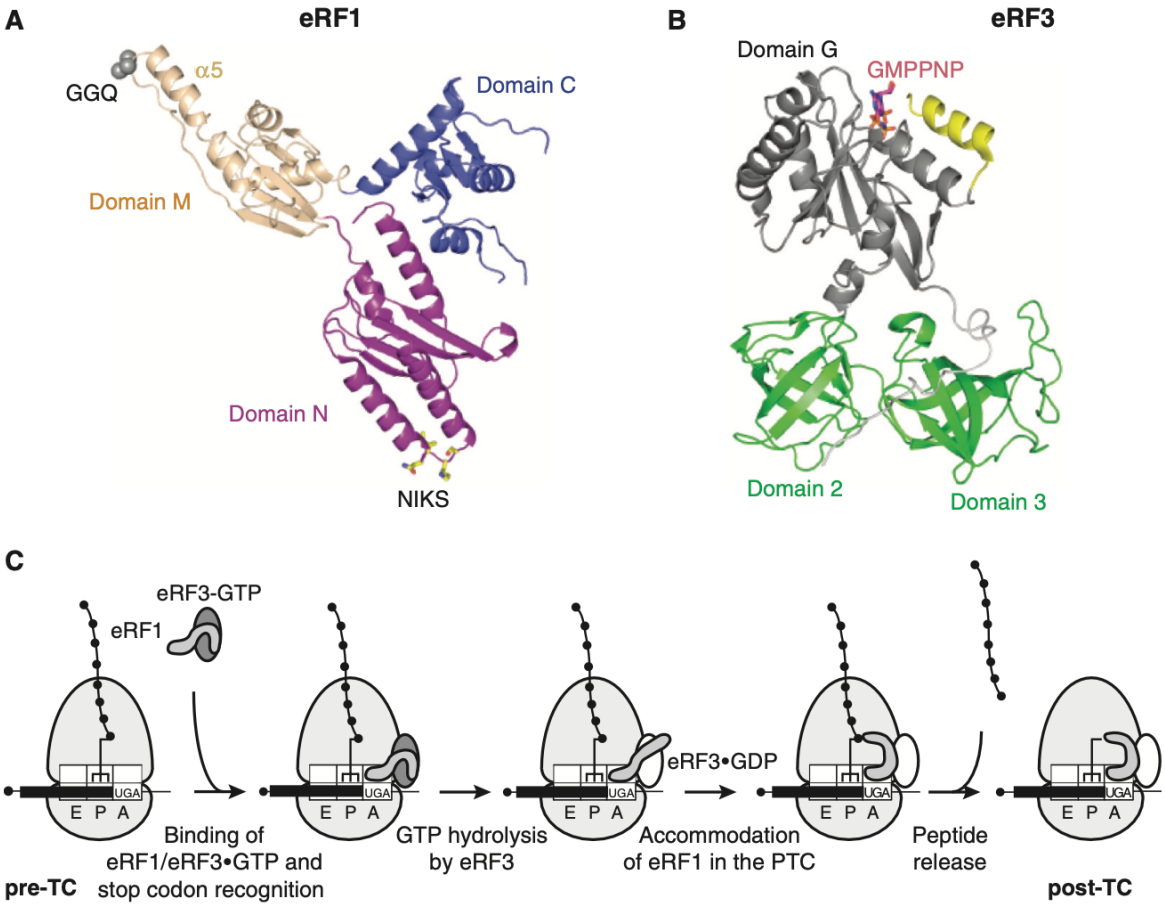

Figure 2. *Translation termination in eukaryotes. (A) structure of human eRF1, (B) structure of eRF3 from Schizosaccharomyces pombe. (C) scheme of termination process (adapted from Hellen, 2018).*

However translational RT can bypass this termination process when competition arises between eRF1, which triggers the proper termination translation upon recognition of a termination codon, and an aminoacyl-tRNA that matches two out of three bases, termed near cognate tRNA (nc-tRNA), in the A-site of the ribosome. This leads to the erroneous insertion of an amino acid into the polypeptide chain, allowing the ribosome to continue translation until it reaches the NTC, thus producing a full-length, functional protein (Dabrowski et al., 2015).

The efficiency of basal RT is mainly influenced by the identity of the stop codon. Depending on the fidelity, the level of readthrough changes greatly, with UGA and UAA showing respectively the highest and the lowest readthrough, while UAG shows an intermediate level (**Figure 3**) (Manuvakhova et al., 2000; Cridge et al., 2018). However, termination efficiency is also influenced by the surrounding sequences both downstream and upstream of the termination codon, with the nucleotide immediately following the stop codon (+4) exerting the strongest influence on RT (Tate and Mannering, 1996; Beryozkin et al., 2023). When Cytosine (C) is present as a +4 nucleotide, the levels of readthrough are higher than when other nucleotides occupy the same position. The order of efficiency from most to least is C>U>A>G (Floquet et al., 2012; Beryozkin et al., 2023), but these findings are controversial since the levels of basal readthrough vary among studies (Bonetti et al., 1995; Kk et al., 1995; Manuvakhova et al., 2000; Beznosková et al., 2015; Beryozkin et al., 2023). The presence of (C) at position +4 did not substantially affect the RT when UAA and UAG stop codons were present in the transcript as PTCs (**Figure 3**) (Manuvakhova et al., 2000; Beryozkin et al., 2023). The formation of mRNA secondary structures, such as stem-loops or pseudoknots, upon interaction with the ribosome, could be a possible explanation of RT (Firth et al., 2011; Wagner et al., 2023).

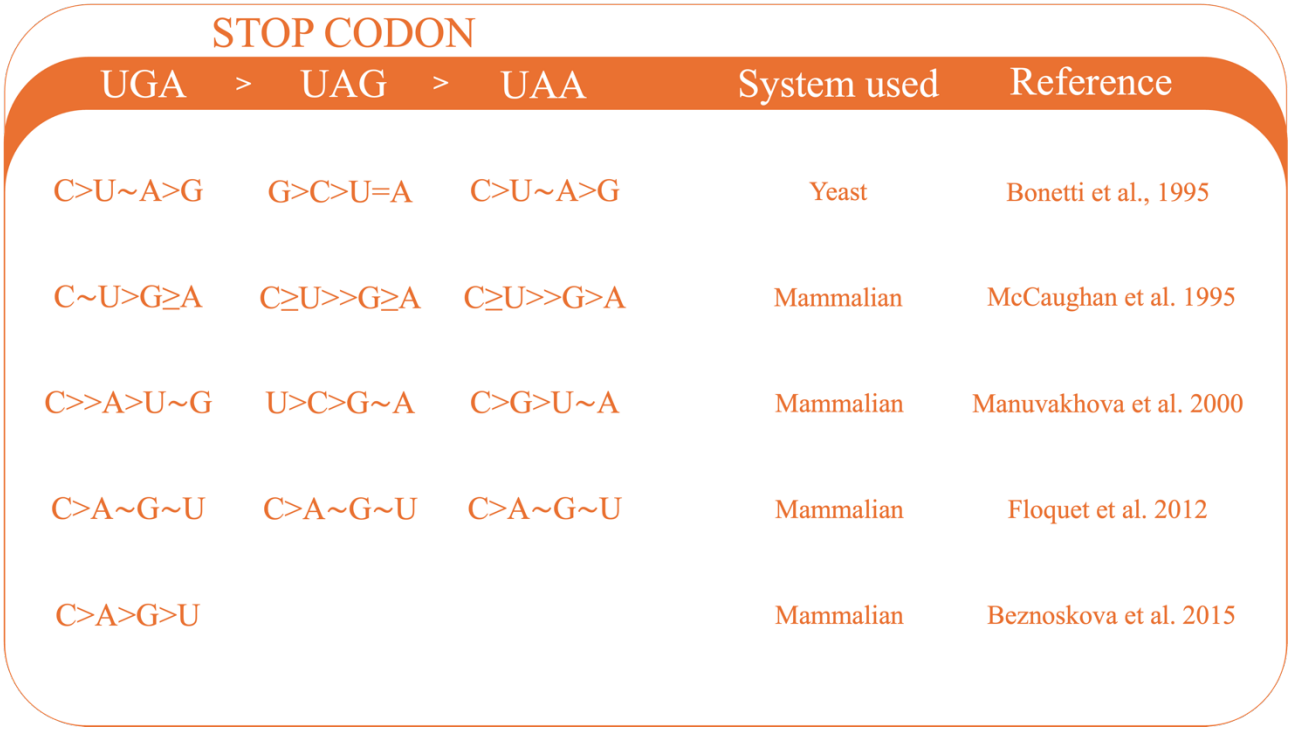

Figure 3. *Termination efficiency influenced by the downstream sequence.*

The presence of adenine (A), or a purine in general, at position -1 or -2 seems to induce RT by modifying the mRNA structure at the P-site, causing structural changes in the ribosome and favoring competition between release factors and natural suppressor tRNAs (**Figure 4**) (Tork et al., 2004; Beryozkin et al., 2023).

Additionally, eukaryotic initiation factor 3 (eIF3) seems to interfere with eRF1, leading to erroneous decoding of the third position of the stop codon set in the adverse termination context, facilitating the insertion of a nc-tRNA (Poncová et al., 2019).

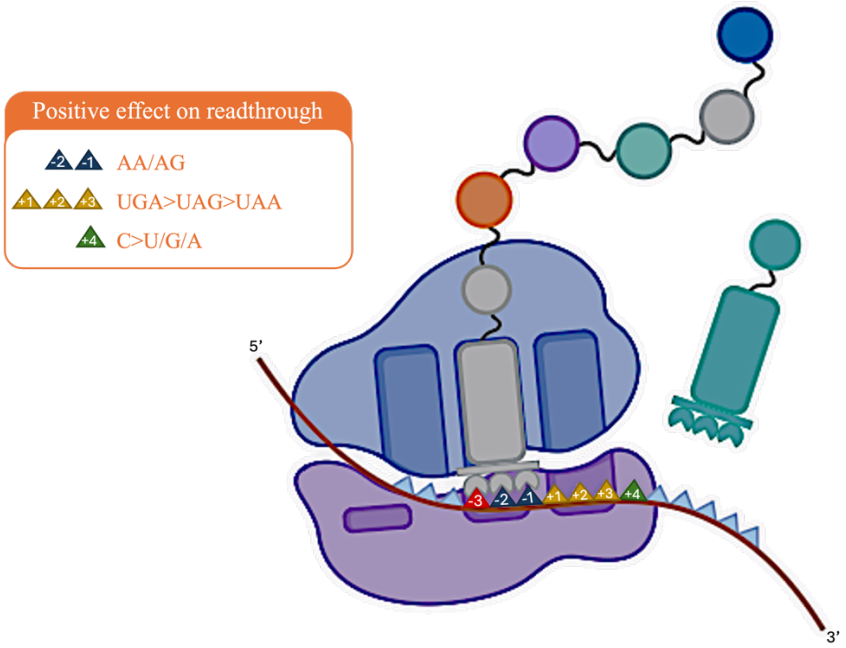

Figure 4. *Factors affecting readthrough during translation. Different positions on the mRNA are marked by numbered triangles. Legend shows higher preference for readthrough.*

The RT mechanism can also be influenced by other factors that are independent of both the type of stop codon and the surrounding mRNA sequence context. These include increased levels of mRNA undergoing termination suppression (Linde et al., 2007; C et al., 2020) or the depletion of key factors such as eRF1 and eRF3 (Carnes et al., 2003; Baradaran-Heravi et al., 2021) or post-translational modification of some ribosomal proteins that affect translational accuracy (Loenarz et al., 2014; Singleton et al., 2014).

1.4 Nonsense-Mediated mRNA Decay

After exploring the complexities of RT, it's important to consider how NMD complements this process. NMD is a cellular surveillance mechanism that identifies and degrades mRNAs containing PTCs, but it is also well established that contributes to the regulation level of gene expression by targeting mRNAs encoding full-length, functional proteins for degradation (Nasif et al., 2018; Karousis and Mühlemann, 2022). Despite being investigated for more than two decades, the mechanism and criteria for the selection of a mRNA for a NMD remain unclear. NMD activation is connected to inefficient translation termination and depends on the messenger ribonucleoproteins (mRNPs) composition on a PTC-containing mRNA. NMD can either occur during the first round of translation, the so-called pioneer round of translation, where mRNA is still associated with the nuclear-cap-binding complex (CBC) (Maquat et al., 2010; Karousis and Mühlemann, 2022) or during later rounds when the CBC is replaced by the eukaryotic initiation

factor 4E (eIF4E) (Durand and Lykke-Andersen, 2013; Rufener and Mühlemann, 2013; Monaghan et al., 2023).

Once an mRNA is marked for NMD, the cell recruits factors to break it down, stopping further translation and ultimately reducing unnecessary or faulty protein synthesis (Monaghan et al., 2023).

The NMD mechanism is enhanced by exon junction complexes (EJCs), which are deposited on RNAs in the nucleus during splicing, generally 20-24 nucleotides upstream of the exon-exon junction (Tø et al., 2005; Karousis and Mühlemann, 2022). The EJCs located in open reading frames (ORFs) are meant to be removed by the ribosome during the first round of translation and those that remain bound to the mRNA, within its ORF or in the 3'untranslated region (UTR), after the beginning of translation, strongly promote the activation of NMD by recruiting NMD factors (**Figure 5**) (Bühler et al., 2006; Metze et al., 2013; Monaghan et al., 2023).

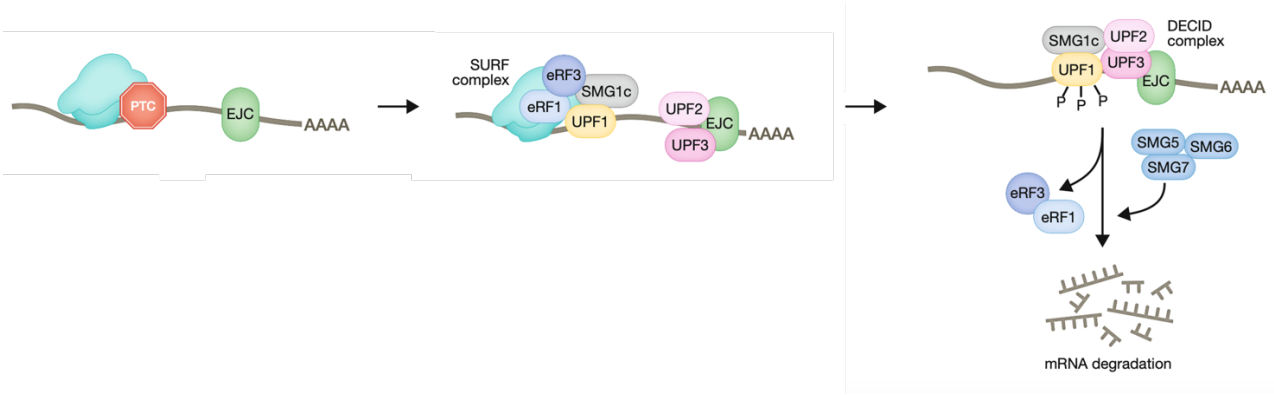

Figure 5. *Schematic representation of NMD activation, leading to the assembly of the SURF complex (adapted from Monaghan et al., 2023).*

Among some gene features that produce transcript prone to NMD, the presence of a PTC at least 50-55 nucleotides upstream of an exon-exon junction is the strongest predictive value for NMD susceptibility (Colombo et al., 2017), while other features that can trigger NMD activation are mRNAs with upstream ORFs (uORF) (Calvo et al., 2009; Monaghan et al., 2023) or still the presence of a long 3'UTR (**Figure 6**) (Hogg and Goff, 2010; Karousis and Mühlemann, 2019).

While the NMD mechanism helps prevent the accumulation of potentially harmful truncated proteins, it can also reduce overall gene expression levels, further contributing to the loss of function.

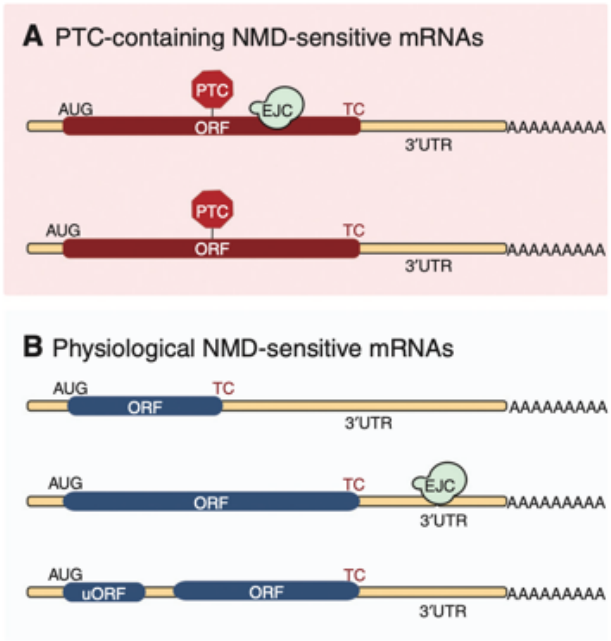

Figure 6. *NMD can be triggered by specific structural features within both abnormal and normal mRNAs. (A) mRNAs containing an ORF that is prematurely terminated by a stop codon are usually prone to NMD. This sensitivity is often increased when EJCs are positioned downstream of the PTC, serving as a signal that promotes NMD. (B) mRNAs with a complete ORF that codes for a full-length protein, certain elements such as long 3' UTRs, EJCs situated in the 3' UTR, or short uORFs can also initiate NMD (adapted from Karousis and Mühlemann, 2019).*

1.5 Therapeutic approaches to nonsense mutations

Considering that basal readthrough acts at a too low extent to give an effect in restoring disease phenotype, attention turns to therapeutic strategies aimed at addressing nonsense mutations. Among therapeutic approaches, translational readthrough-inducing drugs (TRIDs) have emerged as a key focus, aimed at overriding PTCs and enabling the synthesis of functional, full-length proteins (Morais et al., 2024). However, the efficacy of TRIDs is closely tied to their metabolic stability, as drug metabolism influences a compound's bioavailability, therapeutic effectiveness, and potential for side effects. Given the significance of metabolism in relation to TRIDs, the following section explores the fundamentals of drug metabolism, detailing its impact on pharmacological outcomes.

1.6 Fundamental of drug metabolism

Drug metabolism refers to the chemical modification of drugs once they enter the body, primarily occurring to facilitate their excretion and to control their duration and activity within the organism (Patel et al., 2020). Generally, the metabolic process diminishes a drug's therapeutic effects,

though this process is essential in transforming hydrophobic drugs into hydrophilic forms to enable their elimination via urine or bile (Zhao et al., 2021). Without such metabolic changes, lipophilic drugs could persist longer in the body, potentially leading to toxic buildup (Rendic, 2021). Drug metabolism is categorized into two phases that together ensure that drugs are metabolized effectively. Phase I reactions often introduce or uncover functional groups (e.g., -OH, -COOH, -NH2, -SH) on drug molecules through processes such as oxidation, reduction, and hydrolysis. However, if the modified drug is still not fully excretable, it becomes a substrate for Phase II reactions, which involve conjugating these Phase I products with polar compounds. Enzymes such as uridine diphosphate (UDP)-glucuronosyltransferases, sulfotransferases, and glutathione S-transferases mediate these conjugation reactions, further increasing the drug's water solubility. This two-step process enables the body to efficiently transport the drug or its metabolites out of cells, with efflux transporters aiding in cellular excretion (**Figure 7**) (Zhao et al., 2021).

Cytochrome P450 (CYP) enzymes play a dominant role in drug metabolism, being involved in more than 90% of these biochemical reactions. These enzymes exist in various isoforms, with families such as CYP1, CYP2, and CYP3 collectively responsible for the metabolism of nearly 80% of the drugs used in clinical settings. Although the liver is the main site of CYP expression, these enzymes are also found in other organs, such as the kidney, gastrointestinal tract, and skin (Zhao et al., 2021).

CYP enzymes also contribute to variations in individual responses to drugs, as genetic and epigenetic differences, alongside environmental factors like age, diet, and health status, influence CYP activity. Additionally, CYP enzymes can be induced or inhibited by other drugs, which may lead to complex drug-drug interactions (DDIs), as well as drug-gene and drug-gene-environment interactions (Zhao et al., 2021).

Understanding these metabolic processes is essential for developing effective therapeutic strategies. This leads us to the next section, where we explore TRIDs, which aim to overcome nonsense mutations and restore functional protein synthesis.

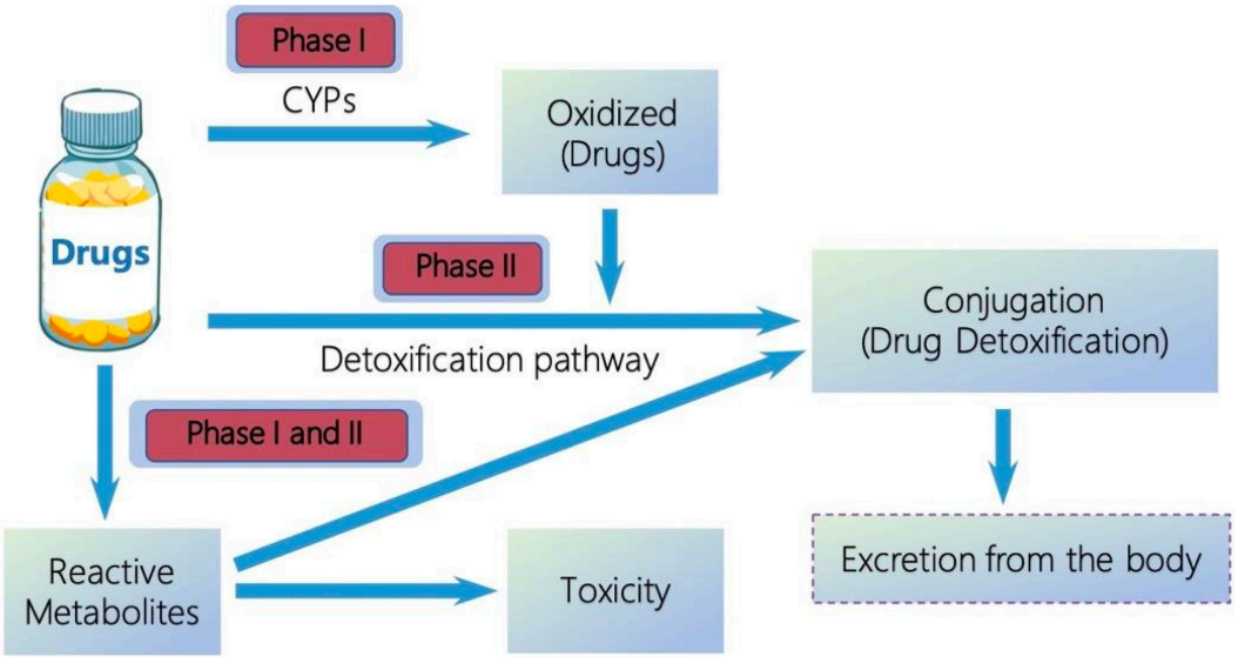

Figure 7. *Metabolic processes in drug clearance (adapted from Zhao et al., 2021).*

1.7 Translational Readthrough Inducing Drugs (TRIDs)

Aminoglycosides antibiotics were the earliest group of compounds identified as being capable of inducing RT in COS-7 cells in 1985, using G418 or paromomycin (Burke and Mogg, 1985; Martins-Dias and Romão, 2021). However, not all aminoglycosides exhibit this property, likely due to variations in their affinity for the ribosomal decoding center in mammalian cells. These antibiotics can be classified in two different groups: the first group includes compounds that have a 4,6-disubstituted-2-deoxystreptamine ring, like gentamicin, G418, tobramycin, etc.; the second group comprises compounds that have a 4,5-disubstituted-2-deoxystreptamine ring, like neomycin and paromomycin (**Figure 8**) (Manuvakhova et al., 2000; Shalev and Baasov, 2014; Martins-Dias and Romão, 2021). Unfortunately, the dosages required for effective RT are often close to those that cause adverse effects such as ototoxicity and nephrotoxicity (Lubamba et al., 2012; Martins-Dias and Romão, 2021). Additionally, patients with diseases caused by nonsense mutations are expected to necessitate lifelong therapy, complicating treatment strategies. Although the precise mechanism behind aminoglycosides toxicity remains unclear, several studies suggest that the endocytic receptor megalin may facilitate the uptake and accumulation of aminoglycosides in the kidney, which is reversible and can be handled with hydration to restore renal function upon treatment interruption (Lopez-Novoa et al., 2011; Martins-Dias and Romão, 2021), and inner ear, where the effects are irreversible and can lead to hearing loss (Xie et al., 2011; Martins-Dias and Romão, 2021).

Aminoglycosides influence several enzymes, leading to off-target effects. They can inhibit phospholipidosis and membrane phospholipases by binding phospholipids in lysosomal membranes. Once endocytosed in lysosomes, aminoglycosides acquire a positive charge due to the acidic pH, allowing them to have a strong interaction with negatively charged phospholipids in the lysosomal membrane. Furthermore, aminoglycosides disrupt eukaryotic protein synthesis during translation, which contributes to their toxic effects (Xie et al., 2011; Martins-Dias and Romão, 2021).

The structural similarity between eukaryotic mitochondrial ribosomes and prokaryotic ribosomes can facilitate the binding of aminoglycosides to the mitochondrial ribosome. This interaction can lead to mitochondrial dysfunction, increasing toxicity and resulting in various side effects (Hobbie et al., 2008; Martins-Dias and Romão, 2021). Moreover, aminoglycosides alter Ca^{2+} levels in the mitochondria, contributing to the formation of reactive oxygen species (ROS) (Jiang et al., 2017).

Cystic Fibrosis (CF) is the first genetic disease in which the ability of aminoglycosides to induce RT was tested. Thus, G418 and gentamicin proved to suppress nonsense mutations in the CFTR gene, leading to the translation of a full-length, functional protein (Howard et al., 1996; Bedwell et al., 1997). G418 binds to the 80S ribosome, therefore altering the translation machinery and inhibiting the elongation cycle of protein synthesis (Bar-Nun et al., 1983; Martins-Dias and Romão, 2021).

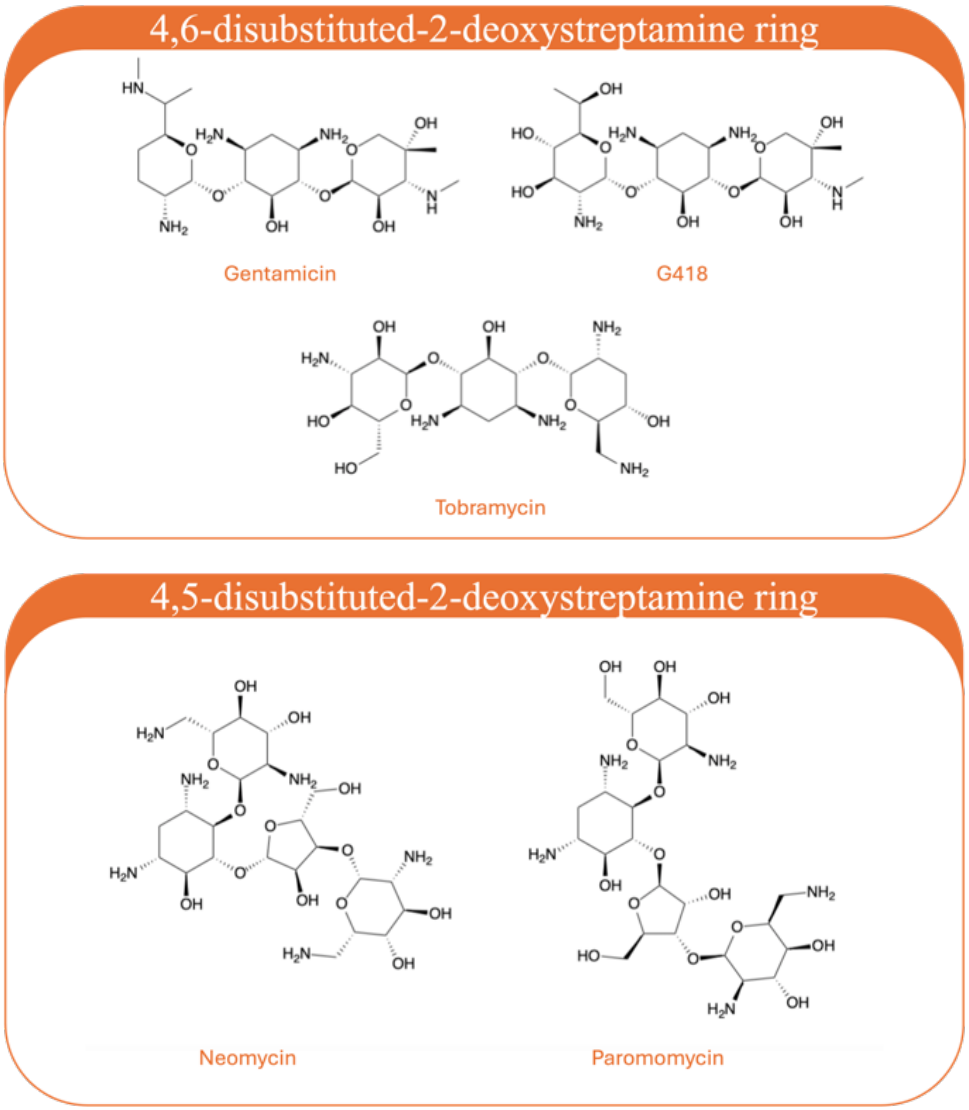

Figure 8. *Classification of antibiotics based on their chemical structures.*

Besides toxicity, an additional problem of aminoglycosides is the development of antibiotic resistance when administered chronically. A new generation of synthetic aminoglycoside derivatives were developed to overcome these issues. Among them, NB124, also known as ELX-02, (**Figure 9**) showed very low renal toxicity and ototoxicity in healthy humans, broader safety range of use and higher potency compared to the first generation of aminoglycoside antibiotics (Leubitz et al., 2019; Brasell et al., 2019; Bezzerri et al., 2020). It underwent clinical trials, reaching Phase II in combination with Ivacaftor, for class I CF patients, but failed to achieve statistical significance for efficacy endpoints. High concentrations of the drug in the kidneys prompted Eloxx Pharmaceuticals to conduct a pivotal study in Alport Syndrome, a rare kidney disease, but it was suddenly cancelled on September 2024 ("Study Details | A Study of ELX-02 in Patients With Alport Syndrome | ClinicalTrials.gov," n.d.).

Other novel not-related aminoglycosides compounds, named RTC13 and RTC14 (**Figure 9**), came out of high throughput screening (HTS) assays and later tested in *mdx* mice. RTC13 showed to partly restore dystrophin protein expression (Kayali et al., 2012; Martins-Dias and Romão, 2021).

Additionally, a molecule capable of RT is 2,6-Diaminopurine (DAP) (**Figure 9**) that displays advantageous pharmacokinetic properties, including stability in plasma and broad distribution throughout the body. Studies indicate that DAP can successfully rectify nonsense mutations in the CFTR gene, restoring its function in various experimental systems, including organoids derived from mouse and patient cells (Leroy et al., 2023).

Another RT compound is Amlexanox (**Figure 9**), which promotes RT and partially inhibits the NMD pathway. This anti-allergic and anti-inflammatory drug has been on the market for over three decades (Saijo et al., 1985; Meng et al., 2009; Martins-Dias and Romão, 2021), but its efficacy in restoring full-length protein, even in combination with other agents, remains limited (McHugh et al., 2020).

A noteworthy TRID is represented by PTC124 (**Figure 9**), also known as Ataluren, which does not share the structural or mechanistic characteristics of aminoglycosides. Unlike aminoglycosides, which primarily target the ribosome and can exhibit significant toxicity, PTC124 works through a distinct mechanism while reducing the risk of off-target effects and toxicity (Hirawat et al., 2007; Huang et al., 2022). Originally identified through a luciferase-based HTS of >800.000 low molecular weight candidates by PTC Therapeutics, PTC124 is diaryl-1,2,4-oxadiazole that has demonstrated efficacy in suppressing nonsense mutations both *in vitro,* using primary muscle cell cultures from DMD patients, and *in vivo* in *mdx* mice (Welch et al., 2007). Another study showed that PTC124 can efficiently suppress the CFTR-G542X nonsense mutation in a CF mouse model expressing a human CFTR-G542X transgene, restoring significant amounts of functional human CFTR protein and chloride channel activity, through subcutaneous or oral administration (Du et al., 2008). Ataluren is primarily metabolized through glucuronidation rather than CYP enzymes, with UGT1A9 being the main enzyme involved. The kidneys play a significant role in its metabolism, showing greater activity than the liver (Kong et al., 2020b). A different study confirmed that its primary metabolite in plasma is Ataluren acyl glucuronide, which is also the predominant metabolite in human urine, while feces contained oxadiazole cleavage products (Kong et al., 2020a). These positive results enabled Ataluren to advance to clinical trials for both CF and DMD. Unfortunately, it did not meet the clinical criteria for CF (Kerem et al., 2014), but in July 2014, it received conditional marketing authorization by the European Union, becoming the first and only available drug on the market for the treatment of

nonsense mutation causing DMD, under the name of Translarna®. Ten years later, the Committee for Medicinal Products for Human Use (CHMP) concluded that Translarna® benefit-risk balance was negative, therefore it did not approve for its renewal (June 2024). It is the responsibility of the EMA to forward the CHMP's opinion to the European Commission, which then will issue a final legally binding decision that affects all EU Member States ("Translarna | European Medicines Agency (EMA)," 2014).

Despite its turbulent fate, Ataluren has shown potential as a groundbreaking treatment for DMD caused by nonsense mutation, distinguished by its high safety profile and easy administration.

The fluctuating results obtained with ataluren and the lack of a readthrough therapy for diseases caused by nonsense mutations like CF and others, prompted the search for new TRID compounds to fill this therapeutic gap driving to the discovery of the following three molecules: the 3acetylamino-5-methyl-1,2,4-oxadiazole (NV848), the 3-pentafluorobenzoylamino-5-perfluorophenyl-1,2,4-oxadiazole (NV914), and the ethyl 5-phenyl-1,2,4-oxadiazole-3-carboxylate (NV930); these were identified through a HTVS process and exhibited promising preliminary results (**Figure 9**).

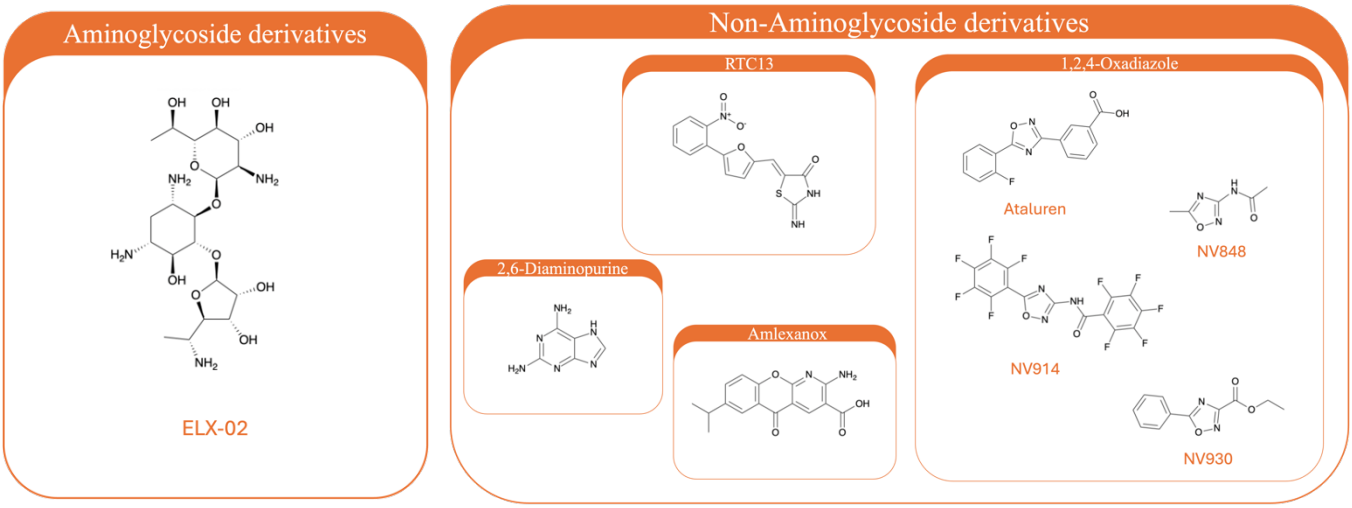

Figure 9. *Readthrough compound grouped based on their structural similarities.*

1.7.1 Exploring the potential of NV848, NV914, and NV930 in nonsense mutation effects rescue

1,2,4-Oxadiazoles are heterocyclic compounds featuring a five-membered aromatic ring with two nitrogen atoms and one oxygen atom. The 1,2,4 configuration is peculiar, due to its favorable electronic properties, contributing to moderate aromaticity and distinctive reactivity. These compounds are synthesized mainly through two methods: the [3+2] cycloaddition of nitriles with

nitrile oxides (**Figure 10a**). and the [4+1] cyclization involving amidoximes and carboxylic acids or their derivatives (**Figure 10b**).

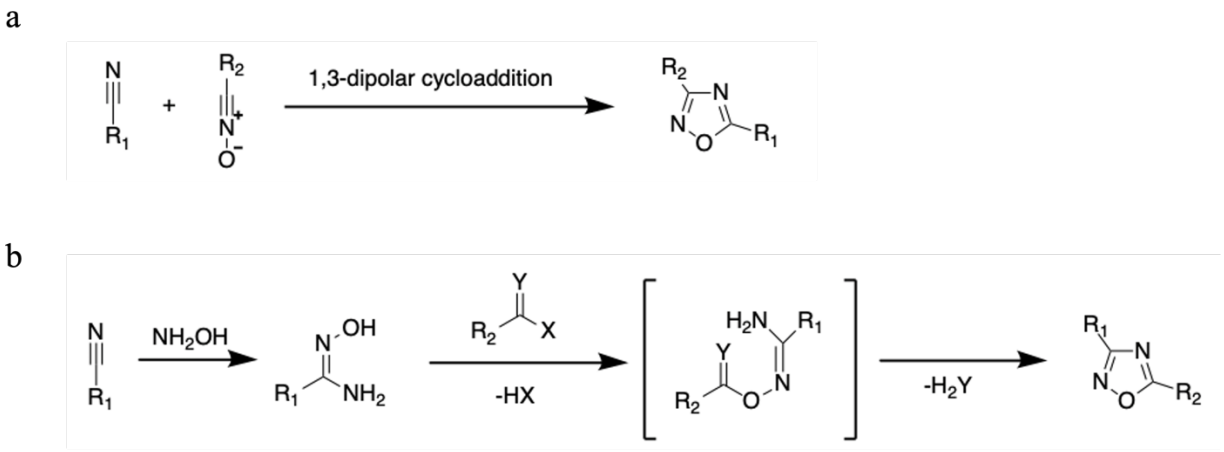

Figure 10. *(a) schematic representation of 1,3-dipolar cycloaddition [3+2]. (b) Schematic representation of amidoxime route [4+1].*

These structural features of 1,2,4-oxadiazoles are further enhanced by the polar and cleavable oxygen-nitrogen bond, which enables them to participate in thermal and photochemical transformations. Such compounds are known for undergoing processes like nucleophilic aromatic substitution (SNAr) and Boulton-Katritzky thermal rearrangements (BKR), leading to the formation of other heterocyclic systems. The [4+1] synthetic approach is preferred in medicinal chemistry due to its compatibility with different substituents at the 3- and 5- positions, which can significantly influence the compound's biological properties (Piccionello et al., 2017).

Given the versatility and functionalization capabilities of the [4+1] pathway, it is widely used in the synthesis of pharmacologically active oxadiazoles. Following an *in silico* screening guided by a validated pharmacophore model, NV848, NV914, and NV930 emerged as promising candidates, ranking in the top 5% of hits. These compounds underwent rigorous preclinical toxicity assessments, beginning with an MTT assay in Fisher Rat Thyroid (FRT) cells to measure viability over 24 and 72 hours, testing three different concentrations: 12 µM, 24 µM and 48 µM. Results indicated that NV848 and NV914 showed no significant cytotoxic effects at either time point across all three concentrations, while NV930 demonstrated a modest reduction in cell viability after 72 hours at both 24 µM and 48 µM (Pibiri et al., 2020). Further validation using zebrafish embryos confirmed the minimal toxicity of NV848 (**Figure 11a**) (Bezzerri et al., 2022). These compounds were then subjected to *in vivo* acute toxicity testing in a murine model, where neither NV848 nor NV930 produced adverse effects at doses up to 300 mg/kg over a two-week period. NV914 inhibited high tolerability even at 2000 mg/kg. Histological analyses aligned with

these observations, as no pathological changes were detected in the treated mice, supporting the high safety profile of these compounds (**Figure 11b**)(Corrao et al., 2022).

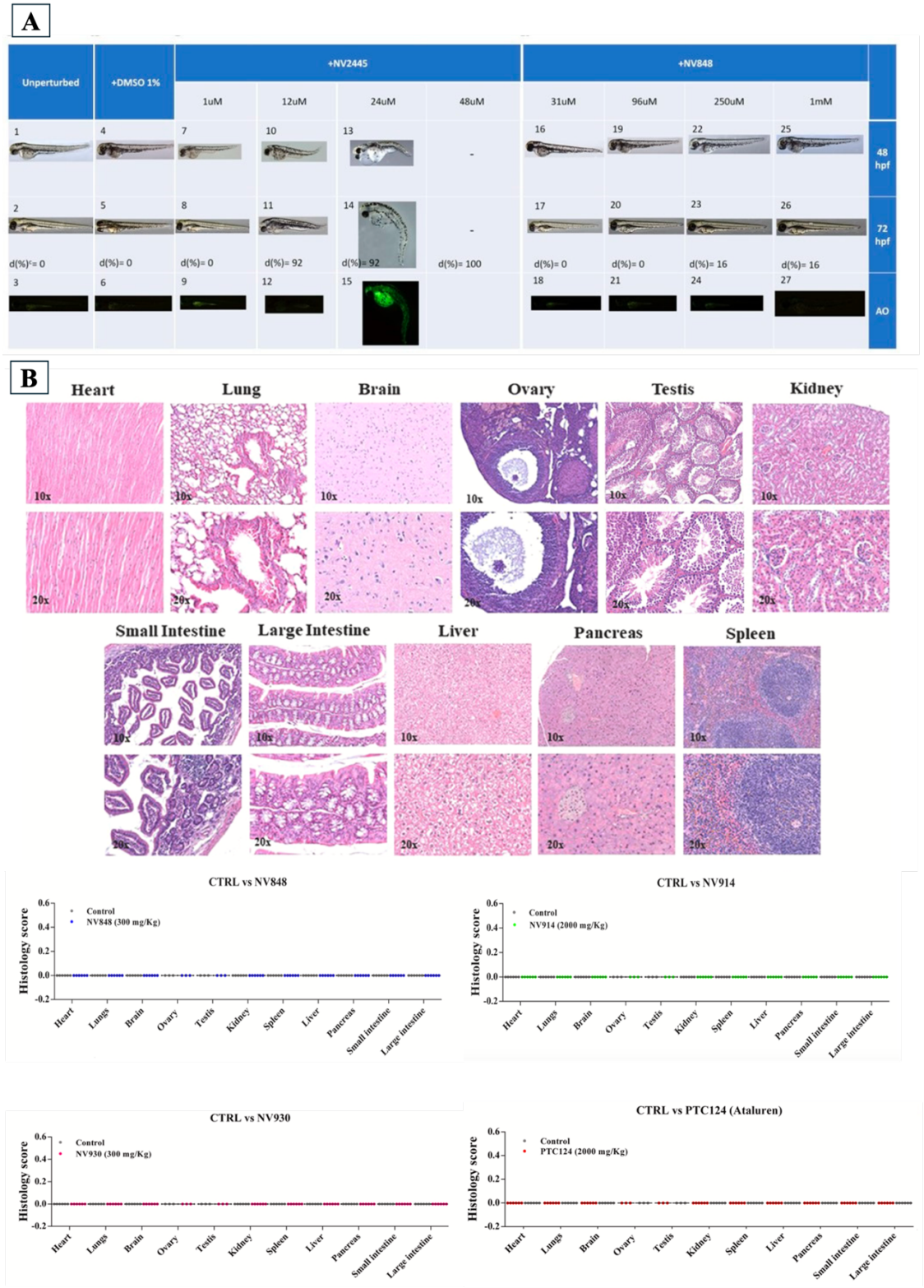

Figure 11. *(A) The evaluation of the toxic effects of NV848 on zebrafish embryos (adapted from Bezzerri et al., 2022). (B) No morphological or structural alterations were observed across all examined organs, as indicated by the histology scores shown in the accompanying graphs. Representative histological panel of organs (10X – 20X magnification) (adapted from Corrao et al., 2022).*

To evaluate their efficacy in readthrough of PTCs, the compounds were tested using the FLuc cell-based assay. Firefly Luciferase is an ATP-dependent enzyme that catalyze the oxidation of firefly luciferin, producing bioluminescence. HeLa cells were transiently transfected with the plasmids pFLuc-WT, which serves as a positive control expressing the wild-type luciferase gene, and pFLuc-opal, which contains a UGA stop codon mutation that mimics a PTC.

Treated cells displayed increased luciferase activity, particularly with NV848 and NV930, indicating potential as readthrough promoters (**Figure 12a**)(Pibiri et al., 2020). This finding was further supported by Western blotting and immunofluorescence analyses, which proved CFTR protein expression in $CFTR^{G542X}$ and $CFTR^{W1282X}$ FRT cells. Particularly, NV848 and NV930 promoted effective translational readthrough in $CFTR^{G542X}$ cells (**Figure 12b**), while NV914 and NV930 promoted CFTR protein expression in $CFTR^{W1282X}$ cells, confirmed by Western blot analyses (**Figure 12c**)(Pibiri et al., 2020).

Following the immunofluorescence and Western blotting experiments, the FRT $CFTR^{W1282X}$ cell line was further used to establish a dose-response curve, which was essential for identifying the optimal concentration that elicited the highest readthrough response. Both NV848 and NV930 exhibited maximum readthrough activity at 24 µM, while NV914 reached its peak activity at 48 µM (Pibiri et al., 2020).

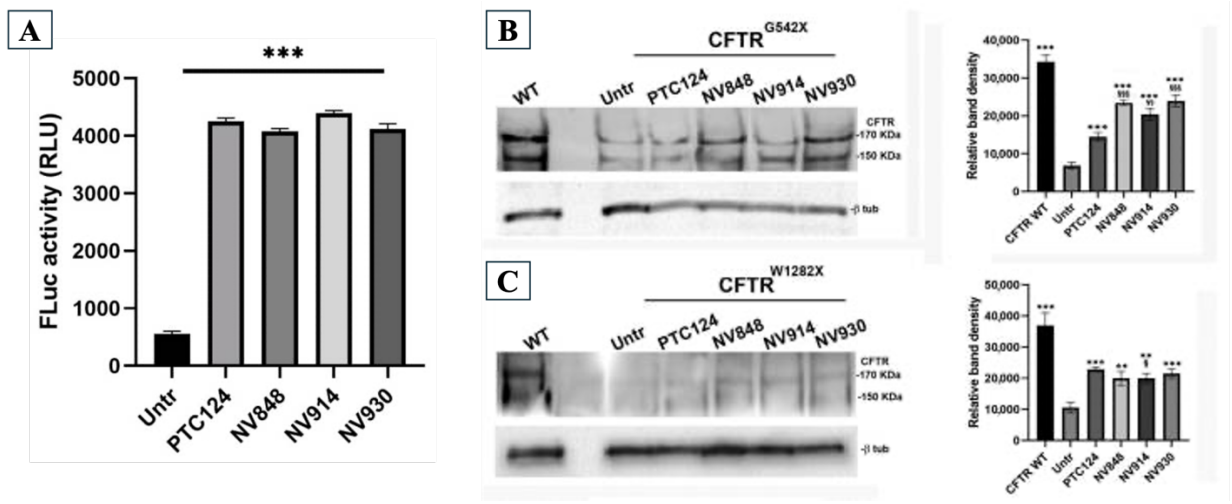

Figure 12. *(A) Luciferase activity was assessed after 24 hours of treatment with each molecule—PTC124, NV848, NV914, and NV930—at a concentration of 12 µM in HeLa cells transfected with the FLuc-opal plasmid. (B) Western blotting to evaluate the expression of CFTR protein in wild-type (WT) CFTR and $CFTR^{G542X}$ FRT cells. (C) Western blotting to evaluate the expression of CFTR protein in wild-type (WT) CFTR and $CFTR^{W1282X}$FRT cells (adapted from Pibiri et al., 2020).*

The readthrough activity of these molecules was also assessed in a cell line c.183-184TA>CT in Shwachman-Diamond syndrome (*SBD*). NV848 and NV914 demonstrated significant readthrough activity, resulting in a 250% and 319% increase in SBDS protein synthesis,

respectively, comparable to the effect observed with ataluren (178%). This activity was further confirmed in primary peripheral blood mononuclear cells (PBMCs), where 10 µM NV848 restored SBDS protein expression to levels comparable to those achieved with 2.5 µM ataluren (**Figure 13**)(Bezzerri et al., 2022).

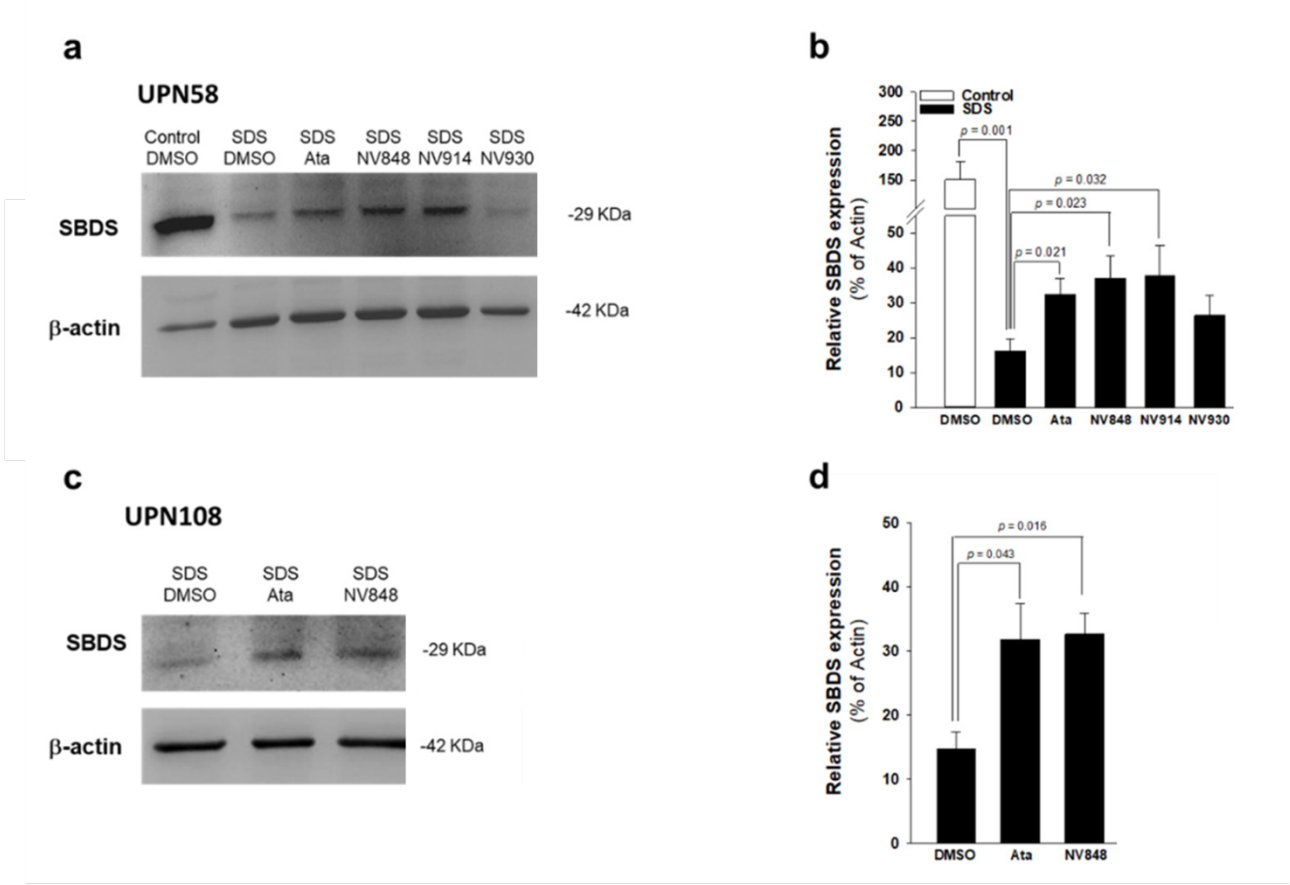

Figure 13. *Western blot analysis of SBDS protein levels in lymphoblastoid cell lines (LCLs) from UPN58 and healthy donors (Control). (B) Densitometry analysis of the bands. (C) Western blot analysis of SBDS in primary peripheral blood mononuclear cells (PBMCs) from UPN108. (D) Densitometry results (adapted from Bezzerri et al., 2022).*

In LRBA$^{R1683X/R1683X}$ human primary fibroblasts, Western blot analysis demonstrated that NV848, NV914, and NV930 significantly restored LRBA protein expression (Corrao et al., unpublished data) *(https://hdl.handle.net/10447/618889)*.

Additionally, a study of metabolic stability using human liver microsomes (HLMs), showed that NV848 maintained significant stability, with only a 15% reduction in concentration over 1 hour (Fiduccia et al., 2024).

Lastly, the potential off-target effects of NV848, NV914 and NV930 on NTCs were carefully evaluated using two complementary *in vitro* approaches. The first approach focused on the tumor suppressor protein p53, a crucial regulator of the cell cycle and a key marker for detecting DNA

damage and cellular stress. Changes in the molecular weight or functionality of p53 could indicate unintended translational alterations caused by readthrough of NTCs. Therefore, this experiment was performed to assess whether the treatment with these compounds induced any such alterations in p53 levels, which would suggest off-target activity (**Figure 14**). The second approach involved evaluating the molecular weights of two housekeeping proteins, Cystatin-C (Cys-C) and β2-Microglobulin (β2M), to detect any unintended elongation due to NTC readthrough (**Figure 15**). Results from both experimental systems indicated that treatment with NV848, NV914 and NV930 did not cause any detectable alterations in protein translation related to NTCs. These findings suggest that these compounds exhibit specificity towards PTCs, with no observed impact on NTCs, thus supporting their potential as selective therapeutic agents (Perriera et al., 2023).

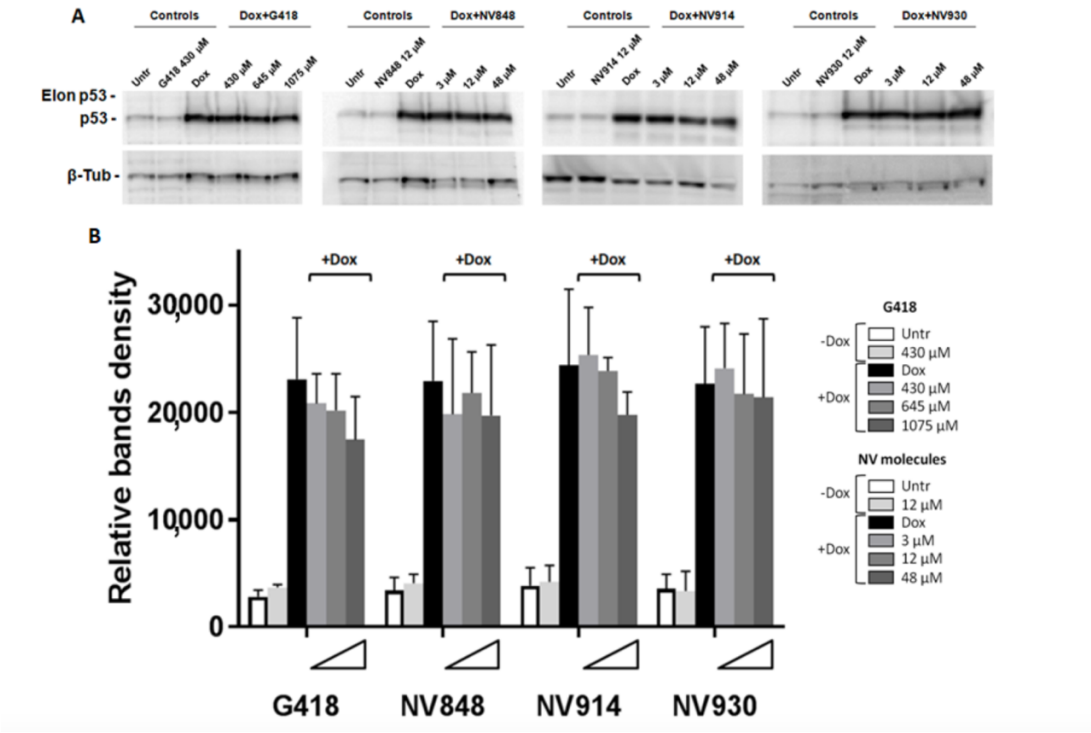

Figure 14. *(A) Western blot analysis was conducted to detect p53 levels in HCT116 cells following a 24-hour treatment with varying concentrations of G418 (430 µM, 645 µM, and 1,075 µM) or NV compounds (3 µM, 12 µM, and 48 µM). Treatments were administered both independently and in combination with Doxorubicin (Dox, 0.2 µg/mL) to induce DNA damage. Samples without Doxorubicin (-Dox) represent treatments applied without DNA damage induction. For each condition, β-Tubulin (β-Tub) was used as a loading control to ensure equal protein loading across the samples. (B) Quantification of the western blot bands was carried out using ImageJ software (adapted from Perriera et al., 2023).*

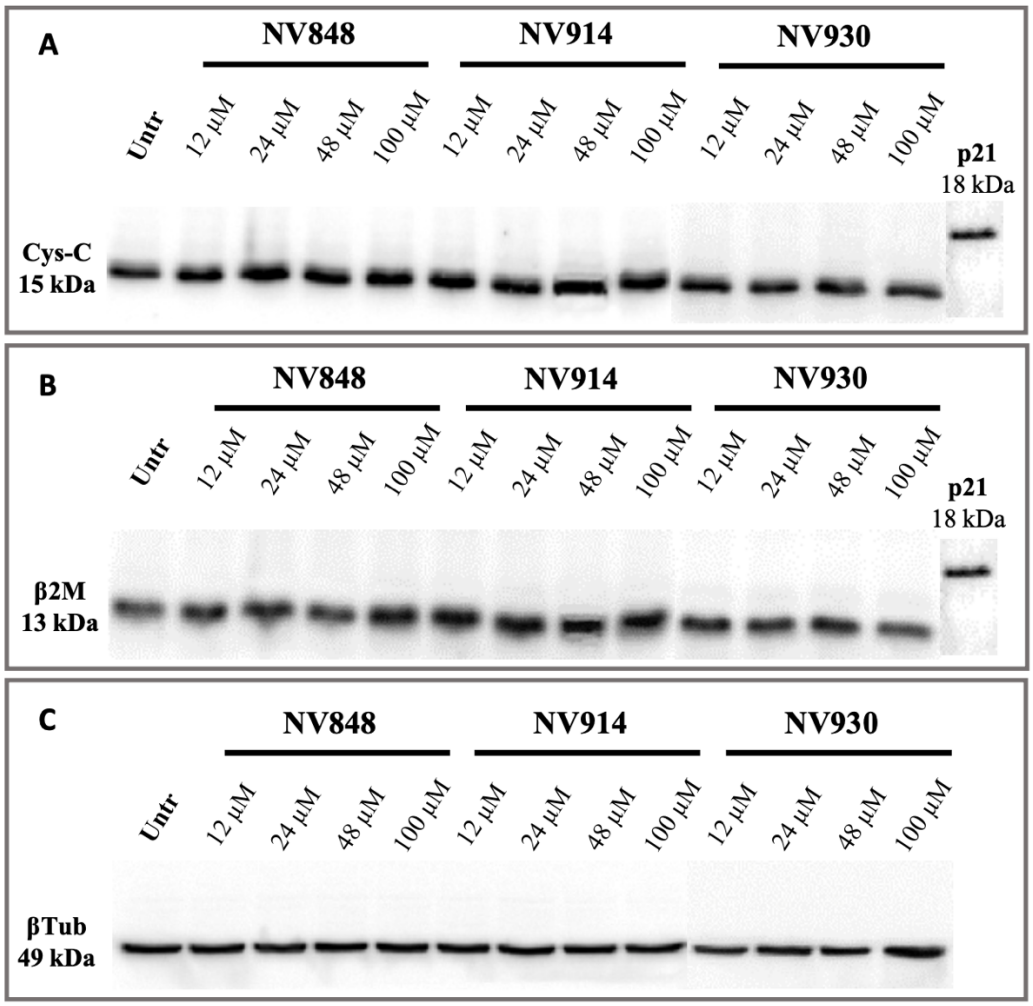

Figure 15. *Western blot analysis performed on 16HBE cells, comparing untreated (Untr; negative control) and cells treated for 24 hours with NV848, NV914, and NV930 at the indicated concentrations. The resulting images show the molecular weights of two housekeeping proteins: Cystatin-C (Cys-C; panel A) and β-2-microglobulin (β2M; panel B). The p21 protein served as an internal control for high molecular weight detection. Additionally, β-tubulin (βTub) was employed as a loading control (panel C). The assay was also performed with a prolonged treatment duration of 72 hours; however, the results remained consistent. (adapted from Perriera et al., 2023).*

The promising activity of NV compounds in promoting readthrough underscores their potential utility in the treatment of various nonsense mutation disorders. This opens the scenario to further research on their application in diseases like DMD, a severe condition caused by nonsense mutations that impair muscle function, and rarer disorders such as LRBA deficiency, which affects immune regulation. Evaluating these compounds in diverse disease models could illuminate new therapeutic pathways and support the development of more effective treatments for nonsense mutation-related conditions.

1.8 Duchenne Muscular Dystrophy (DMD)

DMD is a X-linked recessive disorder caused by mutations in the dystrophin gene, which results in full loss of dystrophin protein expression (Hoffman et al., 1987). DMD affects approximately 1 in 5.000 boys globally, but females with one faulty copy of the gene are generally asymptomatic. However, roughly 8% of female carriers may display symptoms and are referred to as "manifesting carriers" (Taylor et al., 2007; Duan et al., 2021).

The dystrophin gene, located at Xp21.1 on the X chromosome, is one of the largest gene in the human genome, spanning 2.5 megabases of DNA with 79 exons and 78 introns (Cohn and Campbell, 2000). The corresponding dystrophin protein, known as dp427 due to its molecular weight of 427 kDa, is made up of 3,685 amino acids (Hoffman et al., 1987; Emery, 2002). Approximately one-third of mutations occur *de novo*, while two-thirds are inherited from a carrier mother or are the result of germline mosaicism (Nallamilli et al., 2021; Bez Batti Angulski et al., 2023).

Over 7.000 different dystrophin mutations have been identified in patients with DMD or Becker muscular dystrophy (BMD) (Bladen et al., 2015). Large mutations account for 80% of them, with deletions representing 69% and duplications 11%. The remaining 20% are classified as small mutations, which include 25% deletions, 9% small insertions, and 14% alterations at splice sites. Additionally, point mutations constitute 52% of small mutations, of which 50% are nonsense mutations and 2% are missense mutations (Bladen et al., 2015).

DMD is usually diagnosed early, between the ages of 2 and 3 (Emery, 2002). Furthermore, some children with DMD have cognitive abnormalities with the diagnosis typically occurring between the ages of 4 and 5 (Ricotti et al., 2016). By ages 10 to 12, most patients require the use of a wheelchair due to the progression of muscle weakness (Tsuda, 2018). As the disease progresses, patients often develop scoliosis, joint contractures, and restrictive lung disease (Bushby et al., 2010). Assisted ventilation is usually required by the age of 15–20, and despite optimal care, most patients die of cardiac or respiratory failure between the ages of 20 and 30 (Mendell et al., 2012; Mercuri et al., 2019).

1.8.1 Dystrophin protein function

The main isoform of dystrophin is dp427m, which in striated muscles, serves as a crucial link between the actin filaments and the extracellular matrix (ECM) (Hoffman et al., 1987; Ahn and Kunkel, 1993). Dystrophin is a member of the spectrin superfamily of actin-binding proteins (Petrof et al., 1993; Bez Batti Angulski et al., 2023) and has four main functional domains: a N-

terminal (NT) domain, homologous to the actin-binding domains of α-actinin, which anchors dystrophin to the cytoskeleton; a central rod domain consisting of 24 spectrin-like repeats and 4 hinge regions. It has a second actin-binding domain (ABD2), which, in coordination with the first actin-binding domain (ABD1), creates a strong lateral association with actin filaments. Besides its role in actin binding, the rod domain also engages with microtubules, specifically via spectrin-like repeats 20-23, and contributes to the organization of the microtubule lattice in skeletal muscle cells (Straub et al., 1992; Bez Batti Angulski et al., 2023); a cysteine-rich (CR) domain that promotes binding to β-dystroglycan, a transmembrane protein. This binding is crucial for anchoring the cytoskeleton to the extracellular matrix, maintaining muscle fiber stability, and protecting muscle cells from damage during contraction; and a CT domain responsible for binding to dystrobrevin and syntrophins, fixing their positions to the sarcolemma (**Figure 16**) (Zhao et al., 2016; Bez Batti Angulski et al., 2023).

Dystrophin is integral to the dystrophin-glycoprotein complex (DGC), which maintains muscle integrity. The DGC includes extracellular components like α- and β-dystroglycan, which interact with ECM ligands, and cytoplasmic proteins such as syntrophins and neuronal nitric oxide synthase (nNOS), essential for stabilizing the muscle cell membrane (**Figure 16**) (Ervasti and Sonnemann, 2008; Duan et al., 2021; Starosta and Konieczny, 2021).

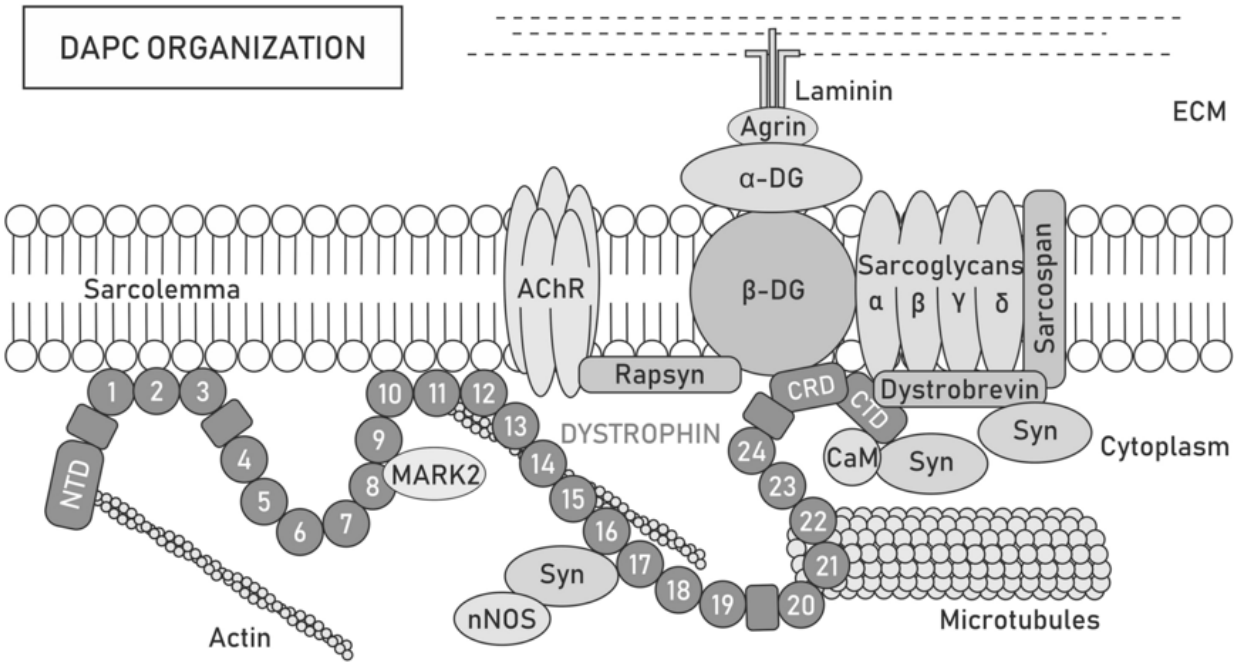

Figure 16. *The dystrophin-associated protein complex (DAPC) is organized around dystrophin, which acts as a scaffold and a hub for mechanical force transmission and signaling. DAPC composition varies by dystrophin isoform and cellular location. Full-length dystrophin (Dp427) has multiple domains enabling interactions with proteins like actin, β-dystroglycan, and syntrophins, supporting muscle stability and transmitting forces between the cytoskeleton and extracellular matrix during contractions (adapted from Starosta and Konieczny, 2021).*

1.9 Advanced *in vitro* systems for disease modeling: the role of 3D bioengineered tissues

3D bioengineered tissues are revolutionizing the field of *in vitro* disease modeling by offering a more physiologically relevant alternative to traditional 2D cell cultures. 2D models provide a limited view of cellular behavior, often failing to replicate the complex structural and functional degrees of native tissues. In contrast, 3D bioengineered systems aim to recreate the architecture, mechanical properties, and microenvironment found in human tissues. These advanced models include a diverse range of tissue types, including cardiac, skeletal muscle, neural, hepatic, and dermal tissues, each meticulously designed to reflect specific physiological and pathological features.

By utilizing 3D scaffolds or matrices, these bioengineered systems allow cells to grow and differentiate in ways that closely mimic *in vivo* conditions. This leads to more accurate modeling of disease mechanisms and enhances the predictive power for assessing drug efficacy and toxicity. Moreover, 3D bioengineered tissues provide valuable insights for regenerative medicine, allowing researchers to explore therapeutic strategies in a context that better resembles human biology.

Unlike organoids, which are self-organizing structures that replicate basic organ architecture, and organs-on-a-chip, which integrate fluid dynamics to simulate whole-organ function, 3D bioengineered tissues focus on replicating specific tissue functions with a high degree of precision. This targeted approach not only enhances our understanding of complex biological processes but also serves as a critical bridge between conventional cell cultures and live organisms.

1.9.1 3D bioengineered skeletal muscle

One of the most promising applications of 3D bioengineered tissues is the development of skeletal muscle models. In contrast to traditional 2D cultures, which lack the necessary structural complexity to facilitate muscle contraction, 3D bioengineered skeletal muscles aim to replicate the structure and function of native skeletal muscle, allowing researchers to study muscle physiology, disease mechanisms, and potential therapeutic interventions with enhanced precision. A notable advancement in this area involves the creation of a contractile, patient-derived 3D skeletal muscle model specifically designed to mimic the effects of DMD. This model effectively reproduces the damage at the sarcolemma observed in the native muscle of DMD patients, providing critical insights into the disease's pathology (Fernández-Costa et al., 2021).

This is achieved by inducing electrical stimulation to promote contractile responses, creating sarcolemma damage through specific contractile regimens that closely mimic the conditions experienced *in vivo* (**Figure 17**). This capability allows for the observation of muscle contraction and functional behavior, which is impossible in 2D cultures, where cells grow flat and lack the three-dimensional context (Tejedera-Villafranca et al., 2023).

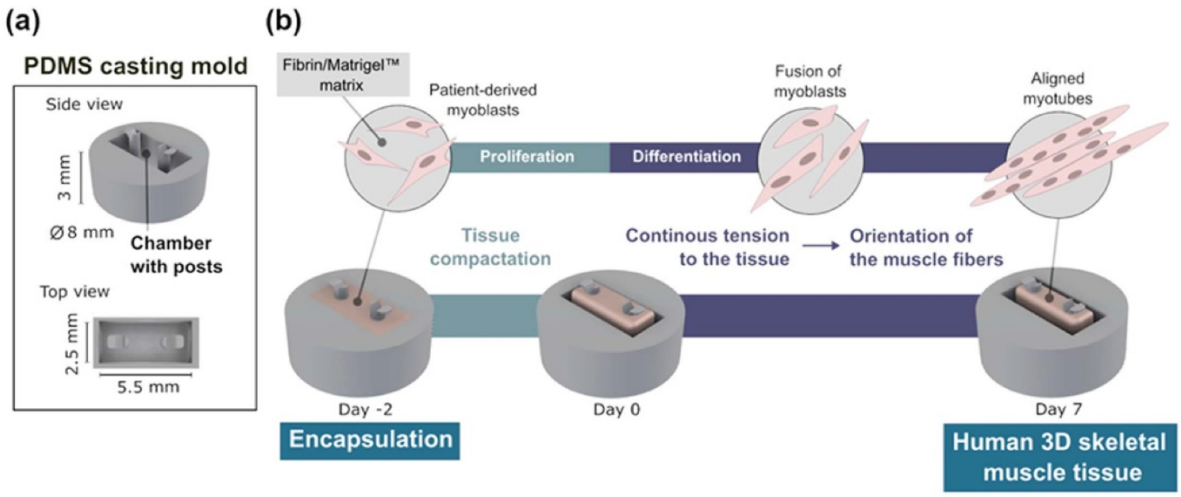

Figure 17. *(A) Illustration of the PDMS (polydimethylsiloxane) mold used for encapsulating muscle cells, featuring pillars for optimal alignment and support. (B) Overview of the encapsulation steps, including cell seeding in a hydrogel matrix within the mold, followed by a culture period for cell proliferation and tissue maturation (adapted from Tejedera-Villafranca et al., 2023).*

1.10 Lipopolysaccharide Responsive and Beige-like Anchor protein (LRBA) deficiency

LRBA deficiency is a rare, autosomal recessive immunodeficiency disorder, first described in 2012, that arises from mutations in the LRBA gene. LRBA deficiency occurs in approximately 1 in 1.000.000 individuals, and its incidence may be underestimated due to the diverse clinical presentations (Mangodt et al., 2023). The LRBA gene is located on chromosome 4q31.3 (OMIM # 606453) spanning a length of 750.839 base pairs, consisting of 58 exons. The protein product of LRBA consists of 2863 amino acids and has a molecular weight of 319 kDa. LRBA is characterized by the presence of several domains, the BEACH domain (beige and Chediak-Higashi), which is roughly 280 amino acids in length, is conserved across a range of proteins classified as BEACH domain-containing proteins (BDCP) and is typically found towards the CT end of the protein (Gebauer et al., 2004; Martínez Jaramillo and Trujillo-Vargas, 2018). In addition to the BEACH domain, proteins within the BDCP family often include several other functional domains such as the ConA-like domain (concanavalin A-like), the Pleckstrin

homology (PH) domain, and the WD40 domain, which is characterized by repeated units of tryptophan and aspartic acid. Furthermore, evidence suggests that LRBA may contain a VHS domain (**Figure 18**) (Martínez Jaramillo and Trujillo-Vargas, 2018).

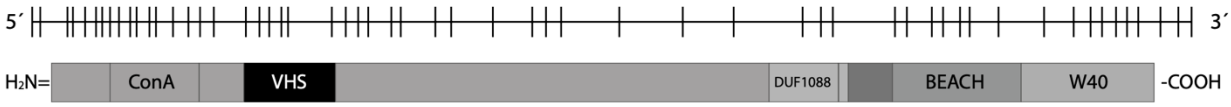

Figure 18. *Schematic representation of human LRBA protein containing a Concanavalin A (Con-A) domain, a VHS domain, a Pleckstrin Homology (PH)-like domain and a BEACH (beige and CHS) domain (adapted from Austin J Clin Immunol. 2014;1(1): 1004.).*

1.10.1 LRBA protein function

LRBA protein is a critical regulator of intracellular trafficking, particularly in the recycling and stability of CTLA-4 (Cytotoxic T-Lymphocyte Antigen 4), a receptor that plays an important role in controlling immune responses (Martínez Jaramillo and Trujillo-Vargas, 2018). LRBA works with the intracellular trafficking machinery to prevent CTLA-4 from degrading too quickly. By competing with proteins like adaptor protein 1 (AP-1), LRBA helps recycle CTLA-4 from endosomes back to the plasma membrane, ensuring it remains available to prevent excessive immune activation. LRBA is also closely linked to Rab11, a GTPase responsible for recycling endosomes. This connection ensures proteins are returned to the cell surface instead of being sent to degradation.

Rab7, another important GTPase, is associated with the trafficking of late endosomes and lysosomes, which play key roles in degradation pathways. Since Rab7 is involved in lysosomal degradation, it's likely that LRBA, by modulating endosomal sorting, helps prevent the degradation of proteins like CTLA-4 that Rab7 would otherwise direct to lysosomes. Instead, LRBA favors recycling via Rab11.

CTLA-4 itself is an immune checkpoint receptor that modulates immune responses by inhibiting T cell activation. It is constitutively expressed on regulatory T cells (Treg) and is transiently expressed on activated CD4+ and CD8+ T cells (Taghizade et al., 2023). In cells lacking constitutive expression, CTLA-4 is stored in compartments such as the Golgi apparatus, endosomes, and lysosomes. Once T cells are activated, CTLA-4 moves to the cell surface, where it competes with CD28 for binding to CD80 and CD86 on antigen-presenting cells (APCs), acting as a brake on immune activation (Qureshi et al., 2011). Unlike CD28, which stays on the cell surface, CTLA-4 undergoes rapid internalization through clathrin-coated vesicles (Qureshi et al., 2012). Recent studies show that the fate of CTLA-4 after internalization varies depending on

which ligand it interacts with. Binding to CD86 promotes CTLA-4 recycling, thereby supporting Treg function, while interaction with CD80 leads to CTLA-4 degradation through ubiquitination (**Figure 19**) (Kennedy et al., 2022).

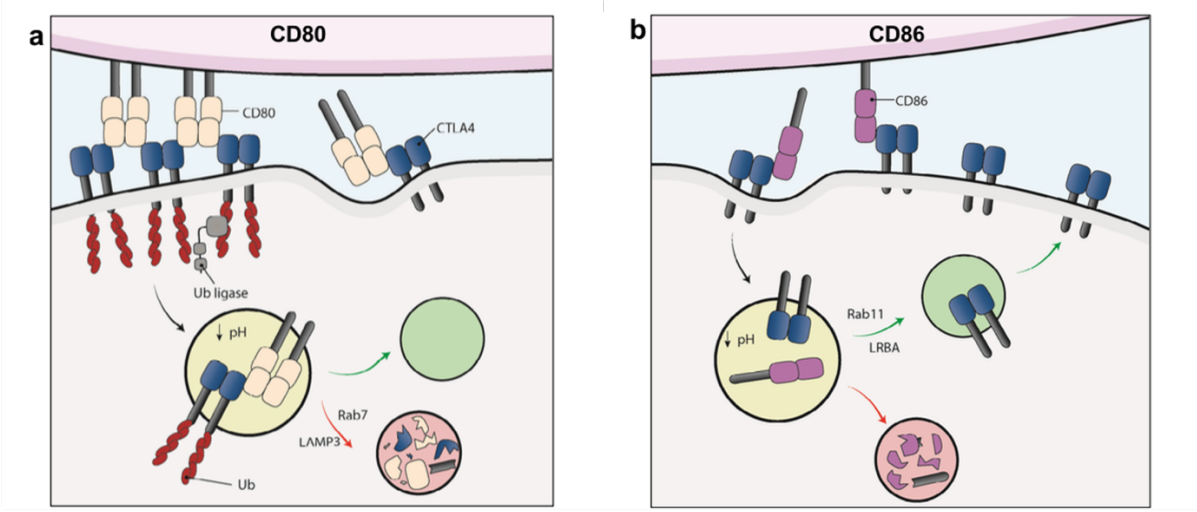

Figure 19. *Proposed model of CD80 and CD86 influence on CTLA-4 trans-endocytosis: (a) CD80 interacts with CTLA-4 to form dimer-dimer lattices, leading to CTLA-4 ubiquitylation. (b) CD86, on the other hand, does not ubiquitinate CTLA-4 due to lower affinity, allowing unmodified CTLA-4 to recycle back to the cell surface via LRBA and Rab11 pathways (adapted from Kennedy et al., 2022).*

The cytoplasmic tail of CTLA-4 contains key motifs, such as Y201VKM and Y218FIP, that interact with proteins like AP-1 and AP-2, which mediate its internalization and trafficking. AP-2 is involved in internalization, while AP-1 directs its movement through the Golgi and towards lysosomal pathways. LRBA plays a protective role in this process by binding to the Y201VKM motif, preventing AP-1 from directing CTLA-4 to lysosomes for degradation. This ensures that CTLA-4 is available to regulate immune responses effectively, maintaining immune tolerance and preventing overactivation of T cells (Wang et al., 2001; Lopez-Herrera et al., 2012; Lo et al., 2015; Martínez Jaramillo and Trujillo-Vargas, 2018).

Beyond its role in regulating CTLA-4, LRBA is also involved in the vesicular trafficking of other receptors, including the epidermal growth factor receptor (EGFR), a tyrosine kinase receptor, and the Fas death receptor (Wang et al., 2004; Lee et al., 2006). When a ligand binds to EGFR, the receptor pairs up with another EGFR molecule in a process called dimerization. This pairing activates the receptor through trans-auto-phosphorylation, recruiting signaling proteins to regulate key cellular activities, including cell growth, division and preventing cell death (Wee and Wang, 2017). EGFR on the cell surface is regulated via clathrin-mediated endocytosis, in a similar way of CTLA-4. This internalization process can lead to either the receptor's degradation

within lysosomal compartments or its recycling back to the plasma membrane (Sigismund et al., 2008). While the direct interaction between LRBA and EGFR is not yet established, dominant-negative LRBA mutants decreases the expression and phosphorylation of EGFR. Moreover, evidence supports the role of AP-2 in facilitating the endocytosis and trafficking of EGFR through the endocytic route (Gámez-Díaz et al., 2016).

The Fas receptor is crucial for triggering apoptosis through the extrinsic pathway, activated when it binds to Fas ligand (FasL). This process involves receptor internalization and tight regulation to ensure appropriate apoptosis (Degli Esposti et al., 2009; Martínez Jaramillo and Trujillo-Vargas, 2018).

LRBA is also associated with autophagy, a lysosomal degradation mechanism that eliminates damaged organelles and microorganisms via autophagosomes. These structures mature by fusing with endosomes to form amphisomes, which later fuse with lysosomes for degradation (Gutierrez et al., 2004; Hansen and Johansen, 2011; Ryter et al., 2014). Hypothesis suggests that LRBA may play a role in the fusion of autophagosomes with late endosomes or potentially competing with clathrin adapter proteins involved in autophagic influx (Martínez Jaramillo and Trujillo-Vargas, 2018).

In the context of apoptosis, LRBA-deficient cells have shown increased markers of apoptosis, highlighting its role in cell survival. The interplay between autophagy and apoptosis is complex; while autophagy can promote survival under certain conditions, defects in autophagy may lead to increased apoptosis. The precise mechanisms through which LRBA regulates these processes and their implications for immune homeostasis and inflammation require further investigation (Martínez Jaramillo and Trujillo-Vargas, 2018).

The implications of nonsense mutations in disorders such as DMD and LRBA deficiency underscore the urgent need for innovative therapeutic approaches. The following section outlines the specific objectives of this research, aimed at investigating the potential of these novel TRIDs in restoring protein function, addressing the challenges posed by these genetic disorders and completing the preclinical phases of development.

2 Objectives

Diseases caused by nonsense mutations present a considerable challenge in genetic medicine, as there are currently no effective therapeutic options available to address these mutations. This significant gap in treatment underscores the urgent need for innovative strategies that target the underlying genetic defects directly, rather than merely managing symptoms. TRIDs offer a promising approach, as they have the potential to bypass the PTC and restore a full-length functional protein.

Starting by the brilliant results obtained *in vitro* and *in vivo* for compounds NV848, NV914 and NV930 (Pibiri et al., 2020), to further explore their potential as TRIDs, it is important to conduct and complete preclinical study. This includes the synthesis of these TRIDs, along with the parental drug PTC124 (as positive control) and various oxadiazole derivatives for use as internal standards. This thesis aims to further elucidate the therapeutic potential of NV848, NV914, and NV930 in addressing nonsense mutations in different disorders.

Following the initial evaluation of NV848's metabolic stability, the metabolic profiles of the remaining two TRID compounds, NV914 and NV930, were assessed under similar conditions to determine their stability and potential as therapeutic agents.

In this respect both NV914 and NV930 were subjected to *in vitro* assays to examine their phase I and phase II metabolic stability by incubating them with human liver microsomes, monitor the rate of degradation and identify any metabolic products that may result from enzymatic activity.

In order to proceed with preclinical development, it is important to assess the organs that are reached by the molecules after oral administration in mice model: an *in vivo* biodistribution study was conducted in wild-type mice C57BL/6. The primary objective of this study was to determine the ability of these TRIDs to reach specific organs, providing critical insights into their therapeutic applicability. The study also helped to anticipate potential off-target effects.

In addition to *in vivo* studies, this research focuses on an advanced in vitro model of 3D bioengineered skeletal muscle derived from DMD patients, characterized by nonsense mutations. Conducted at the Institute for Bioengineering of Catalonia (IBEC) in Barcelona (Spain), in Javier Ramón Azcón's research group, this study aims to validate a reporter system designed explicitly for DMD patients with nonsense mutations. The 3D model offers significant advantages over traditional 2D cultures, as it more accurately mimics the structural and functional characteristics of human muscle tissue. By utilizing this advanced model, the research investigates the efficacy of TRIDs in rescuing dystrophin protein, contributing to a better understanding of their therapeutic potential.

Additionally, using such models contributes to reducing the reliance on animal testing during the early stages of drug development, a consideration that aligns with ethical research practices.

Another significant focus of this thesis has been the study of the proteomic impact of the NV molecules on cells harboring a nonsense mutation in the LRBA gene. Conducted under the guidance of Prof. Dr. Samuel Meier-Menches at the University of Vienna, this study aims to explore the broader impact of TRIDs on cellular protein expression.

The proteomic approach offers a deeper understanding of how NV848, NV914 and NV930 influence protein networks and pathways disrupted by nonsense mutations. Such analyses not only reveal specific proteins affected by treatment but also provide insights into potential off-target effects and cellular mechanisms.

In summary, the work presented in this thesis seeks to contribute to the understanding of TRIDs as viable therapeutic agents for nonsense mutations. Through a combination of *in vitro* metabolic stability, *in vivo* biodistribution studies, advanced *in vitro* modeling, and proteomic analyses, this research aims to provide valuable information that can drive the future development of targeted therapies for genetic disorders associated with premature termination of protein synthesis.

3 Results and Discussion

3.1 Synthesis and characterization of *3-acetylamino-5-methyl-1,2,4-oxadiazole* (NV848)

The synthesis route for this compound has already been described in the literature (Pibiri et al., 2020). It involves the cyclization of a nitrile with hydroxylamine, a well-established method for constructing the 1,2,4-oxadiazole ring.

The reaction proceeds through the formation of an amidoxime intermediate, which is then reacted with an excess of acetic anhydride in the presence of a base. This step promotes both the dehydration necessary for ring closure and the selective acylation of the amino group at the 3-position. The result is the final compound, 3-acetylamino-5-methyl-1,2,4-oxadiazole (**Scheme 1**).

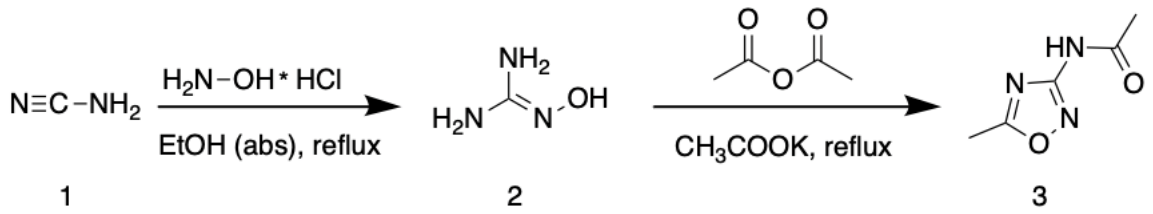

Scheme 1. *This scheme illustrates the synthetic pathway for 3-acetylamino-5-methyl-1,2,4-oxadiazole starting from cyanamide.*

The synthetic process began with cyanamide (**1**), which was reacted with hydroxylamine hydrochloride under reflux in absolute ethanol, leading to the formation of the corresponding amidoxime (**2**). This step proceeded smoothly under mild conditions, yielding the key intermediate for the subsequent reactions. In the next step, amidoxime (**2**) was treated with an excess of acetic anhydride in the presence of potassium acetate under reflux. This reaction produced 3-acetylamino-5-methyl-1,2,4-oxadiazole (**3**).

However, the initial synthesis proved inefficient, with a modest overall yield of approximately 18%, combined by the formation of several side products. These byproducts likely arose from rearrangements of the oxadiazole ring into the 1,3,4-oxadiazole structure, which complicated the reaction and reduced the overall yield. To address these inefficiencies, further optimization of the reaction conditions was undertaken to minimize side reactions and improve the yield of the desired products.

3.1.1 Optimization of the synthetic route for *3-acetylamino-5-methyl-1,2,4-oxadiazole* (NV848)

The literature presents an alternative synthetic route for the preparation of 3-amino-5-methyl-1,2,4-oxadiazole (**Scheme 2**)(Vieira et al., 2005). Various reaction conditions, including different temperatures and solvents, were systematically evaluated. The conditions outlined below were determined to be the most effective for this synthesis.

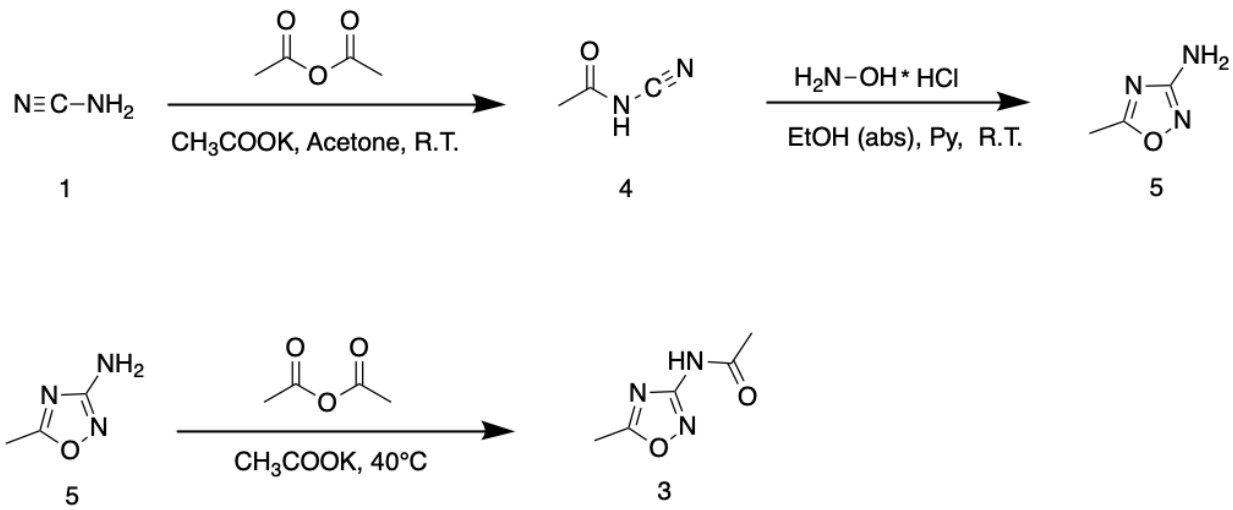

1 4 5 5 3

Scheme 2. *This scheme illustrates an alternative synthetic route for the preparation of 3-amino-5-methyl-1,2,4-oxadiazole.*

Unlike the previous method, the synthetic process initiated with cyanamide (**1**), which was reacted with acetic anhydride in acetone at room temperature overnight, resulting in the formation of acetylcyanamide (**4**). Although this step takes longer, it generates fewer side products, making purification easier. Additionally, the yield for this reaction approaches 100%.

In the following step, acetylcyanamide (**4**) was treated with hydroxylamine hydrochloride in the presence of pyridine in absolute ethanol at room temperature overnight. This reaction led to the formation of 3-amino-5-methyl-1,2,4-oxadiazole (**5**), which was then purified via column chromatography, resulting in a yield of approximately 55%.

In the subsequent step, compound (**5**) was treated with acetic anhydride and potassium acetate under solvent-free conditions at 40°C for 24 hours to obtain compound (**3**). The methylation reaction of compound (**5**) proceeded efficiently, with a yield of 85%. After purification by column chromatography and crystallization from ethanol, the overall yield for the entire synthetic route was approximately 46%, marking a significant improvement over the initial method and demonstrating the effectiveness of the optimized reaction conditions.

3.2 Synthesis and characterization of 3-pentafluorobenzoylamino-5-perfluorophenyl-1,2,4-oxadiazole (NV914)

The synthesis route for this compound involves the classic amidoxime method. The process begins with the reaction of a nitrile with hydroxylamine, leading to the formation of an amidoxime intermediate. This intermediate is then reacted with an acyl chloride to promote cyclization and form the 1,2,4-oxadiazole ring. The use of an excess of acyl chloride, in this case, ensures that, after the ring closure, the free amine on the oxadiazole at the 3-position is acylated (**Scheme 3**).

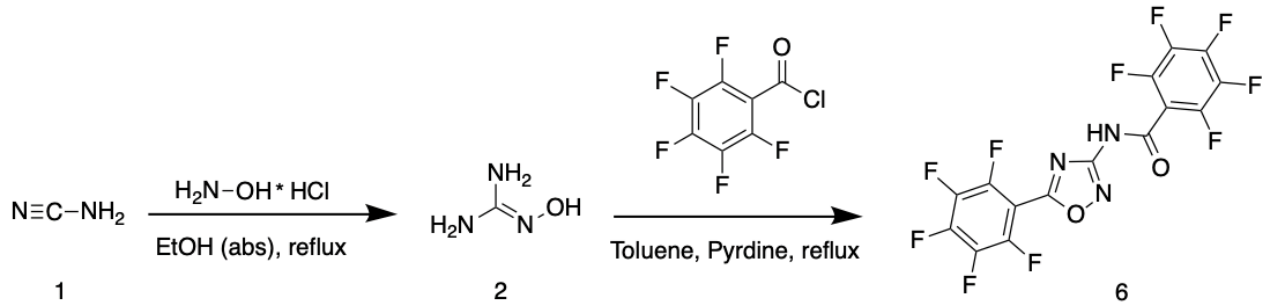

Scheme 3. *Synthesis of 1,2,4-oxadiazole via the amidoxime route.*

The synthetic process began with cyanamide (**1**), which was reacted with hydroxylamine hydrochloride under reflux in absolute ethanol, leading to the formation of the hydroxyguanidine (**2**). In the next step, hydroxyguanidine (**2**) was treated with an excess of pentafluorobenzoyl chloride in the presence of pyridine, using toluene as a solvent, under reflux. This reaction led to the formation of the desired compound 3-pentafluorobenzoylamino-5-perfluorophenyl-1,2,4-oxadiazole (**6**). The product was successfully isolated by column chromatography and further crystallized in ethanol.

Despite successful formation of the desired product, the reaction conditions were suboptimal, as evidenced by a modest overall yield of 10%. Refluxing under these conditions produced several by-products.

3.2.1 Optimization of the 3-pentafluorobenzoylamino-5-perfluorophenyl-1,2,4-oxadiazole (NV914)

In optimizing the synthesis of the desired product, several key modifications were made to the original procedure. The focus was on improving reaction conditions, minimizing by-products, and addressing practical challenges, such as reagent loss due to high temperatures, which could lead to compound degradation and unwanted side reactions.

The original process, which involved the formation of hydroxyguanidine from cyanamide and hydroxylamine hydrochloride followed by reaction with pentafluorobenzoyl chloride under reflux, suffered from low yields and product impurities.

To address these challenges, hydroxylamine hydrochloride was first treated with sodium bicarbonate at room temperature to free the nucleophilic hydroxylamine, ensuring a more efficient nucleophilic attack in the subsequent reaction. Besides, the cyclization step with pentafluorobenzoyl chloride was conducted under thermoregulated conditions between 0°C and 5°C instead of refluxing (**Scheme 4**). This adjustment aimed to improve reaction selectivity and reduce by-product formation.

These optimizations resulted in improved yields, reduced impurities, and more efficient handling of the reaction mixture, laying the foundation for a more reliable synthetic route.

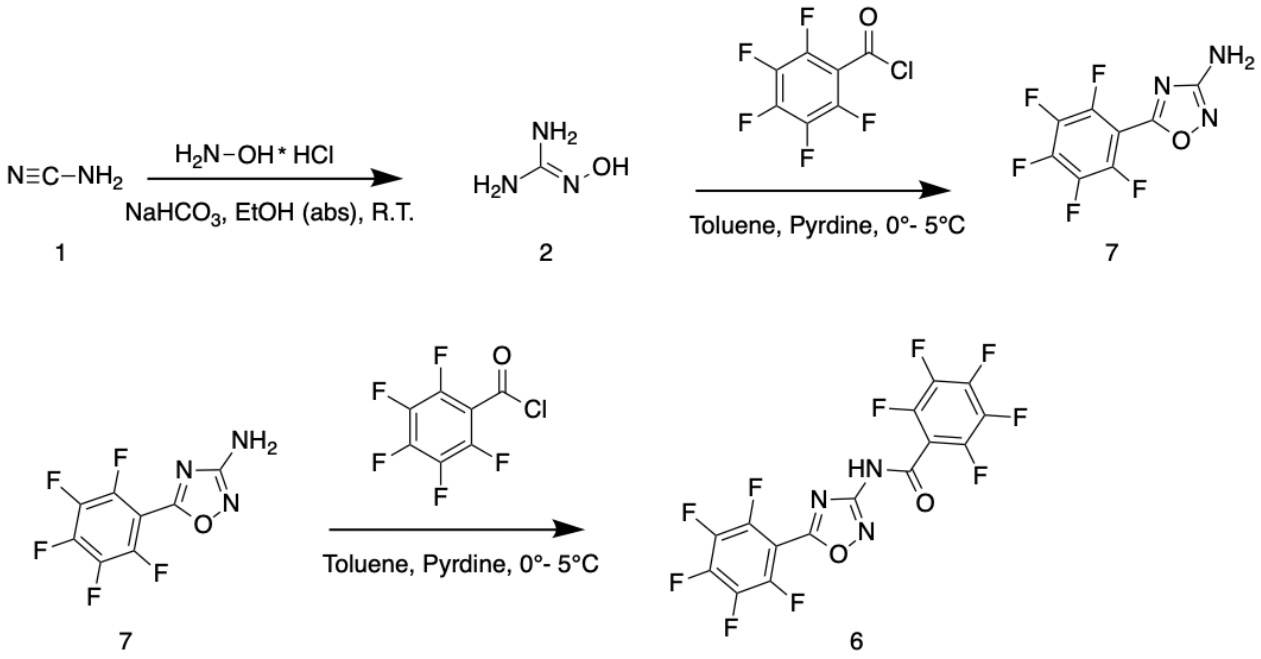

Scheme 4. *This scheme illustrates the optimized synthesis route for hydroxyguanidine from cyanamide and hydroxylamine hydrochloride, followed by cyclization with pentafluorobenzoyl chloride.*

The synthetic process began with cyanamide (**1**), which was reacted with hydroxylamine hydrochloride at room temperature in absolute ethanol overnight, leading to the formation of hydroxyguanidine (**2**). In the next step, hydroxyguanidine (**2**) was treated with pentafluorobenzoyl chloride in the presence of pyridine, using toluene as the solvent. This reaction was carried out under thermoregulated conditions, maintained between 0°C and 5°C, overnight. As a result, the desired compound, 3-amino-5-perfluorophenyl-1,2,4-oxadiazole (**7**), was obtained. After compound (**7**) was purified by column chromatography, the reaction set in

the same conditions as prior to produce 3-pentafluorobenzoylamino-5-perfluorophenyl-1,2,4-oxadiazole (**6**). The final product was then further purified by column chromatography and crystallized from ethanol, with an overall yield of 31%.

3.3 Synthesis and characterization of ethyl 5-phenyl-1,2,4-oxadiazole-3-carboxylate (NV930)

The synthesis of ethyl 5-phenyl-1,2,4-oxadiazole-3-carboxylate follows a stepwise process involving the reaction of ethyl cyanoformate with hydroxylamine. This reaction forms an amidoxime intermediate, which subsequently reacts with benzoyl chloride. The resulting product is an open-chain structure, which undergoes cyclization through a final dehydration step (**Scheme 5**).

Upon heating the intermediate to 165°C, its melting point is reached, and a dehydration reaction occurs, leading to the elimination of a water molecule and the closure of the 1,2,4-oxadiazole ring. The phenyl group at the 5-position comes from the benzoyl chloride, while the carboxyethyl group is derived from the ethyl cyanoformate starting material.

Following ring closure, the product is purified and crystallized, yielding ethyl 5-phenyl-1,2,4-oxadiazole-3-carboxylate. This method ensures efficient cyclization and selective functionalization, resulting in the desired oxadiazole compound with good yield.

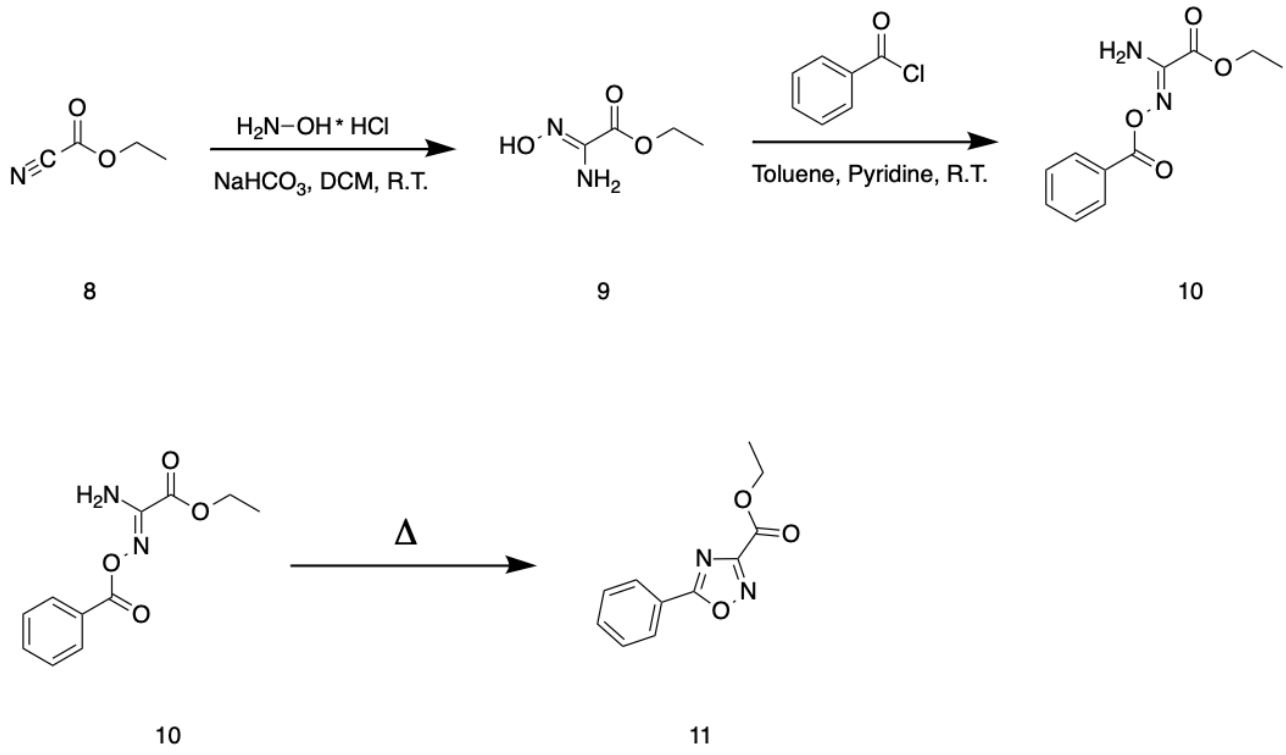

Scheme 5. *This scheme outlines the stepwise synthesis of ethyl 5-phenyl-1,2,4-oxadiazole-3-carboxylate.*

The synthetic process began with ethyl cyanoformate (**8**), which was reacted with hydroxylamine at room temperature in dichloromethane for 24 hours. This reaction resulted in the formation of ethyl-2-amino-2-(hydroxyimino)acetate (**9**). Following this, compound (**9**) was isolated through crystallization, preparing it for the subsequent reaction.

In the next step, compound (**9**) was reacted with benzoyl chloride in the presence of pyridine, using toluene as the solvent. This reaction was also conducted at room temperature for 24 hours, yielding ethyl-2-amino-2-((benzoyloxy)imino)acetate (**10**). After purification by column chromatography, compound (**10**) was placed into a high-pressure tube and subjected to an oil bath at 165°C for 2 hours. During this step, compound (**10**) underwent dehydration, resulting in the formation of ethyl 5-phenyl-1,2,4-oxadiazole-3-carboxylate (**11**). The final product was subsequently purified by column chromatography and crystallized from ethanol with an overall yield of 52%.

3.4 Synthesis and characterization of *Ataluren* (PTC124)

The synthesis of Ataluren follows a carefully designed multi-step route, as outlined in its original patent (**Scheme 6**) (Karp et al., 2006). The process begins with the construction of key intermediates through strategic reactions, leading to the formation of the 1,2,4-oxadiazole ring.

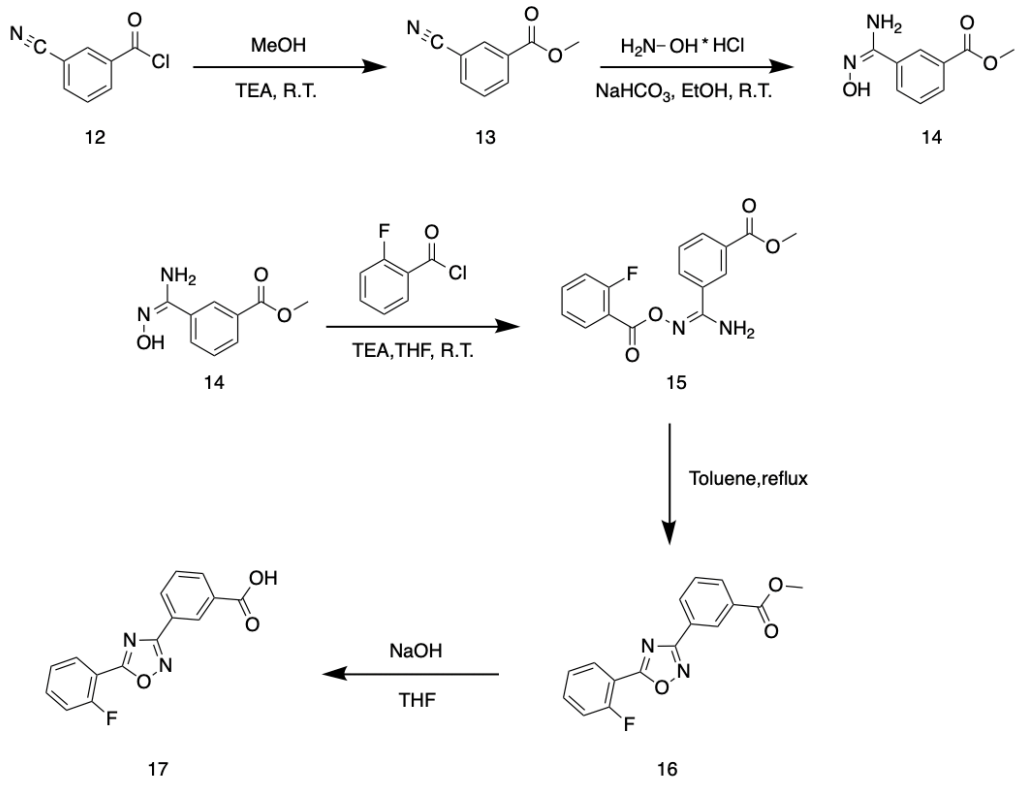

Scheme 6. *This scheme illustrates the multi-step synthetic route for Ataluren.*

The synthesis of Ataluren started with the reaction of 3-cyanobenzoyl chloride (**12**) and methanol in the presence of triethylamine, resulting in the formation of methyl 3-cyanobenzoate (**13**) with a yield of 95%. This esterification was conducted at room temperature over a duration of 24 hours. Following the successful isolation of compound (**13**), it was treated with hydroxylamine hydrochloride in ethanol, alongside sodium bicarbonate, yielding the amidoxime derivative, methyl-3-(N'-hydroxycarbamimidoyl)benzoate (**14**), which was obtained in 93% yield.
After purification by column chromatography, compound (**14**) was dissolved in anhydrous THF and treated with triethylamine. The addition of 2-fluorobenzoyl chloride resulted in the formation of methyl-3-(N'-((2-fluorobenzoyl)oxy)carbamimidoyl)benzoate (**15**), with a yield of 79%.
The next stage involved setting compound (**15**) under reflux in toluene for one hour, which promoted cyclization and yielded methyl 3-(5-(2-fluorophenyl)-1,2,4-oxadiazol-3-yl)benzoate (**16**) in an 83% yield. The final step required hydrolysis of the ester group using sodium hydroxide in THF, resulting in the target compound, 3-(5-(2-fluorophenyl)-1,2,4-oxadiazol-3-yl)benzoic acid (**17**), with a yield of 60%. Overall, the entire synthetic route afforded a cumulative yield of 34%.

3.5 Synthesis and characterization of 2,3,5,6-tetrafluoro-4-methoxy-N-(5-(2,3,5,6-tetrafluoro-4-methoxyphenyl)-1,2,4-oxadiazol-3-yl)benzamide (IP30)

Accurate quantification of target analytes in complex matrices often requires the use of a structurally related internal standard to ensure precision and reliability in analytical methods. The 2,3,5,6-tetrafluoro-4-methoxy-N-(5-(2,3,5,6-tetrafluoro-4-methoxyphenyl)-1,2,4-oxadiazol-3-yl)benzamide (IP30) was synthetized to serve as an internal standard specifically for NV914. The structural similarity between IP30 and NV914, differing primarily in the replacement of fluorine with methoxy groups, enables the standard to mimic the analyte's chemical behavior closely while remaining distinguishable during analysis.
The reaction involves the nucleophilic aromatic substitution of one of the fluorine atoms on the perfluorophenyl rings by the methoxide ion (**Scheme 7**). The electron-deficient perfluorophenyl ring is highly susceptible to nucleophilic attack due to the strong electron-withdrawing effect of the multiple fluorine atoms.

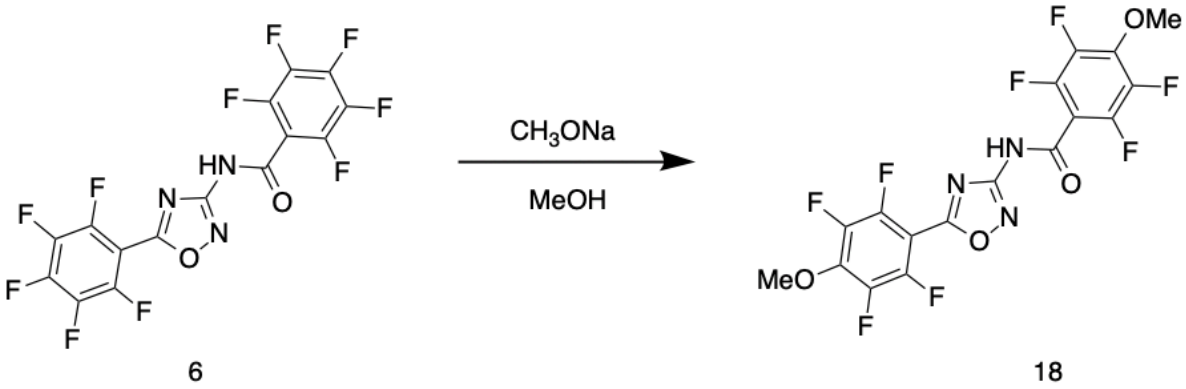

Scheme 7. *This scheme illustrates the nucleophilic aromatic substitution reaction involving both perfluorophenyl rings.*

In this synthetic route, 2,3,4,5,6-pentafluoro-N-(5-(perfluorophenyl)-1,2,4-oxadiazol-3-yl)benzamide (**6**) was reacted with an excess of sodium methoxide in methanol, allowing the reaction to proceed at room temperature overnight. This reaction led to the formation of 2,3,5,6-tetrafluoro-4-methoxy-*N*-(5-(2,3,5,6-tetrafluoro-4-methoxyphenyl)-1,2,4-oxadiazol-3-yl)benzamide (**18**), which was then isolated by flash chromatography with a yield of 22%.

3.6 Synthesis and characterization of isopropyl-5-phenyl-1,2,4-oxadiazole-3-carboxylate (IP31)

Analogous to the synthesis of IP30, the preparation of isopropyl-5-phenyl-1,2,4-oxadiazole-3-carboxylate (IP31) was designed to create a structurally aligned internal standard for its parent compound, NV930.

The synthetic pathway begins with ethyl 5-phenyl-1,2,4-oxadiazole-3-carboxylate as a key starting material, which undergoes a transesterification reaction with potassium tert-butoxide (KOtBu) in isopropyl alcohol (IPA) (**Scheme 8**). The basic environment generated by KOtBu deprotonates isopropanol to form the isopropoxide ion, which facilitates the exchange of the ethyl group for the isopropyl group, yielding isopropyl-5-phenyl-1,2,4-oxadiazole-3-carboxylate.

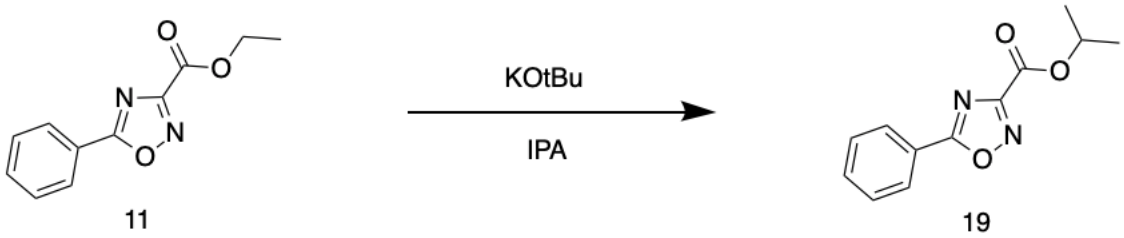

Scheme 8. *This scheme illustrates the synthetic pathway that begins with ethyl 5-phenyl-1,2,4-oxadiazole-3-carboxylate as a key starting material.*

In this synthetic route, ethyl 5-phenyl-1,2,4-oxadiazole-3-carboxylate (**11**) was reacted with an excess of isopropyl alcohol and potassium tert-butoxide to promote transesterification at room temperature, allowing the reaction to proceed overnight. This process led to the formation of isopropyl 5-phenyl-1,2,4-oxadiazole-3-carboxylate (**19**), which was subsequently isolated by flash chromatography with a yield of 30%.

3.7 Synthesis and characterization of 5-phenyl-1,2,4-oxadiazole-3-carboxylic acid (IP32)

To confirm the identity of a target compound in analytical studies, it is often required to synthesize a reference standard for direct comparison of fragmentation patterns and retention times. The synthesis of 5-phenyl-1,2,4-oxadiazole-3-carboxylic acid (IP32) was carried out specifically for this purpose, allowing verification of the analyte's identity by comparing its behavior in HPLC-MS analysis.

The synthesis begins with ethyl 5-phenyl-1,2,4-oxadiazole-3-carboxylate as the starting material, where sodium hydroxide facilitates the hydrolysis of the ester group, leading to the formation of the corresponding carboxylic acid (**Scheme 9**). Toluene, a non-polar solvent, provides an optimal medium for the reaction, allowing for effective mixing and interaction between the reactants. The 5-phenyl-1,2,4-oxadiazole-3-carboxylic acid is isolated by precipitation.

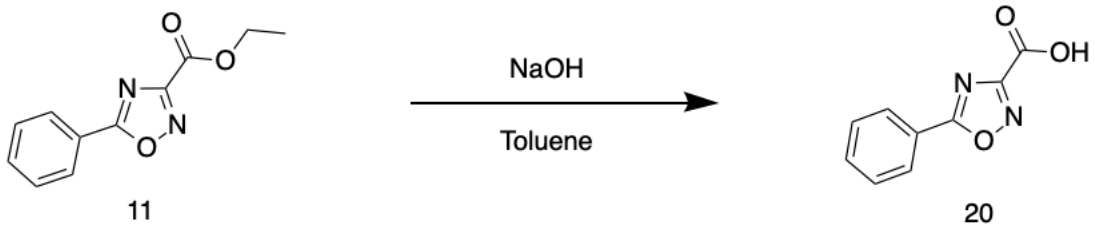

Scheme 9. *This scheme illustrates the hydrolysis of ethyl 5-phenyl-1,2,4-oxadiazole-3-carboxylate.*

Ethyl 5-phenyl-1,2,4-oxadiazole-3-carboxylate (**11**) was reacted with sodium hydroxide in toluene at room temperature for 24 hours, facilitating hydrolysis of the ester group and forming the corresponding carboxylate salts. After solvent removal under reduced pressure, the crude product was dissolved in water, and acidification caused compound (**20**) to precipitate out of solution, yielding 83%.

3.8 Evaluation of NV914's metabolic stability reveals no Phase I reactions

Metabolism plays a critical role in determining the fate of chemical compounds within biological systems, particularly drugs. In the context of pharmacology, understanding a drug's metabolic pathways is essential for predicting its efficacy, safety, and optimal dosage. The liver is the primary organ responsible for drug metabolism, where enzymes such as cytochrome P450 and UGT (Uridine 5'-diphospho-glucuronosyltransferase) catalyze the biotransformation of drugs into metabolites. These processes often render drugs either more active, inactive, or more suitable for excretion. *In vitro* models, such as liver microsomes, are widely used to simulate hepatic metabolism, providing an initial insight into how a drug candidate might behave *in vivo*. Early investigation of metabolic pathways in drug development allows for the identification of potential drug interactions, toxicities, and changes in pharmacokinetics, which aids in optimizing drug design and therapeutic strategies. In this study, the hepatic metabolism of NV914 is examined using HLMs, derived from 50 different donors, to simulate *in vivo* conditions and assess the metabolic degradation of NV914 over time.

Two experimental conditions were tested. The first condition consisted of NV914, microsomes, and phosphate buffer, while the second condition included additional components such as UDPGA, alamethicin, and magnesium chloride to specifically assess UGT activity (**Figure 20**).

A calibration curve was made with the same matrix to ensure accurate quantification of NV914 under experimental conditions (**Figure 21**).

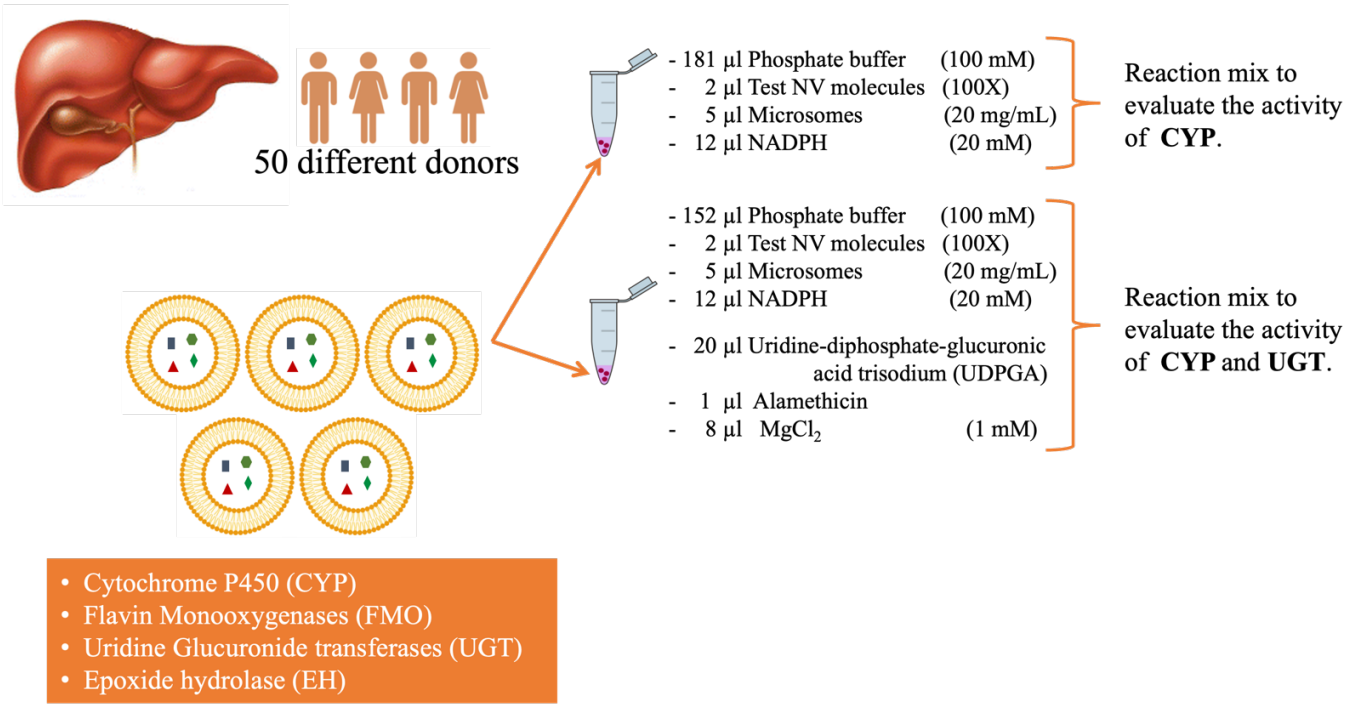

Figure 20. *Schematic representation of the experimental setup for metabolism assays. Condition 1 includes the test molecule, HLMs, and phosphate buffer to assess general metabolic stability. Condition 2 includes the test molecule, HLMs, phosphate buffer, UDPGA, alamethicin, and magnesium chloride to evaluate UGT-mediated glucuronidation activity.*

The experiment demonstrated that NV914 exhibits moderate stability against hepatic metabolism, with a reduction in concentration of approximately 46% over the course of one hour (**Figure 22 and 23**). Despite this decrease, no evidence of Phase I reactions was detected, and no glucuronide products were observed under the conditions designed to assess UGT activity. These results suggest that NV914 does not undergo significant phase I metabolism or phase II glucuronidation. The observed reduction in concentration may be attributed to other factors, such minor metabolic pathways. However, NV914 overall showed resilience against major hepatic metabolic processes.

Mixture no.1		
First Experiment		
Conc. µM		Signal
0,1	µM	166226
0,1	µM	176435
0,1	µM	146898
0,5	µM	232959
0,5	µM	247063
0,5	µM	230843
1	µM	309307
1	µM	309871
1	µM	308348
1,5	µM	404192
1,5	µM	408584
1,5	µM	399982

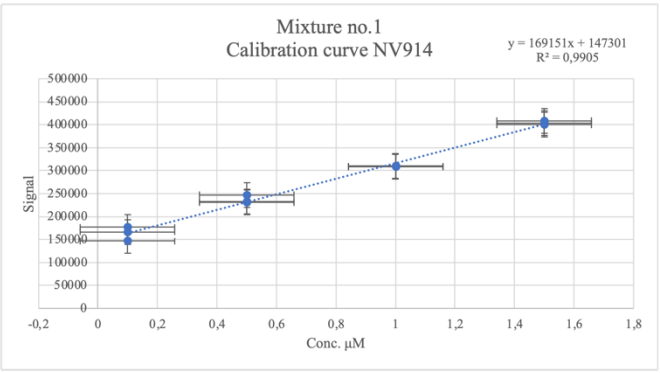

Mixture no.2		
First Experiment		
Conc. µM		Signal
0,1	µM	76543
0,1	µM	73467
0,1	µM	76743
0,5	µM	137922
0,5	µM	143664
0,5	µM	142154
1	µM	212690
1	µM	228665
1	µM	217092
1,5	µM	276129
1,5	µM	279873
1,5	µM	291529

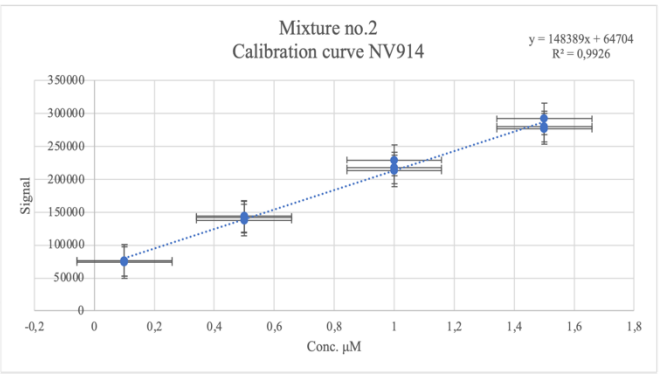

Mixture no.1		
Repeated Experiment		
Conc. µM		Signal
0,1	µM	222386
0,1	µM	224977
0,1	µM	222898
0,5	µM	271455
0,5	µM	265280
0,5	µM	261091
1	µM	330851
1	µM	328716
1	µM	339088
1,5	µM	384693
1,5	µM	392173
1,5	µM	391989

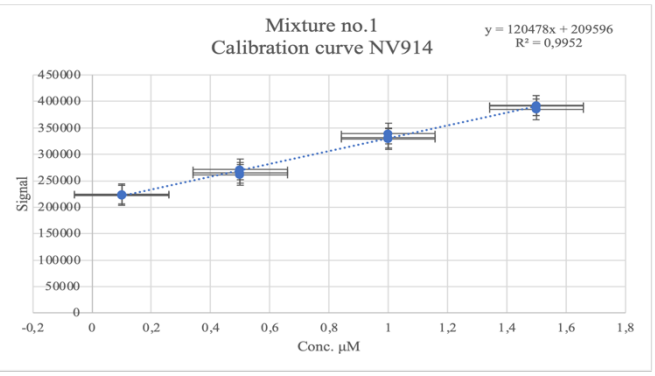

Mixture no.2		
Repeated Experiment		
Conc. µM		Signal
0,1	µM	67182
0,1	µM	67118
0,1	µM	65621
0,5	µM	198988
0,5	µM	193076
0,5	µM	201823
1	µM	297777
1	µM	299598
1	µM	296485
1,5	µM	430133
1,5	µM	432308
1,5	µM	436838

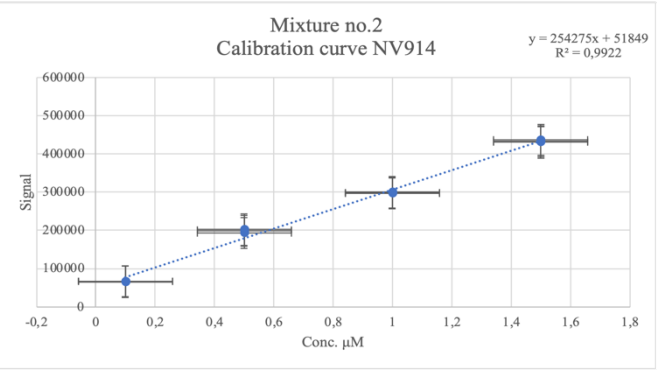

Figure 21. *Calibration curves were set to match the theorical concentration of 1,3 µM at time zero.*

Mixture no.1			
First Experiment			
Time	Signal	Average	Conc. µM
0 min	276704	367196,372	**1,3**
0 min	273766		
5 min	267044	350256,39	**1,2**
5 min	258031		
15 min	196851	273490,489	**0,7**
15 min	213143		
30 min	141971	226091,225	**0,5**
30 min	196966		
60 min	161942	214712,52	**0,4**
60 min	159937		

Mixture no.2			
First Experiment			
Time	Signal	Average	Conc. µM
0 min	205183	257610,351	**1,3**
0 min	203566		
5 min	211871	255928,238	**1,3**
5 min	194209		
15 min	180089	226135,488	**1,1**
15 min	178719		
30 min	155075	197220,665	**0,9**
30 min	157854		
60 min	128844	163129,042	**0,7**
60 min	129992		

Mixture no.1			
Repeated Experiment			
Time	Signal	Average	Conc. µM
0 min	271180	366217,488	**1,3**
0 min	264276		
5 min	259266	347921,524	**1,1**
5 min	249439		
15 min	239284	325259,313	**1,0**
15 min	236286		
30 min	247464	337109,868	**1,1**
30 min	245433		
60 min	208047	281416,982	**0,6**
60 min	203420		

Mixture no.2			
Repeated Experiment			
Time	Signal	Average	Conc. µM
0 min	209213	382406,86	**1,3**
0 min	209341		
5 min	195769	364717,914	**1,2**
5 min	203424		
15 min	176738	318553,61	**1,0**
15 min	171927		
30 min	153378	274893,589	**0,9**
30 min	147500		
60 min	132333	233803,631	**0,7**
60 min	123571		

Figure 22. *Normalized data according to recovery, showing the decrease in NV914 concentration over 1 hour.*

Mixture no.1			
First Experiment			
Time	Average	Conc. µM	Conc.%
0 min	275235	1,3	100%
5 min	262537,5	1,2	92%
15 min	204997	0,7	58%
30 min	169468,5	0,5	36%
60 min	160939,5	0,4	31%

Mixture no.1			
Repeated Experiment			
Time	Average	Conc. µM	Conc.%
0 min	366217,488	1,3	100%
5 min	347921,524	1,1	88%
15 min	325259,313	1,0	74%
30 min	337109,868	1,1	81%
60 min	281416,982	0,6	46%

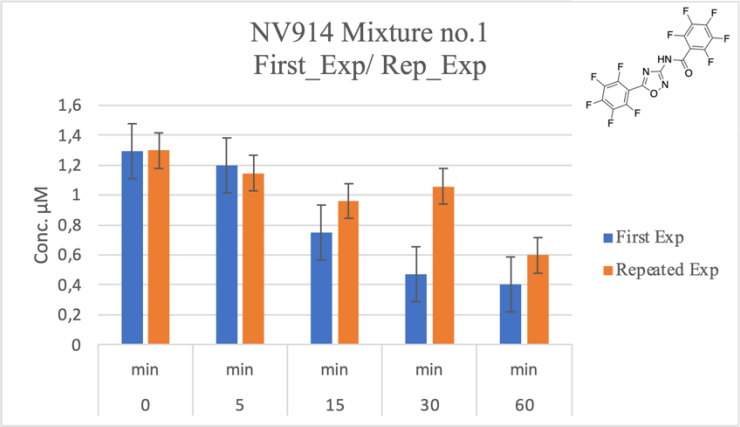

Mixture no.2			
First Experiment			
Time	Average	Conc. µM	Conc.%
0 min	204374,5	1,3	100%
5 min	203040	1,3	99%
15 min	179404	1,1	84%
30 min	156464,5	0,9	69%
60 min	129418	0,7	51%

Mixture no.2			
Repeated Experiment			
Time	Average	Conc. µM	Conc.%
0 min	209277	1,3	100%
5 min	199596,5	1,2	95%
15 min	174332,5	1,0	81%
30 min	150439	0,9	68%
60 min	127952	0,7	55%

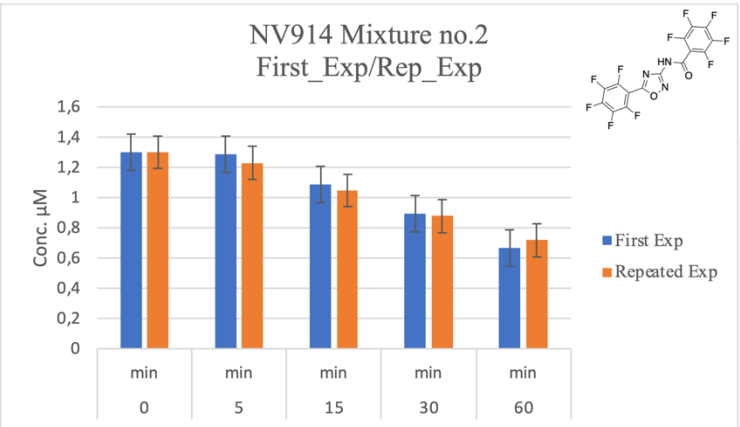

Figure 23. *Percentage metabolism of NV914 over one hour under both conditions for replicates.*

3.9 The study on HLMs of compound NV930 shows the molecule's low stability

The metabolic stability of NV930 was evaluated in HLMs, following a similar protocol to that of NV914, with minor adjustments. For this assay, only one experimental condition was applied, consisting of NV930, microsomes, and a phosphate buffer. Unexpectedly, when samples were analyzed, NV930 could not be detected at any time point, including at time zero, which suggested potential issues with compound recovery. Despite repeating the experiment under identical conditions, the results remained unchanged, pointing to possible instability or rapid degradation of NV930 in the reaction environment. To address this challenge, the concentration of NV930 in the stock solution was increased to 100 mM (**Figure 24**). In this case, NV930 was detected at the initial time points (0 and 5 minutes), but the signal was weak, falling below the lowest point of the calibration curve (**Figure 25**). Notably, HPLC-MS analysis revealed the presence of IP32, a corresponding carboxylic acid metabolite derived from ester bond hydrolysis. The identification of IP32 was confirmed by comparing its retention time and spectra with those of a synthesized IP32 standard under identical HPLC-MS conditions. Despite detecting IP32, the weak signal from NV930 prevented the normalization of recovery data or generate a detailed metabolic profile for the parent compound. This indicates that NV930 undergoes rapid hydrolysis in the reaction mixture, leading to the formation of IP32, the metabolite derived from ester bond cleavage.

First Experiment	
Conc. µM	Signal
5 µM	244914
5 µM	240001
5 µM	249125
25 µM	1127667
25 µM	1075409
25 µM	1109826
50 µM	1943962
50 µM	1870111
50 µM	1825863
100 µM	3090089
100 µM	3157686
100 µM	3156033

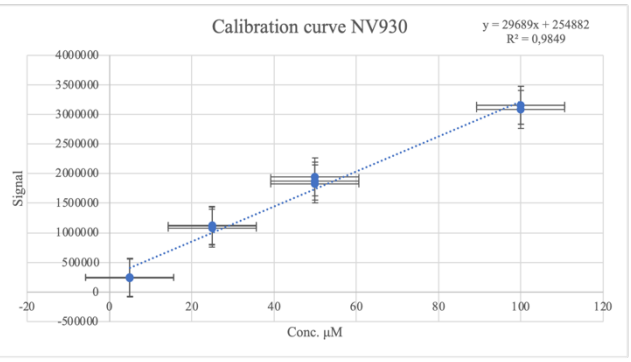

Repeated Experiment	
Conc. µM	Signal
5 µM	40694
5 µM	39466
5 µM	37364
25 µM	188300
25 µM	179260
25 µM	168024
50 µM	329568
50 µM	302137
50 µM	287083
100 µM	516774
100 µM	499288
100 µM	487456

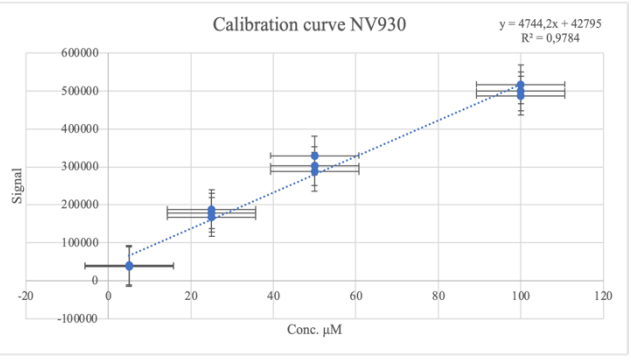

Figure 24. *Calibration curves were set to reflect the theoretical concentration of 65.22 µM at time zero.*

First Experiment			
Time	Signal	Average	Conc. µM
0 min	127794	124168	**-3,6568116**
0 min	120542		
5 min	6201	5141,5	**-7,6053772**
5 min	4082		
15 min	\		
15 min	\		
30 min	\		
30 min	\		
60 min	\		
60 min	\		

Repeated Experiment			
Time	Signal	Average	Conc. µM
0 min	\	\	
0 min	\	\	
5 min	8260	8395	**-6,12080231**
5 min	8530		
15 min	\	\	
15 min	\	\	
30 min	\	\	
30 min	\	\	
60 min	\	\	
60 min	\	\	

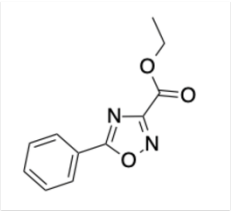

NV930

Figure 25. *Normalized data according to recovery was not possible due to inconsistent results in both experiments.*

From these findings, it was concluded that NV930 exhibits poor stability in the buffer solution used for the microsomal assay. It appears that NV930 undergoes rapid hydrolysis, likely due to the instability of an ester group within the molecule, leading to the formation of its corresponding carboxylic acid derivative, IP32. This suggests that phase I metabolism, specifically ester hydrolysis, plays a major role in the degradation of NV930. However, no phase II glucuronidation products were detected under the UGT-optimized conditions. These results indicate that NV930 is highly susceptible to hydrolysis in the presence of microsomes, with minimal resistance to hepatic metabolism.

3.10 Biodistribution analysis

Biodistribution studies are fundamental in drug development, providing essential data on how a drug distributes across various organs after administration. This information is crucial for understanding an aspect of the pharmacokinetic of a compound. By examining the biodistribution of a drug, it is possible to assess which organs are primarily involved in its uptake and retention, as well as how long it remains in circulation or in specific organs. Such insights are vital for determining the therapeutic potential of a compound, identifying possible off-target effects, and assessing the risk of toxicity, particularly in sensitive organs.

In this study, the biodistribution of three investigational compounds, NV848, NV914 and NV930, was evaluated using male C57BL/6 mice as the model organism. Toxicity studies previously conducted on these compounds in the same C57BL/6 mice model indicated no significant health risks. Specifically, NV848 and NV930 were classified as Category 4, and NV914 as Category 5, under the Globally Harmonized System (GHS) for Classification and Labeling of Chemicals, placing these compounds within a low-risk health profile. This biodistribution analysis, therefore, is a complementary study that examines the distribution of these compounds following oral administration and focuses on their concentrations in various organs over specified time points.

Monitoring the presence of these compounds across different organs and at various time intervals enabled a comprehensive evaluation of their pharmacokinetic profiles.
Since this was a single-dose treatment, the focus was on understanding the immediate distribution of these compounds rather than assessing long-term toxicity or accumulation. However, such data are essential for identifying potential target organs that would need to be closely monitored in future studies, particularly if the compounds were to be administered daily, which could reveal cumulative effects and highlight specific organ targets for therapeutic action.

3.10.1 Biodistribution profile of NV848: rapid clearance and hydrophilic behavior

Given the importance of biodistribution data in determining a compound's pharmacokinetic profile, the analysis of NV848 aimed to capture its unique distribution pattern following a single-dose administration.
Initial results from plasma analysis showed NV848's rapid systemic clearance, with concentrations peaking early post-administration and diminishing to low levels by 24 hours. Specifically, NV848 levels ranged from 0.05 µg/mL to 26 µg/mL in plasma, averaging 11.21 µg/mL at 45 minutes but decreasing to an average of 0.06 µg/mL by 24 hours (**Figure 26**). Concentration profiles in organs varied significantly, with some organs falling below the limit of detection (LOD), making it impossible to quantify. In the kidneys, NV848 was detected in two subjects at 145 ng/g and 794 ng/g after 45minute, while lung concentrations ranged between 421 ng/g and 1184 ng/g at this same time point, dropping below detectable levels within 2 hours. The pancreas showed more sustained concentrations through the first two hours, while the intestine displayed a high initial concentration (1018 ng/g to 8465 ng/g at 45 minutes), which declined after 2 hours, indicating rapid absorption. Interestingly, NV848 was detected in the brain at relatively high concentrations ranging from 4003 ng/g to 9969 ng/g at 45 minutes, later decreasing to 883 ng/g to 1587 ng/g by 2 hours. This distribution pattern raises the possibility of partial blood-brain barrier permeability, though NV848's low retention suggests limited long-term presence in brain tissue (**Figure 27**).
Recovery tests demonstrated variable extraction efficiencies across organs, likely due to NV848's interactions with specific matrix components. In some instances, recovery was not feasible, with rates ranging from 0% to 55%.

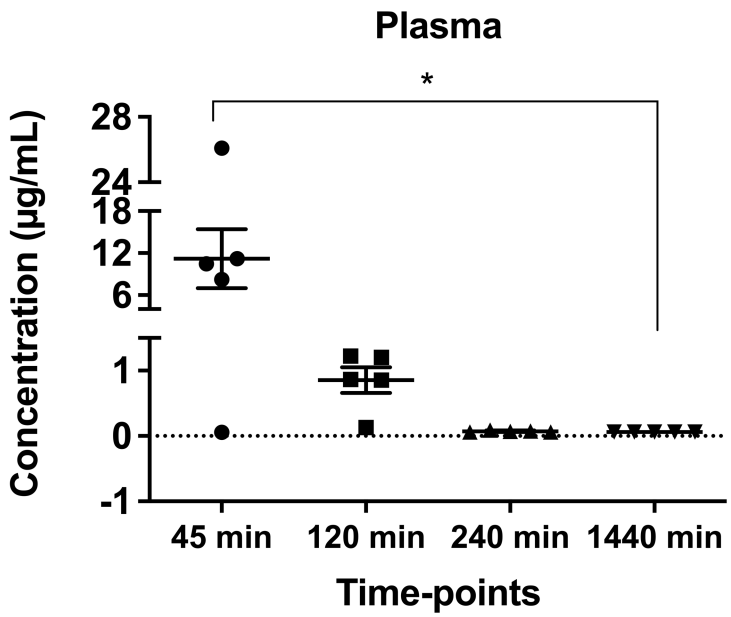

Figure 26. *Plasma concentration profile of NV848 following single-dose administration in mice (adapted from Fiduccia et al., 2024).*

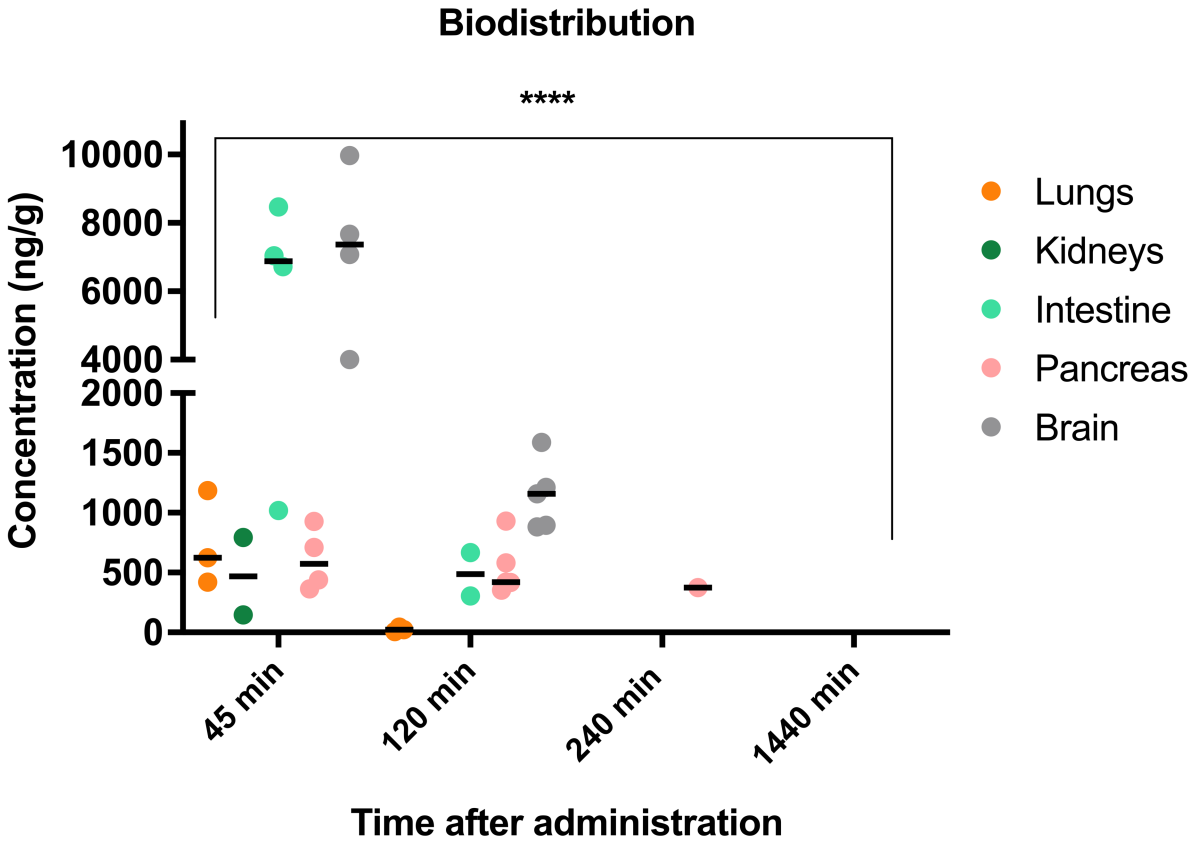

Figure 27. *Organ concentration profile of NV848 following single-dose administration in mice (adapted from Fiduccia et al., 2024).*

3.10.2 Biodistribution profile of NV914: limited absorption with high intestinal retention

These analyses were conducted similarly to those for NV848 but with some adjustments to the calibration curve. Although matrix-matching techniques are commonly used to mitigate matrix effects, they often require extensive sample preparation and many blanks. This approach can become time-consuming and resource-demanding, especially in studies with large sample sets or limited sample volumes.

In this study, an internal standard (IS) approach was selected for making the calibration curve aimed at quantifying NV914 concentrations across various organs. The IS method directly compensates for matrix effects within the samples, reducing the necessity for numerous blanks and simplifying sample preparation. Using an internal standard accelerated the workflow, leading to a more efficient process without compromising accuracy.

In plasma samples, NV914 was rarely detected; it appeared in only 2 samples out of 35, with measured concentrations of 27 ng/mL at 45 minutes and 227 ng/mL at 1 hour, indicating low systemic absorption (**Figure 28**).

Instead, NV914 displayed substantial retention in the intestine, reaching concentrations much higher than plasma levels. At 45 minutes, intestinal levels ranged from 0.7 µg/g to 187 µg/g, averaging 62 µg/g. Concentrations peaked around 1 hour, ranging from 37 µg/g to 156 µg/g with an average of 100 µg/g, and remained high up to 6 hours. After 24 hours, NV914 was detected in the intestine of only 1 mouse (37 µg/g), suggesting prolonged but gradually diminishing retention.

In the kidneys, NV914 reached an average concentration of 2152 ng/g at 45 minutes (ranging from 238 ng/g to 4361 ng/g) and maintained similar levels after 1 hour, averaging 1100 ng/g. The concentration peaked at 3 hours (average 9360 ng/g, ranging from 2715 ng/g to 13213 ng/g) before rapidly declining, with the compound detectable in only 2 mice at 4 hours and undetectable at subsequent time points.

Lung concentrations showed irregular patterns, with the compound detected in only a few mice. At 45 minutes, 1 mouse displayed a level of 800 ng/g, while another showed 1193 ng/g after 2 hours. Concentrations ranged around 1022 ng/g to 1183 ng/g at 3 hours, but a single mouse exhibited a high concentration of 44337 ng/g at 4 hours, considered an outlier due to lack of confirmation in other samples. Sporadic detections continued, with another outlier at 6 hours (173599 ng/g) and a single detectable level at 24 hours (9322 ng/g).

In the pancreas, NV914 was similarly detected only in a few subjects at 45 minutes (11360 ng/g and 22471 ng/g). Initial levels averaged 8445 ng/g at 1 hour, peaking at 3 hours with an average concentration of 46442 ng/g (ranging from 6774 ng/g to 72428 ng/g). By 4 hours, concentrations dropped, with levels detected in only 2 mice (460 ng/g and 10700 ng/g). Following this, the

analyte was observed in only a few mice, with concentrations of 6616 ng/g at 6 hours and 159 ng/g at 24 hours.

In brain samples, NV914 was detected in only 2 mice: one at 1 hour (18040 ng/g) and another at 4 hours (387 ng/g). No analyte was detected in liver samples despite repeated extraction attempts (**Figure 29**).

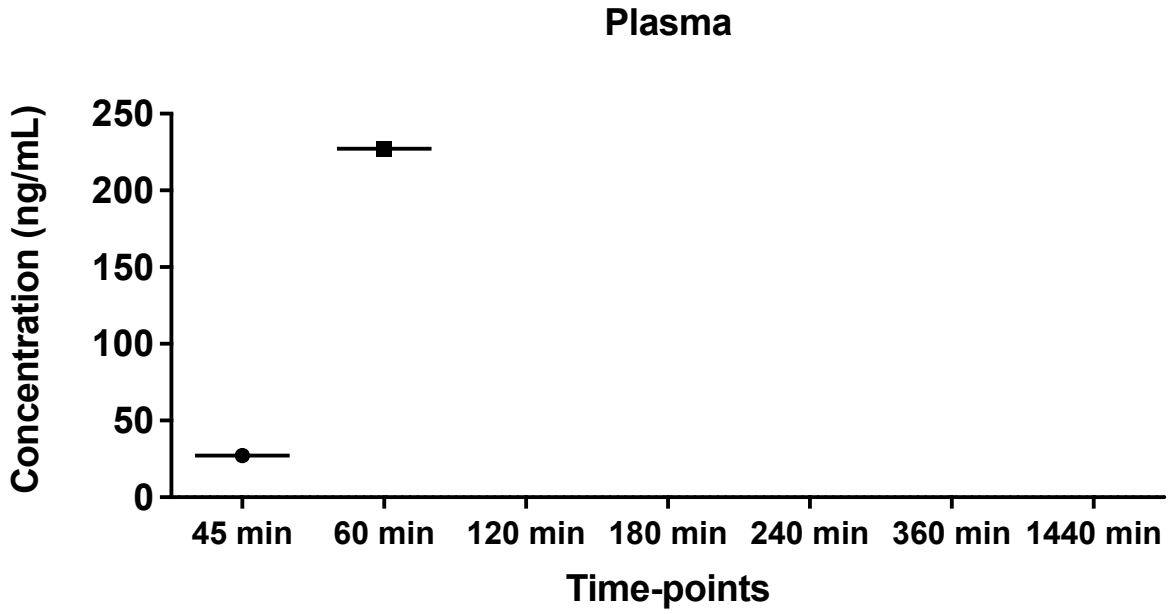

Figure 28. *Plasma concentration profile of NV914 following single-dose administration in mice.*

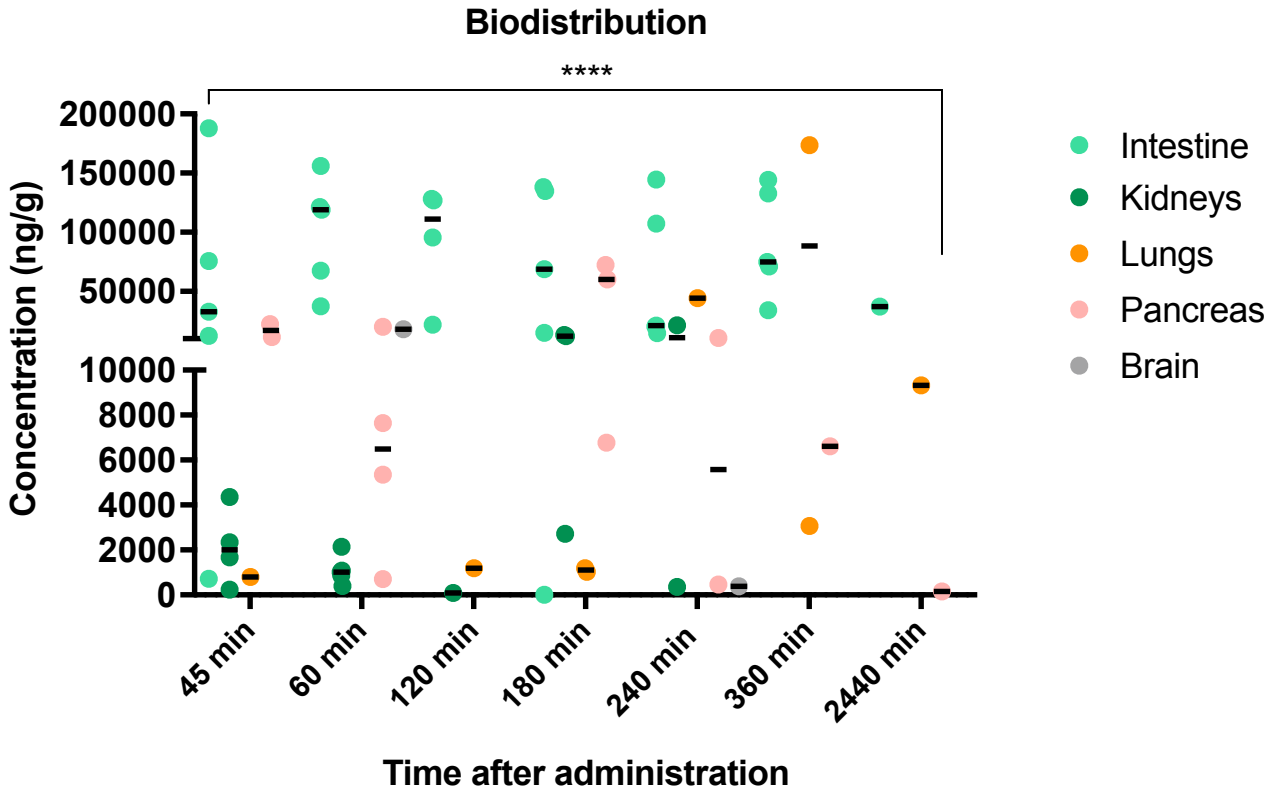

Figure 29. *Organ concentration profile of NV914 following single-dose administration in mice.*

3.10.3 Biodistribution profile of NV930: prolonged retention across some organs

Consistent with the analyses of NV914, the quantification of NV930 was carried out using a similar methodology. For the calibration curve, the isolated and purified compound IP30 was used as the IS in order to minimize potential matrix effects. Plasma analysis revealed NV930 concentrations ranging from 5 ng/mL to 202 ng/mL, with an average concentration of 74 ng/mL at 45 minutes post-oral administration. This high average concentration at the 45 minute is notably influenced by an outlier of 202 ng/mL. Without this outlier, the early concentration levels might suggest that NV930 is not yet fully absorbed, possibly due to the concurrent fat administration, which could delay or reduce absorption rates initially. By 120 minutes, the average plasma concentration dropped to 15 ng/mL (ranging from 4 ng/mL to 24 ng/mL), indicating absorption had not fully completed by 45 minutes. Beyond this initial phase, NV930 plasma levels stabilized, showing minimal variation from 4 to 24 hours. At 4 hours, concentrations ranged from 35 ng/mL to 90 ng/mL, and by 24 hours, they ranged from 60 ng/mL to 95 ng/mL, suggesting a sustained presence once absorption was complete (**Figure 30**).

Liver concentrations of NV930 were difficult to quantify due to matrix complexity. At 45 minutes, the compound was detected in only one mouse at 79 ng/g. After 2 hours, it was detected again in a single mouse at 0.95 ng/g, with concentrations rising after 4 hours (15 ng/g to 50 ng/g) and further increasing to 10 ng/g to 113 ng/g by 24 hours. Kidney concentrations ranged from 656 ng/g to 8983 ng/g at 45 minutes. After 2 hours, levels had already dropped to a range between 14 ng/g and 143 ng/g. By 4 hours, concentrations were between 41 ng/g and 670 ng/g, and the compound was still detectable at 24 hours, ranging from 79 ng/g to 1533 ng/g. In the lung, concentrations spiked at 45 minutes (1849 ng/g to 4430 ng/g), then declined to 52 ng/g to 1803 ng/g after 2 hours, to 88 ng/g to 231 ng/g by 240 minutes, and finally ranged from 159 ng/g to 2398 ng/g at 24 hours. The pancreas exhibited high concentrations initially, averaging 10221 ng/g at 45 minutes (266 ng/g to 10346 ng/g), which dropped to an average of 246 ng/g at 2 hours (14 ng/g to 799 ng/g) and 65 ng/g by 4 hours (22 ng/g to 152 ng/g). By 24 hours, pancreatic concentrations ranged from 73 ng/g to 301 ng/g. In the intestine, NV930 levels were initially high (653 ng/g to 3076 ng/g at 45 minutes) but decreased after 2 hours to an average of 299 ng/g (27 ng/g to 878 ng/g), continuing to decrease to an average of 102 ng/g by 4 hours (27 ng/g to 250 ng/g) and showed little further change up to 24 hours, with concentrations between 68 ng/g and 276 ng/g (**Figure 31**).

As observed with NV848 and NV914, extraction efficiency in recovery tests varied across organs due to NV930's interactions with matrix components, with recovery rates ranging from 0% to 44%, making quantification challenging in some cases.

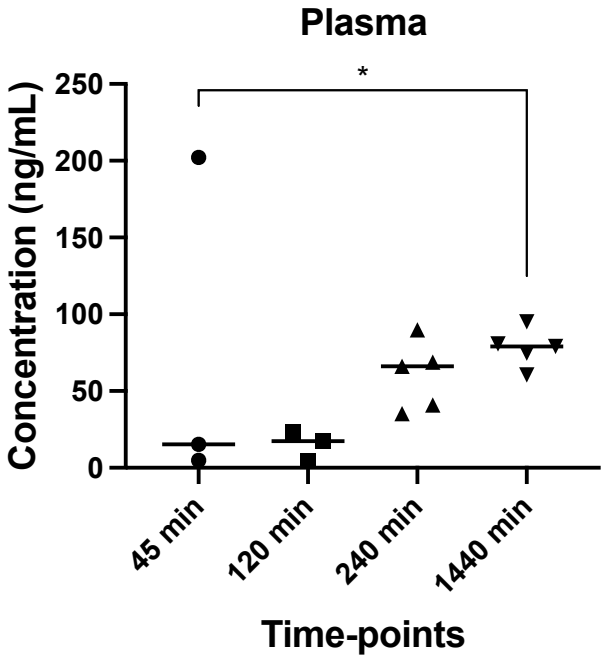

Figure 30. *Plasma concentration profile of NV930 following single-dose administration in mice.*

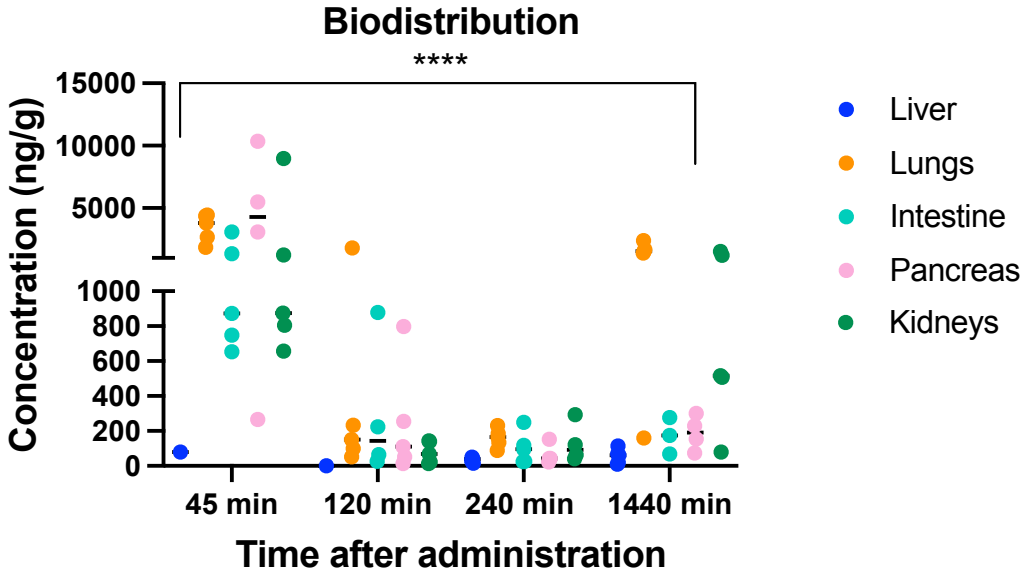

Figure 31. *Organ concentration profile of NV930 following single-dose administration in mice.*

The biodistribution analysis revealed distinct patterns for NV848, NV914, and NV930, each showing their potential to target specific organs and tissues. The small size and hydrophilic nature of NV848 led to its rapid absorption and efficient distribution throughout various tissues, including significant penetration into the brain. NV914 exhibited strong retention in the intestine, which is likely due to its lipophilic properties. NV930, while detected in several organs, showed

moderate concentrations, likely influenced by hepatic metabolism, and remained detectable for up to 24 hours. These differences in tissue distribution offer valuable insights into the potential therapeutic applications of each molecule, supporting their application for treating diseases related to specific organs.

3.11 Proteomic impact of NVs molecules on LRBA mutant fibroblasts

Proteomic studies offer clear advantages in understanding biological processes at a molecular level by providing direct insights into the functional state of proteins, which are the primary effectors in cells. A significant advantage of proteomic analysis is its ability to capture dynamic changes within the proteome, reflecting shifts in response to environmental factors, drugs, or disease progression.

In parallel with biodistribution studies, this research aims to investigate the impact of Ataluren and NV molecules on primary human fibroblasts harboring both homozygous and heterozygous nonsense mutation in the LRBA gene (**Figure 32**). This study is essential for understanding potential variations in protein expression, to concerning pathways involved in the recovery of a protein with a mutated endogenous gene and for evaluating any significant imbalances in the overall proteome.

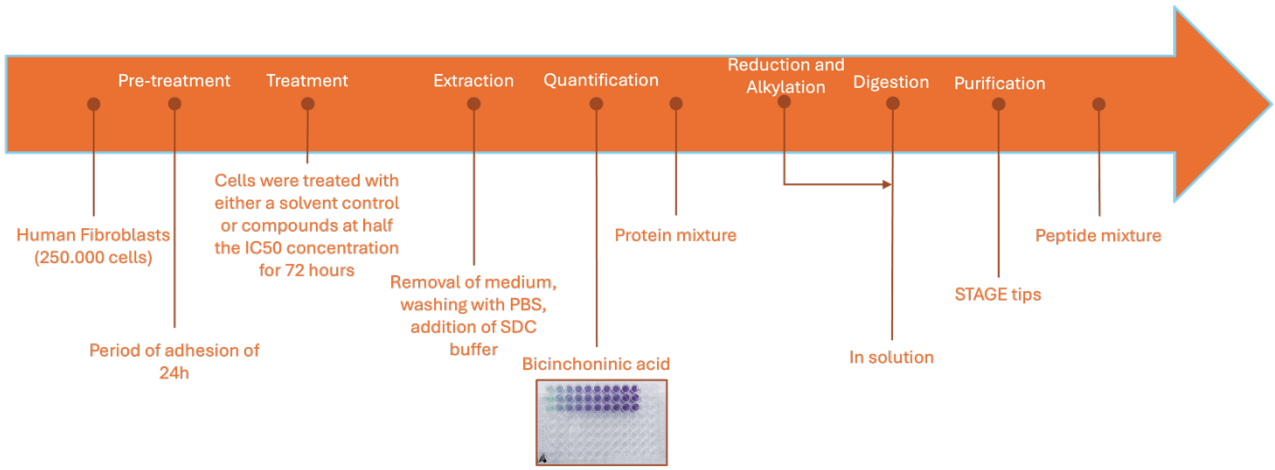

Figure 32. *Sample preparation steps for bottom-up proteomic analysis.*

3.11.1 Bottom-up proteomic analysis of LRBA$^{R1683X/R1683X}$ mutant fibroblasts.

To evaluate differential protein expression in fibroblast cell lines from an LRBA$^{R1683X/R1683X}$ homozygous patient and an LRBA$^{R1683X/WT}$ heterozygous sibling, label-free quantification (LFQ) was performed using Data-Dependent Acquisition (DDA) via nLC-MS/MS. Cells were treated

with 12 μM of NV848, NV914, NV930, or Ataluren for 72 hours, and protein expression profiles were analyzed by volcano plot, comparing untreated with treated conditions.

In the homozygous cell line, treatment with Ataluren (**Figure 33a**) resulted in no significant changes in protein expression, while treatments with NV848 (**Figure 33b**) and NV914 (**Figure 33c**) induced minimal shifts, showing 67 and 47 proteins with significant expression changes, respectively. NV930 treatment (**Figure 33d**) led to the differential expression of 865 proteins, with distinct patterns of upregulation and downregulation. Scatter plot analyses across biological replicates demonstrated reproducibility, with correlation coefficients typically >0.8, reinforcing the robustness of the LFQ-based proteomic data.

In contrast, the heterozygous cell line exhibited a broader response across all four treatments, with significant changes in protein expression observed under each condition. Specifically, treatment with Ataluren (**Figure 34a**) resulted in 1274 proteins with significant expression changes, NV848 (**Figure 34b**) impacted 1300 proteins, NV914 (**Figure 34c**) showed 1144 proteins with significant changes, and NV930 (**Figure 34d**) affected 1399 proteins.

Interestingly, the LRBA protein was not detected in either cell line, likely due to its low abundance in these samples. Given the DDA approach, which prioritizes high-abundance peptides, the non-detection of LRBA may reflect the relative abundance of this protein compared to other cellular proteins.

After establishing the differential effects of each treatment relative to the untreated condition, a comparison was carried out across treated conditions within each cell line to identify consistent changes in protein expression. This analysis aimed to determine whether specific protein expression patterns were commonly induced by multiple treatments, potentially indicating shared pathways or cellular processes underlying the response within either the homozygous or heterozygous fibroblasts. In the treated heterozygous cell line, a consistent response in protein expression variation was observed, with similar patterns evident across all conditions. In contrast, the homozygous cell line did not exhibit such uniformity in its response to the different treatments.

A subsequent comparison between the two cell lines was performed by examining each condition treated with the same molecule to identify whether up- or downregulation patterns were consistent across genotypes.

Notably, some treatments produced similar patterns of protein expression changes, either upregulated or downregulated, when comparing conditions treated with the same molecule. Additionally, certain treated conditions exhibited a greater overlap in protein expression changes. Among these shared proteins, particular attention was given to those involved in the LRBA pathway. While only a few proteins related to the LRBA pathway, such as RAB11A, a GTPase

involved in endosomal trafficking, were downregulated in the homozygous cell line, the majority of the significant changes were observed in the heterozygous cell line.

Several proteins were identified as being downregulated, including CDKN2A, RAB11A, PARP1, EGFR, CYCS, ARF1, CASP3, CASP8, and ARF6. Conversely, proteins such as CTBS, CD276, and MAP1 were found to be upregulated.

This clear difference underlines how the two genotypes respond to treatment in distinct ways. The heterozygous cells show a strong ability to react to the treatment and change their protein expression profile. In contrast, the homozygous cells maintain a more stable proteomic setting.

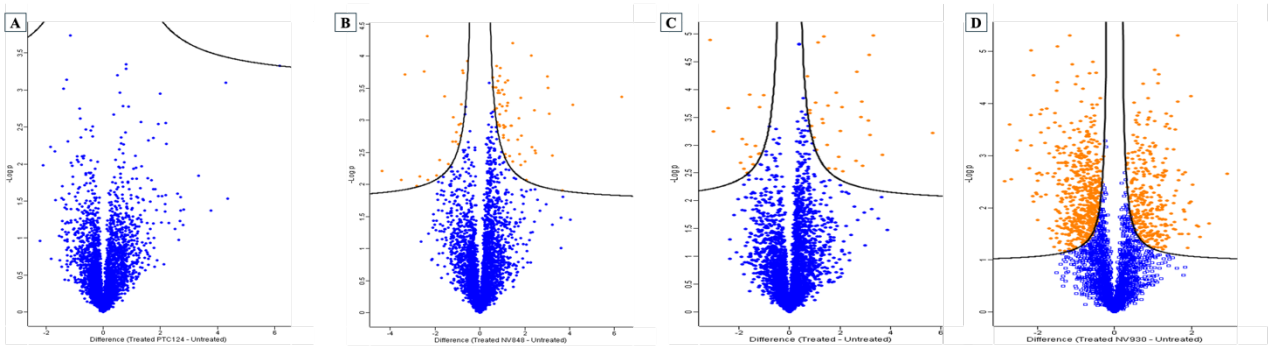

Figure 33. *Volcano plots represent differential protein expression in the homozygous cell line under each treatment. Plot A (PTC124) shows no significant changes, while Plot B (NV848) and Plot C (NV914) display minimal shifts in protein expression, with 67and 47 significant protein expression, respectively. Plot D (NV930) reveals distinct upregulation and downregulation of 865 proteins.*

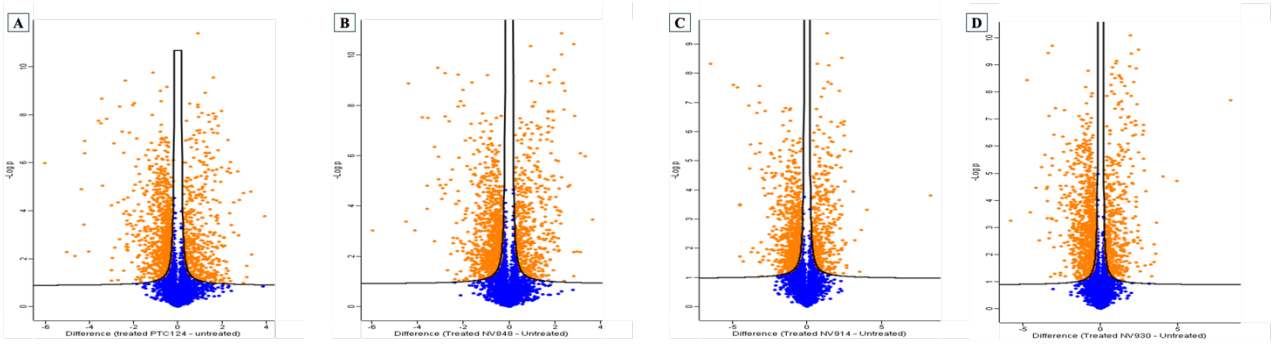

Figure 34. *Volcano plots represent differential protein expression in the heterozygous cell line under each treatment. Plot A (PTC124) shows 1274 proteins with significant expression changes, Plot B (NV848) shows 1300, Plot C (NV914) shows 1144, and Plot D (NV930) shows 1399 proteins with significant expression changes.*

3.12 Development of 3D Bioengineered skeletal muscle model

Recognizing the limitations of traditional models, this research focused on the potential of 3D bioengineered skeletal muscle models to provide more accurate representations of diseases. The experimental work aimed to develop a model for studying DMD. Before advancing to the 3D models, initial toxicity assays were conducted on 2D cultures to evaluate the safety of the synthesized compounds. The toxicity of NV848, NV914, NV930, and Ataluren was first assessed in the c.5758 C>T (p.Gln1920X) cell line, which harbors a UAG stop codon (**Figure 35**). The MTS assay involved testing ten different concentrations ranging from 1 µM to 500 µM.

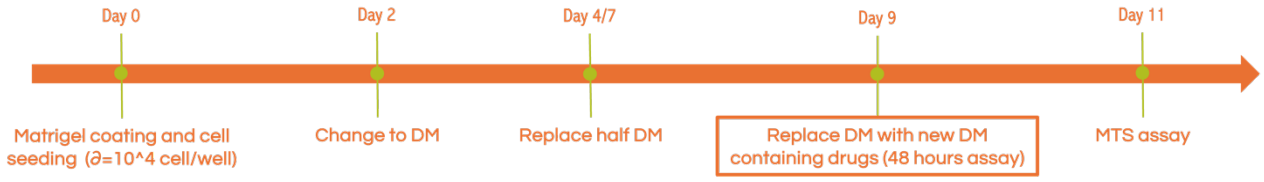

Figure 35. *MTS assay protocol. Molecules were administered to the differentiated cells and maintained in contact for 48 hours before performing the MTS assay.*

Among the four molecules examined, only NV914 exhibited toxic effects in the model showing a $logEC_{50}$ of 25.12 µM, allowing for the production of a dose-response curve. The remaining molecules were non-toxic, even at the highest concentration of 500 µM used in the experiment (**Figure 36**). It is worthy to note that all molecules were well tolerated at high concentrations in murine model.

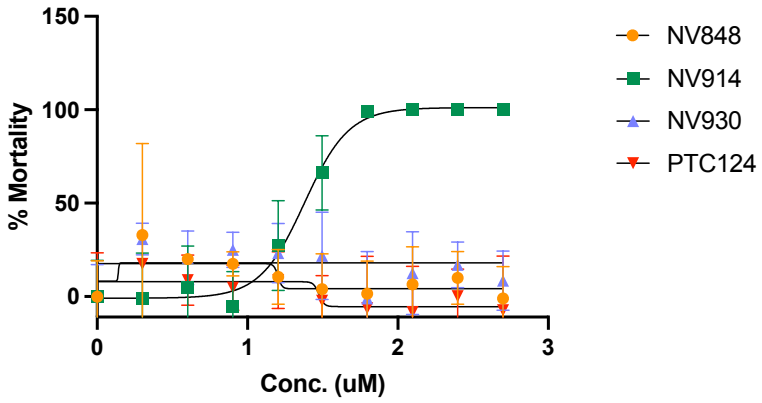

Figure 36. *Cell line c.5758 C>T (p.Gln1920X), containing a UAG stop codon, is used for toxicity assessment, with a LogEC50 of 25.12 µM for NV914.*

The experiment was replicated twice, and the toxicity was also evaluated in a different cell line, c.3556 G>T (p.Glu1186X), which carries a UAA stop codon. The MTS assay was conducted with five different concentrations ranging from 1 µM to 500 µM. Again, only NV914 exhibited toxic effects in the model showing a $logEC_{50}$ of 31.43 µM (**Figure 37**).

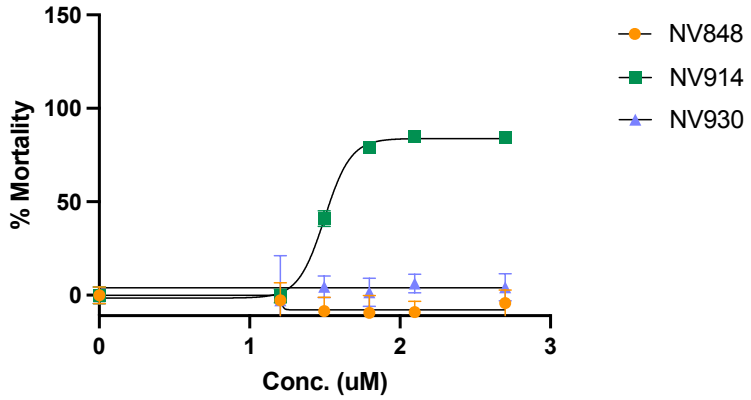

Figure 37. *c.3556 G>T (p.Glu1186X) containing a UAA stop codon, is used for toxicity assessment, with a LogEC50 of 31.43 µM for NV914.*

After establishing the safety range for the synthesized molecules, In-Cell Western (ICW) assays were conducted on the c.5758 C>T (p.Gln1920X), c.3556 G>T (p.Glu1186X) c. 8713 C>T (p.Arg2905X) cell lines to evaluate dystrophin protein expression (**Figure 38**). ICW assays merge the specificity of Western Blotting with the high throughput of ELISA. One of the key advantages of the ICW assay is its ability to gather reproducible data across multiple experimental conditions and replicates. This method allows for the detection of proteins in fixed and permeabilized cells using target-specific primary antibodies and IRDye® secondary antibodies.

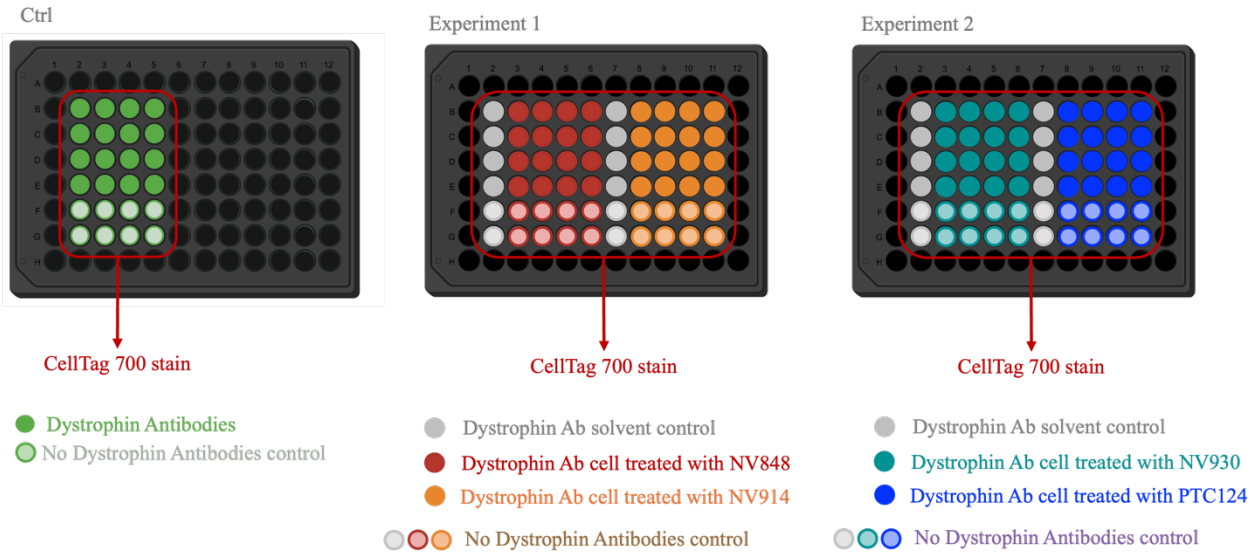

Figure 38. *The left 96-well plate contains a wild-type muscle cell line used to validate the protocol and assess dystrophin expression. The middle and right 96-well plate outline the experimental conditions for both Experiment 1 and Experiment 2, with each column representing a specific treatment. From left to right, conditions include a solvent control (water for NV848, DMSO for NV914, NV930, and PTC124 at a final concentration of 0.1%) followed by treatments with molecules at concentrations of 8 µM, 16 µM, 31.3 µM, and 62 µM.*

Results indicated no measurable increase in dystrophin protein levels under the chosen treatment conditions (**Figure 39**).

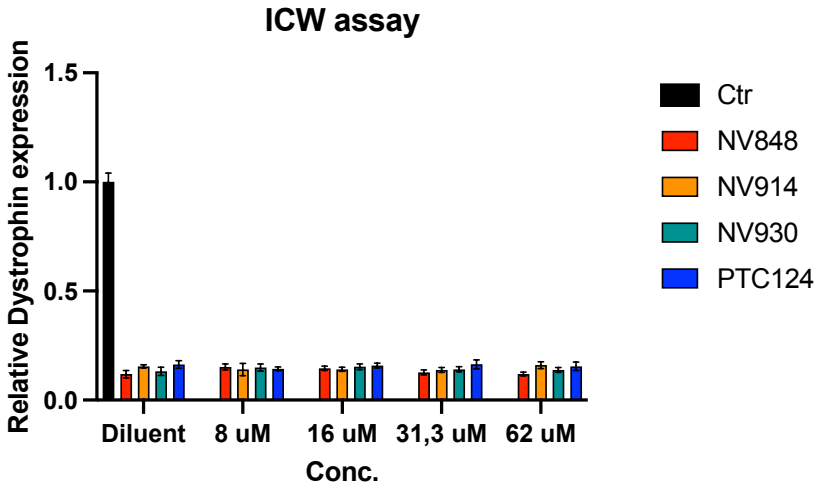

Figure 39. *ICW results showing no difference in term of dystrophin expression between untreated and treated cell line.*

The assay was repeated, but the results remained consistent, showing no difference in dystrophin protein levels between the untreated and treated conditions in the DMD cell line.

In response to these findings, the experimental protocol was adjusted to administer the drugs immediately after transitioning to DM. This time, the cell line c. 8713 C>T substitution (p.Arg2905X), with a UGA stop codon, was used for the experiment. The positive control was switched from Ataluren to G418, expecting to achieve a more pronounced readthrough response. Following this modification, dystrophin was successfully detected after ten days of differentiation period (**Figure 40a**) and the results were validated by repeating the experiment (**Figure 40b**).

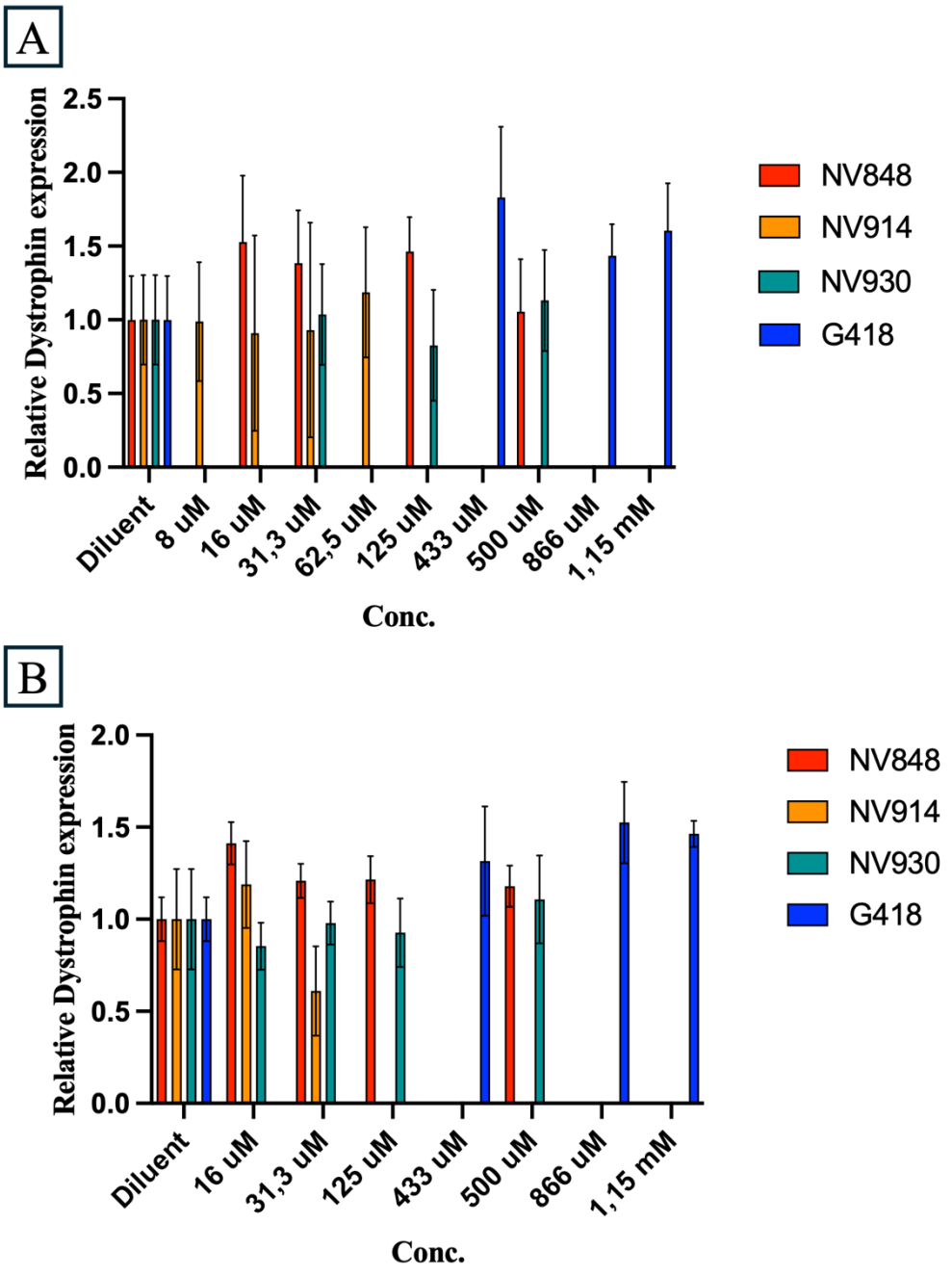

Figure 40. *ICW results show readthrough activities of NV848 and G418. NV848 exhibited its highest readthrough efficiency at 16 µM, while G418 reached its peak activity at 866 µM.*

Once both toxicity and efficacy were assessed in 2D cultures, the next step involved transitioning to a 3D bioengineered skeletal muscle model (**Figure 41**).

After seven days of differentiation, cells were electrically stimulated to induce contraction and rupture of the sarcolemma in DMD cells. Upon stimulation, the cells were divided into distinct experimental conditions. One group remained untreated and the other groups received treatment with NV848 at concentrations of 16 µM and 31 µM, along with G418 at a concentration of 433 µM. Samples were allowed to incubate for 48 hours.

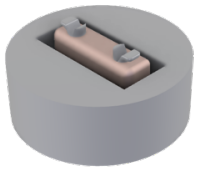

Figure 41. *Casting molds designed with a rectangular reservoir for seeding the cell/hydrogel solution, with two vertical, flexible PDMS pillars.*

The 3D bioengineered skeletal muscle model shows great promise as a more accurate representation of DMD. However, the experimental results revealed a concerning lack of significant increases in dystrophin expression in response to the synthesized compounds (**Figure 42 and 43**). This raises important questions about the factors influencing these outcomes and the overall effectiveness of the model.

The challenges encountered during this study underline the need for further optimization of the model and experimental protocols. Moving forward, refining the differentiation process, exploring alternative cell lines, and adjusting treatment strategies may enhance the model's effectiveness. Ultimately, this research paves the way for future studies aimed at developing targeted therapies for DMD, reinforcing the importance of continued exploration in this vital area of biomedical research.

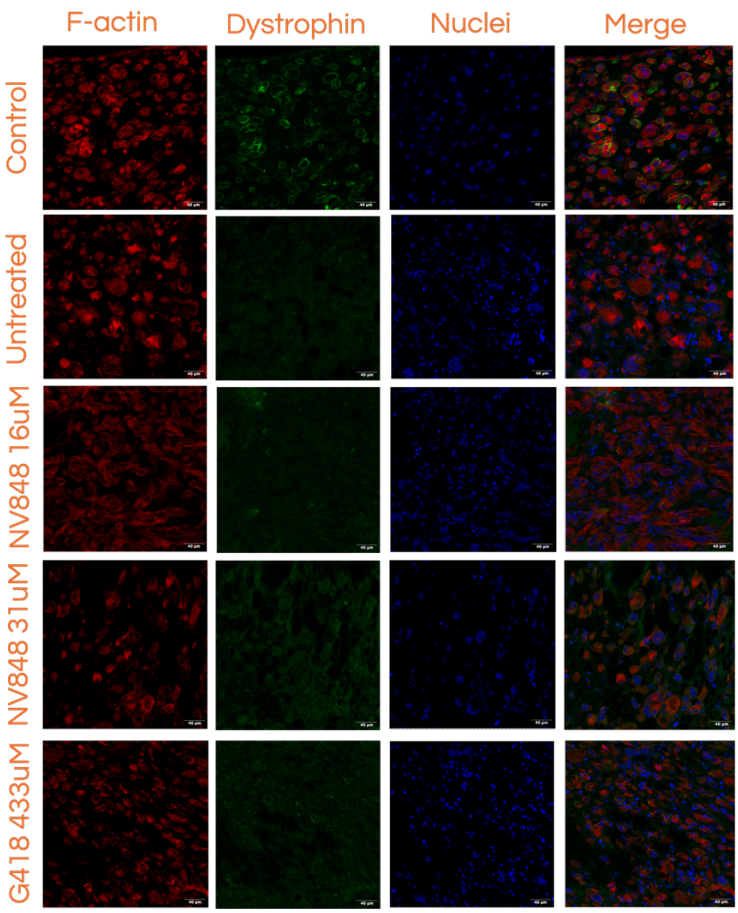

Figure 42. *Immunostaining of 3D muscle tissue reveals distinct differences in protein expression. The control sample is a wild-type cell line expressing dystrophin, while the other samples represent various conditions of the same cell line harboring a nonsense mutation.*

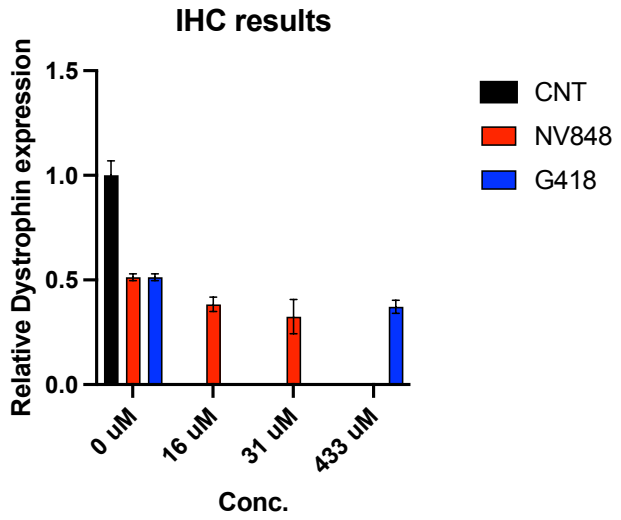

Figure 43. *Immunostaining results demonstrate a significant reduction in cell vitality for those treated with compounds compared to the untreated control group.*

4 Conclusions

This project has highlighted the varied metabolic, biodistribution, and cellular responses elicited by NV914, NV930, and NV848, illustrating their therapeutic promise and the challenges of drug stability, targeting, and cell impact. The advancements in synthetic methods further strengthen their potential by addressing critical production inefficiencies, ensuring higher yields of the final products.

The initial synthetic routes for NV848 and NV914, though functional, were marked by significant challenges, including low yields and by-products formation. For NV848, optimization of reaction conditions led to a marked improvement in overall yield, from an initial 18% to a more efficient 46%. These advancements minimized side reactions, including undesirable rearrangements, thereby enhancing the scalability and reproducibility of the synthesis. Similarly, the synthetic route for NV914 was improved by implementing thermoregulated conditions during the cyclization step, significantly reducing the formation of impurities and enhancing the overall yield. These refinements demonstrate a clear progression towards more efficient and practical production of these compounds.

The synthesis of NV930, in contrast, did not require optimization due to its already high yield and straightforward preparation.

The metabolic studies revealed that NV914 has moderate hepatic stability, comparable to ataluren and slightly lower than NV848. No signs of significant Phase I or Phase II metabolism have been shown. This suggests that NV914 is quite resilient against major hepatic clearance pathways, making it a promising candidate for situations where sustained bioavailability is crucial. In contrast, NV930 displayed a high susceptibility to hepatic metabolism, rapidly undergoing ester hydrolysis to convert into its carboxylic acid form, IP32.

Biodistribution studies showed a clearer picture of how NV848, NV914, and NV930 target specific organs, providing valuable insights for tissue-specific drug delivery. NV848, for example, was found to rapidly enter the bloodstream and penetrate various tissues, including the brain. This is particularly interesting for treating neurological or brain-related genetic disorders. On the other hand, NV914 showed strong retention in the intestine with lower levels in the brain, hinting at its potential applications in gastrointestinal diseases or conditions related to the intestine. Meanwhile, NV930 was detected in several organs up to 24 hours, although at moderate concentrations, likely due to its hepatic metabolism.

By proteomic analysis, the impact of NV molecules was assessed in two different cell types: i) human primary fibroblasts harboring a homozygous nonsense mutation in the endogenous LRBA gene $LRBA^{R1683X/R1683X}$ and ii) heterozygous $LRBA^{R1683X/WT}$ human primary fibroblasts.

In homozygous cells, only limited changes in protein expression were observed, with NV930 producing the most pronounced effect. In contrast, heterozygous cells exhibited a major differential protein expression under all treatments.

Whereas a human cell contains tens of thousands of types of proteins, the variations observed following treatments represent a very small percentage. This is a crucial finding from the therapeutic point of view, since it suggests that treatments do not cause significant alterations in the overall protein balance of the cell, minimizing the risk of side effects.

The 3D bioengineered tissue model, developed using primary DMD patient-derived myotubes, was designed to simulate DMD pathology through electrical stimulation. While previous 2D culture studies showed that dystrophin rescue typically requires prolonged treatment, this 3D model was designed with a different approach: to test whether dystrophin expression could be triggered within a shorter, 48-hour treatment window following stimulation. This choice was based on literature search, suggesting that after sarcolemmal damage, the cellular demand for dystrophin increases significantly. By applying treatment right after stimulation (which induces sarcolemma rupture), the experiment aimed to determine if this increased demand might accelerate dystrophin expression within a shorter timeframe. However, the anticipated dystrophin rescue was not observed, indicating that immediate post-damage conditions alone were insufficient. In this case, further experiments would be necessary with implemented protocols, mimicking the conditions used for the 2D screening to be able to assess the effective rescue of dystrophin protein.

5 Material and methods

Reagents and solvents were obtained from commercial suppliers. Melting points were measured using Axio imager.A2m microscope (Carl Zeiss, Göttingen, Germany) equipped with a Linkham hot-stage LTS420E with a Linkpad T95-LTS processor to control the temperature. ^{1}H NMR spectra were recorded on a Bruker Avance spectrometer operating at 400 MHz. Sample purification was carried out via flash chromatography on silica gel (Merck, 0.040–0.063 mm particle size). HRMS spectra were acquired by analyzing sample solutions with an Agilent 6540 UHD Accurate-Mass Q-TOF LC/MS equipped with a Dual AJS ESI source. All spectroscopic and spectrometric characterization details are provided in Appendix A.

Chemistry.

Synthesis of *3-acetylamino-5-methyl-1,2,4-oxadiazole* (***NV848***)

Synthesis of *acetylcyanamide*

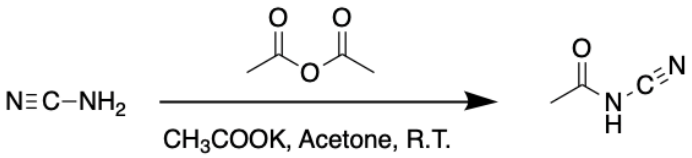

Cyanamide (2.0 g, 47.56 mmol) was dissolved in acetone, followed by the addition of acetic anhydride (6.74 mL, 71.34 mmol) and potassium acetate (7.0 g, 71.34 mmol). The reaction mixture was stirred at room temperature for 24 hours. Upon completion, the reaction mixture was filtered to remove the salts, and acetone was removed under reduced pressure, yielding acetylcyanamide as a near-quantitative product (~100% yield).

Synthesis of *3-amino-5-methyl-1,2,4-oxadiazole*

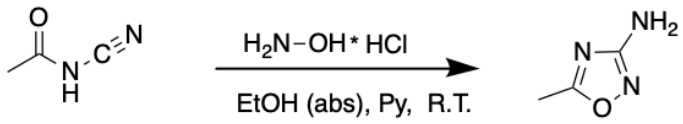

The resulting acetylcyanamide was dissolved in ethanol absolute. Hydroxylamine hydrochloride (4.96 g, 71.34 mmol) and pyridine (5.75 mL, 71.34 mmol) were then added, and the reaction mixture was stirred at room temperature for 24 hours. After completion, the solvent was evaporated under reduced pressure.

The residue was subjected to liquid-liquid extraction. The aqueous phase was extracted three times with ethyl acetate (3 x 100 mL). The combined organic phases were dried over anhydrous

sodium sulfate (Na_2SO_4), filtered, and the solvent was removed under vacuum to yield the crude product.

The crude product was purified by column chromatography using petroleum ether/ethyl acetate (2:1) as the mobile phase. This process yielded the pure 3-amino-5-methyl-1,2,4-oxadiazole.

Synthesis of ***NV848***

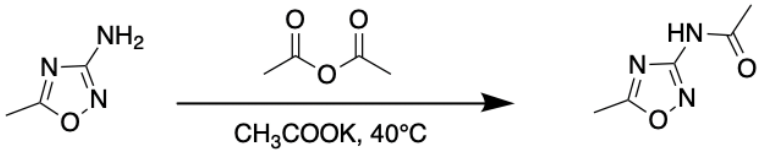

In a solvent-free setup, 3-amino-5-methyl-1,2,4-oxadiazole was treated with acetic anhydride (6.74 mL, 71.34 mmol) and potassium acetate (7.0 g, 71.34 mmol) at 40°C for 24 hours. After completion, the crude product was purified by column chromatography using a petroleum ether/ethyl acetate gradient (starting with 2:1, then moving to 1:1).

NV848: Reaction yield 46%, MP 162–163 °C. ^{1}H NMR (DMSO-d6) δ (ppm): 2.08 (s, 3H), 2.52 (s, 3H), 10.94 (s, 1H). HRMS for $C_5H_7N_3O_2$ found 142.0625 $[M + H]^+$ (Calcd. 142.0611).

Synthesis of *3-pentafluorobenzoylamino-5-perfluorophenyl-1,2,4-oxadiazole (**NV914**)*

Synthesis of *2-hydroxyguanidine*

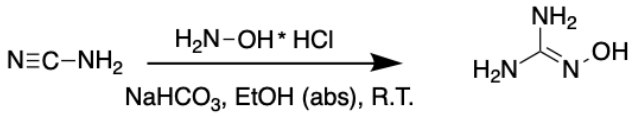

Hydroxylamine hydrochloride (3.30 g, 47.56 mmol) was dissolved in ethanol absolute (20 mL) in a round-bottom flask and stirred for 10 minutes to fully dissolve. Sodium bicarbonate (4.0 g, 47.56 mmol) and cyanamide (2.0 g, 47.56 mmol) were then added to the flask. The reaction mixture was stirred at room temperature for 24 hours. Reaction progress was monitored by thin-layer chromatography (TLC) to confirm the complete consumption of the reactants.

Once the reaction was complete, the solvent was evaporated under reduced pressure, yielding a crude product.

Synthesis of *3-amino-5-perfluorophenyl-1,2,4-oxadiazole*

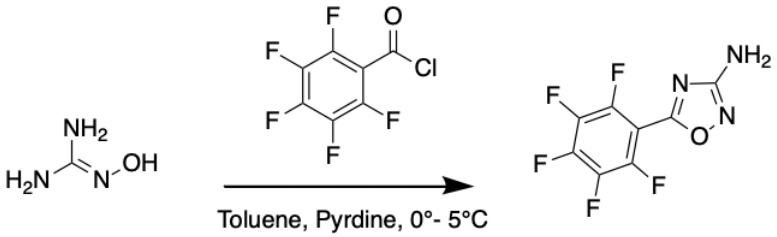

This crude product was used directly in the next step for the synthesis of 3-amino-5-perfluorophenyl-1,2,4-oxadiazole. The flask containing the crude mixture was placed in an ice bath, and 2,3,4,5,6-pentafluorobenzoyl chloride (11.20 mL, 71.34 mmol) and pyridine (5.75 mL, 71.34 mmol) were slowly added, ensuring the temperature remained below 5°C. The reaction mixture was stirred at this temperature for 48 hours. After 48 hours, TLC analysis indicated the disappearance of 2-hydroxyguanidine.

Synthesis of ***NV914***

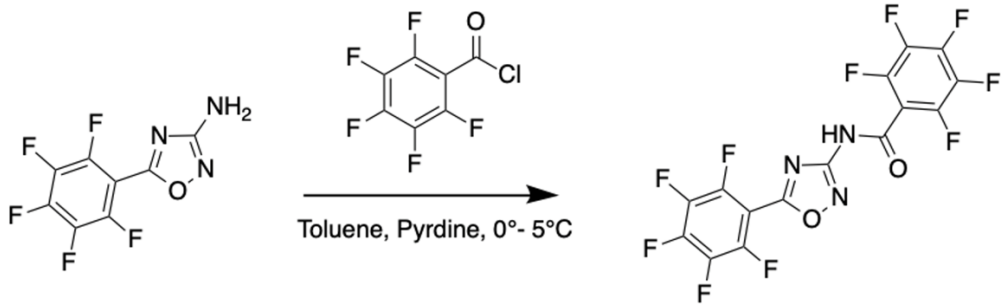

Pentafluorobenzoyl chloride (7.46 mL, 47.56 mmol) and pyridine (3.84 mL, 47.56 mmol) was added to the flask, and the reaction was allowed to proceed overnight while maintaining the temperature below 5°C to minimize side-product formation.

After 24 hours, TLC confirmed the formation of 3-pentafluorobenzoylamino-5-perfluorophenyl-1,2,4-oxadiazole and nearly complete consumption of 3-amino-5-perfluorophenyl-1,2,4-oxadiazole. The solvent was removed by vacuum, and the crude product was subjected to liquid-liquid extraction. The aqueous phase was extracted three times with ethyl acetate (3 x 100 mL).

For further purification, additional liquid-liquid extractions were performed using a basic aqueous phase. The pH of the aqueous phase was monitored after each extraction, and sodium hydroxide (NaOH) was added as needed to maintain the pH between 7 and 8. Once the pH stabilized in this range, the extractions were stopped.

The organic phase was dried over anhydrous sodium sulfate (Na_2SO_4), filtered, and the solvent was removed under vacuum. The crude product was purified by column chromatography using a petroleum ether/ethyl acetate gradient, starting at a 10:1 ratio and gradually shifting to 5:1. Final

purification was achieved by recrystallization from ethanol, yielding pure 3-pentafluorobenzoylamino-5-perfluorophenyl-1,2,4-oxadiazole.

NV914: Reaction yield 31%, MP 209-210 °C. ^{1}H NMR (DMSO-d6) δ (ppm): 2.08 (s, 3H), 2.52 (s, 3H), 10.94 (s, 1H). HRMS for $C_{15}HF_{10}N_3O_2$ found 445.9989 $[M + H]^+$ (Calcd. 445.9982) and 467.9809 $[M+Na]^+$ (Calcd. 467.9801).

Synthesis of *ethyl 5-phenyl-1,2,4-oxadiazole-3-carboxylate (**NV930**)*

Synthesis of *ethyl-2-amino-2-(hydroxyimino)acetate*

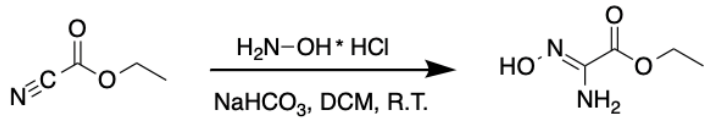

Ethyl cyanoformate (1.5 g, 15.13 mmol) was dissolved in dichloromethane (20 mL) in a round-bottom flask. Hydroxylamine hydrochloride (1.05 g, 15.13 mmol) and sodium bicarbonate (1.27 g, 15.13 mmol) were then added, and the reaction mixture was stirred at room temperature for 24 hours. The reaction was monitored by TLC using a mobile phase of petroleum ether and ethyl acetate 2:1. After completion, the solution was filtered to remove salts, and the product was obtained by crystallization through the addition of cold petroleum ether, yielding ethyl-2-amino-2-(hydroxyimino)acetate.

Synthesis of *ethyl-2-amino-2-((benzoyloxy)imino)acetate*

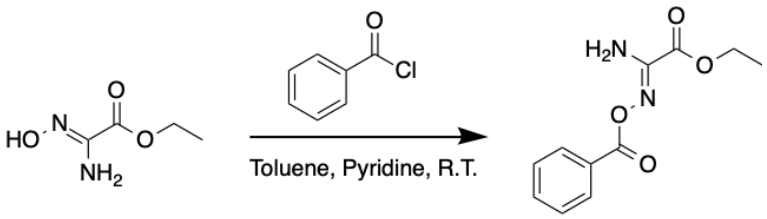

Ethyl-2-amino-2-(hydroxyimino)acetate (1.6 g, 12.11 mmol) was dissolved in toluene (15 mL), followed by the addition of benzoyl chloride (2.11 mL, 18.17 mmol) and pyridine (1.46 mL, 18.17 mmol). The reaction mixture was stirred at room temperature for 24 hours. After completion, the solvent was removed under reduced pressure. The crude product was subjected to liquid-liquid extraction, with the aqueous phase extracted three times using ethyl acetate (3 x 100 mL). The combined organic phases were dried over anhydrous sodium sulfate (Na_2SO_4), filtered, and the solvent was removed under vacuum.

The crude product was dissolved in ethanol and purified by crystallization, yielding pure ethyl-2-amino-2-((benzoyloxy)imino)acetate.

Synthesis of ***NV930***

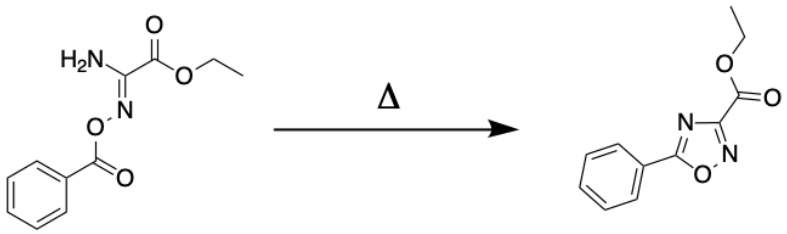

ethyl-2-amino-2-((benzoyloxy)imino)acetate (2.5 g, 10.58 mmol). was then transferred to a high-pressure tube and heated in an oil bath at 165°C for 2 hours, leading to dehydration and the formation of NV930.

The crude NV930 was purified by column chromatography using a petroleum ether/ethyl acetate gradient (5:1). Final purification was achieved by recrystallization from ethanol, yielding pure ethyl 5-phenyl-1,2,4-oxadiazole-3-carboxylate (1.7 g, 7.79 mmol).

NV930: Reaction yield 52%, MP 64-65 °C. ^{1}H NMR (DMSO-d6) δ (ppm): 8.16 (d, 2H), 7.80 – 7.71 (m, 1H), 7.66 (t, 2H), 4.45 (q, 2H), 1.36 (t, 3H). HRMS for $C_{11}H_{10}N_2O_3$ found 219.0772 $[M + H]^+$ (Calcd. 219.0764) and 241.0587 $[M+Na]^+$ (Calcd. 241.0584).

Synthesis of *Ataluren (**PTC124**)*

Synthesis of methyl 3-cyanobenzoate

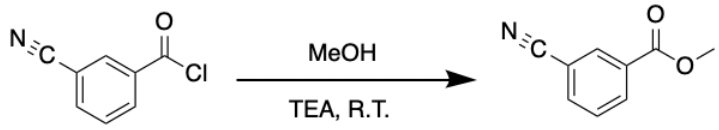

The reaction was initiated by adding 3-cyanobenzoyl chloride (1.0 g, 6.04 mmol), triethylamine (TEA, 1.68 mL, 12.08 mmol), and methanol (10 mL) to a round-bottom flask. The mixture was stirred at room temperature overnight. After 24 hours, the reaction was monitored by thin-layer chromatography (TLC) using a 2:1 ratio of petroleum ether and ethyl acetate, confirming the formation of methyl 3-cyanobenzoate. The solvent was then removed under reduced pressure.

Liquid-liquid extraction was performed with water and diethyl ether, repeating the extraction three times. The combined organic layers were dried over sodium sulfate (Na_2SO_4), filtered, and the solvent was evaporated under reduced pressure. The product was isolated by column chromatography with a yield of 94%.

Synthesis of *methyl 3-(N'-hydroxycarbamimidoyl)benzoate*

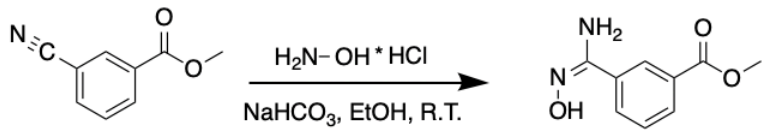

In the next step, hydroxylamine hydrochloride (0.61 g, 8.84 mmol) and sodium bicarbonate (0.74 g, 8.84 mmol) were added to a flask containing 10 mL of water. The mixture was stirred for 10 minutes to fully dissolve the solids and ensure proper solubilization. Methyl 3-cyanobenzoate (0.95 g, 5.9 mmol) was then added and ethanol absolute was used as the solvent. The reaction was stirred overnight at room temperature, and after 24 hours, progress was checked by TLC. Upon complete consumption of the reactants, the solvent was removed under vacuum, and a standard workup was performed involving liquid-liquid extraction and purification by column chromatography. This step yielded methyl 3-(N'-hydroxycarbamimidoyl)benzoate with a yield of 93%.

Synthesis of *methyl 3-(N'-((2-fluorobenzoyl)oxy)carbamimidoyl)benzoate*

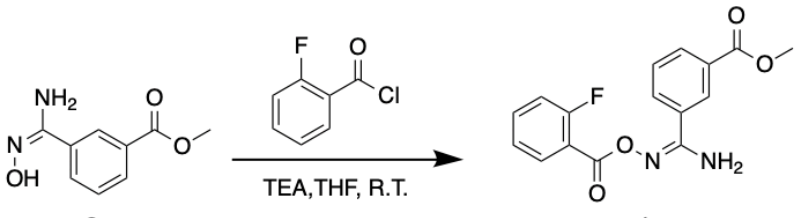

The obtained methyl 3-(N'-hydroxycarbamimidoyl)benzoate (1.06 g, 5.46 mmol) was dissolved in anhydrous tetrahydrofuran (THF). Once fully dissolved, triethylamine (TEA, 1.52 mL, 10.92 mmol) was added, and the mixture was stirred for 20 minutes at room temperature. Subsequently, 2-fluorobenzoyl chloride (0.97 mL, 8.19 mmol) was added, and the reaction continued for 1 hour. TLC (2:1 petroleum ether/ethyl acetate) confirmed product formation. The mixture was filtered to remove salts, which were washed with THF to maximize product recovery. The solution was evaporated under vacuum, yielding methyl 3-(N'-((2-fluorobenzoyl)oxy)carbamimidoyl)benzoate with a 79% yield after standard workup.

Synthesis of *methyl 3-(5-(2-fluorophenyl)-1,2,4-oxadiazol-3-yl)benzoate*

Next, methyl 3-(N'-((2-fluorobenzoyl)oxy)carbamimidoyl)benzoate (1.36 g, 4.3 mmol) was dissolved in toluene and heated under reflux for 1 hour. TLC confirmed the formation of the desired product, which was purified by column chromatography using a 5:1 ratio of petroleum ether to ethyl acetate. This step yielded 83%.

Synthesis of ***PTC124***

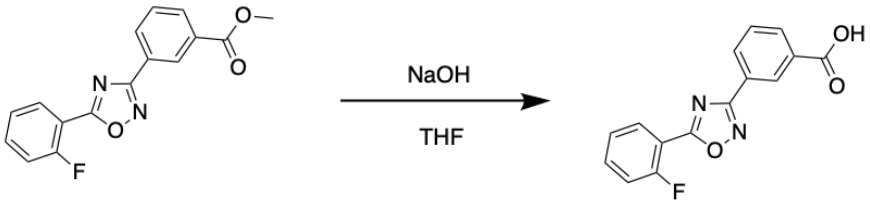

Finally, the purified product (1.06 g, 3.56 mmol) was dissolved in THF, and an aqueous solution of sodium hydroxide (1.5 M) was added in a 4:1 ratio (THF
solution). The reaction was stirred overnight at room temperature. After completion, confirmed by TLC, the solvent was evaporated under vacuum, and water was added to the residue. The pH was adjusted to 1 using hydrochloric acid (HCl), leading to product precipitation. The crude Ataluren was recovered by vacuum filtration and recrystallized from ethanol, yielding pure Ataluren with a final yield of 60%. The overall yield for the process was 34%.

PTC124: Reaction yield 34%, MP 241-242 °C. ^{1}H NMR (DMSO-d6) δ (ppm): 8.16 (d, 2H), 7.80 – 7.71 (m, 1H), 7.66 (t, 2H), 4.45 (q, 2H), 1.36 (t, 3H). HRMS for $C_{15}H_9FN_2O_3$ found 285.0682 $[M + H]^+$ (Calcd. 285.067) and 307.0501 $[M+Na]^+$ (Calcd. 307.0489).

Synthesis of ***IP30***

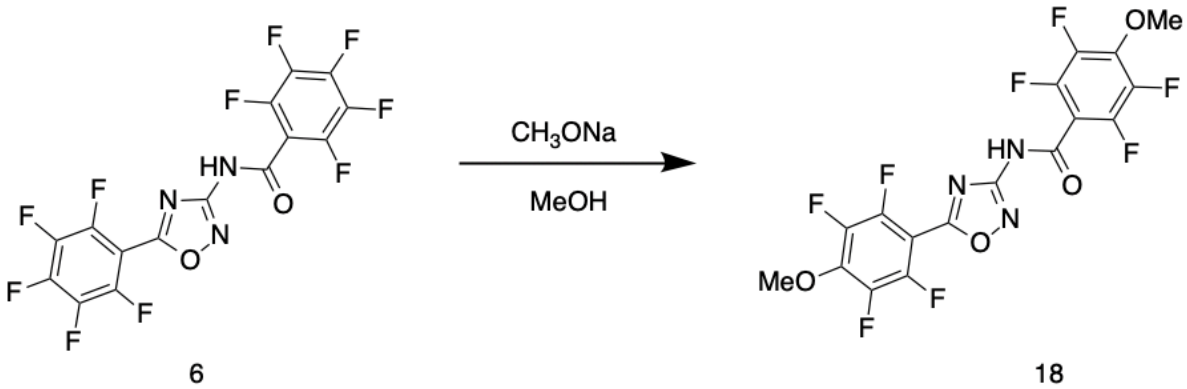

6 18

The reaction is started by adding NV914 (0.1 g, 0.22 mmol) and sodium methoxide (0.024g, 0.44 mmol) in methanol. The reaction is left under stirring at room temperature overnight. After about

24 hours the reaction is checked by TLC. The solvent was removed by vacuum, and the crude product was subjected to liquid-liquid extraction. The aqueous phase was extracted three times with ethyl acetate (3 x 100 mL). The organic phase was dried over anhydrous sodium sulfate (Na_2SO_4), filtered, and the solvent was removed under vacuum. The crude product was purified by flash chromatography using a petroleum ether/ethyl acetate gradient, starting at a 10:1 ratio and gradually shifting to 5:1.

IP30: Reaction yield 22%, MP 203-204 °C. ^{1}H NMR (DMSO-d6) δ (ppm): 12.72 (s, 1H), 4.23 (t, 3H), 4.15 (t, 1H). HRMS for $C_{17}H_7F_8N_3O_4$ found 470.0394 $[M + H]^+$ (Calcd. 470.0382) and 492.0204 $[M+Na]^+$ (Calcd. 492.0201).

Synthesis of ***IP31***

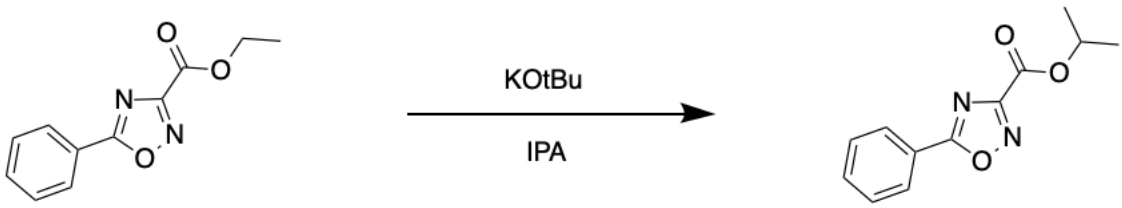

The reaction is started by adding NV930 (0.1 g, 0.49 mmol) and potassium tert-butoxide (0.03 g, 0.22 mmol) in propan-2-ol (20 mL). The reaction is left under stirring at room temperature overnight. After about 24 hours the reaction is checked by TLC. The solvent was removed by vacuum, and the crude product was subjected to liquid-liquid extraction. The aqueous phase was extracted three times with ethyl acetate (3 x 100 mL). The organic phase was dried over anhydrous sodium sulfate (Na_2SO_4), filtered, and the solvent was removed under vacuum. The crude product was purified by flash chromatography using a petroleum ether/ethyl acetate gradient, starting at a 2:1 ratio and eventually to 1:1.

IP31: Reaction yield 30%, MP 50 - 51 °C. ^{1}H NMR (DMSO-d6) δ (ppm): 8.20 – 8.11 (m, 2H), 7.79 – 7.71 (m, 1H), 7.70 – 7.60 (m, 2H), 5.26 (p, 1H), 1.37 (d, 6H). HRMS for $C_{12}H_{12}N_2O_3$ found 233.0935 $[M + H]^+$ (Calcd. 233.0921) and 255.0723 $[M+Na]^+$ (Calcd. 255.074).

Synthesis of ***IP32***

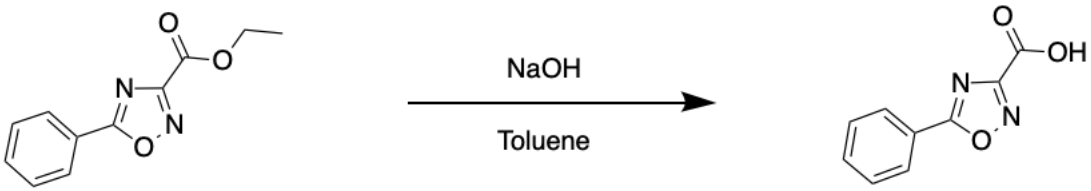

The reaction is started by adding NV930 (0.1 g, 0.49 mmol) and sodium hydroxide (0.02 g, 0.49 mmol) into a flask with toluene (15 mL). The reaction is left under stirring at room temperature overnight. After about 24 hours the reaction is checked by TLC. The solvent is dried out by vacuum and water is added to the residue. After adding water, the pH is adjusted to 1 by adding acidic solution of HCl 1M and the product starts precipitating out of the water. The clean product is then recovered by vacuum filtration.

IP32: Reaction yield 83%, MP 109 - 110 °C. HRMS for $C_9H_6N_2O_3$ found 191.0429 $[M + H]^+$ (Calcd. 191.0451)

***In vitro* metabolism.** To assess the metabolism of two compounds, NV914 and NV930, separate *in vitro* experiments were carried out using pooled HLMs from 50 donors (both male and female) provided by Gibco™, Thermo Fisher Scientific, U.S. The experimental setup was consistent for both compounds, except for their concentrations: NV914 was tested at 2 mM, while NV930 was tested at 100 mM.

In both cases, the microsomes were prepared at a concentration of 20 mg protein/mL, and incubations were carried out at 37°C in a total volume of 0.2 mL. NADPH was included in all reactions as a necessary cofactor for cytochrome P450 enzyme activity.

To further explore the glucuronidation potential of NV914, UDP-glucuronyltransferase (UGT) activity was measured by adding magnesium chloride (1 mM), alamethicin (50 µg per mg of microsomal protein), and uridine diphosphate glucuronic acid (UDPGA, 5 mM) to the incubation mixtures. The buffer volumes were carefully adjusted to ensure that all samples maintained a consistent final volume for reliable comparison.

The experimental setup began with the preparation of a stock solution of the compound in Acetonitrile, ensuring complete dissolution. Subsequently, HLMs were thawed gradually on ice to maintain their enzymatic activity. Then the microsomes, test molecule and the buffer were pre-incubated in a water bath at 37°C for five minutes. This step allowed to acclimate to the reaction conditions, optimizing enzyme function. The reactions were initiated by adding the necessary cofactors and allowed to proceed for different time intervals: at the start of the reaction (T_0), after

5 minutes (T_5), 15 minutes (T_{15}), 30 minutes (T_{30}), and 60 minutes (T_{60}). At each time point, each aliquot was promptly quenched by adding it to Acetonitrile, stopping further enzymatic activity. After collection, the samples were vortexed to mix thoroughly and then centrifuged at approximately 3000 rpm for 5 minutes to separate the supernatant from the protein pellet. The resulting supernatant, containing the metabolized NV914, was stored for subsequent High-Performance Liquid Chromatography- Mass Spectrometry (HPLC-MS) analysis.

Cell lines. In this study, several cell lines were employed to investigate mutations associated with DMD and LRBA gene mutations. The first cell line, derived from the c.5758 C>T substitution (p.Gln1920X), was available at the Institute for Bioengineering of Catalonia (IBEC). Additionally, two other cell lines, c.3556 G>T substitution (p.Glu1186X) and c.8713 C>T substitution (p.Arg2905X) were provided by Professor Vincent Mouly from the Institute of Myology in France. Each of these cell lines presents a distinct type of premature stop codon. Furthermore, the study included cell lines related to LRBA gene mutations, specifically the $LRBA^{R1683X/R1683X}$ cell line, characterized by a nonsense mutation, as well as a heterozygous line derived from the sibling of an affected individual. All human samples were collected and analyzed according to the standards of the ethical committee and the Declaration of Helsinki, following written consent was obtained. The patient gave written informed consent for skin biopsy, fibroblast culture, inclusion in the trial and analysis on the explant liver. These cell lines served as essential models for proteomic analysis and the evaluation of therapeutic strategies aimed at addressing the underlying genetic defects in these conditions.

Toxicity assay. Cells were seeded in coated 96-well plates at an average density of 10,000 cells per well. After reaching confluency, which typically occurred within 48 hours, the growth medium (GM) was replaced with differentiation medium (DM). The DM was refreshed every two days. Following seven days of differentiation, the DM was replaced with fresh DM containing the test drugs. After 48 hours of treatment, the MTS assay was performed to assess cell viability.

In-Cell Western. Cells were seeded in black-coated 96-well plates at a density of 10,000 cells per well. Upon reaching confluency, the GM was replaced with DM, which was renewed every two days. In the experimental condition, treatment with PTC124 and NV compounds was initiated immediately after the switch to DM. After nine days of differentiation, the cells were fixed. Control treatments included solvent controls: water for NV848 and DMSO for NV914, NV930, and PTC124, at a final concentration of 0.1%.

Permeabilization was then performed using PBS-T (PBS with 0.1% Triton X-100) to allow access of antibodies to intracellular proteins. A blocking buffer was applied to reduce non-specific antibody binding. For dystrophin detection, primary antibodies Mandys1 and Mandys106 were used. After incubation with the primary antibodies, cells were treated with anti-mouse IRDye 800CW secondary antibodies for visualization. To ensure accurate quantification of protein levels, CellTag™ 700 Stain was employed for normalization to cell number. Plates were then scanned using an appropriate fluorescence imager to quantify dystrophin expression levels. Data analysis was conducted using Image Studio™ Software. Intensity measurements in the 800-nm channel were corrected by subtracting the average background intensity, determined from rows without primary antibody. The corrected values were then normalized by dividing by the corresponding intensity in the 700-nm channel, ensuring accurate data reflecting specific protein expression relative to cell number.

Animal models. The animal experiments were performed on C57BL/6 mice and $CFTR^{G542X/G542X}$ homozygous mice (generated by crossing heterozygous $CFTR^{WT/G542X}$ mice). C57BL/6 mice were sourced from ENVIGO Srl (San Pietro al Natisone, Italy), and $CFTR^{G542X/G542X}$ homozygous mice were generously provided by Prof. C. Hodges (Case Western Reserve University, Cleveland, USA). All mice were housed in a controlled environment (temperature 22–25°C, humidity 50–60%) under a 12-hour light/dark cycle. Animal care and experimental protocols adhered to Italian law (D.Lgs 26/2014) and were approved by the University of Palermo's Animal Care and Use Ethics Committee and the Italian Ministry of Health (Authorizations n.1235/2020 and n. 2/2022-PR), following EU Directive 2010/63/EU.

Biodistribution Studies. The biodistribution studies aimed to assess the tissue distribution of three compounds, NV848, NV914, and NV930, following oral administration in mice. The experimental design consisted of three treated groups, each receiving a different investigational compound, and a fourth, untreated group that served as a negative control. Specifically, Group 1 received NV848, Group 2 was administered NV914, and Group 3 was given NV930. A total of 81 C57BL/6 male mice (4 weeks old, average weight 18.0 ± 4.0 g) were utilized: 20 mice for NV848, 35 mice for NV914, 20 mice for NV930 and 6 mice for the control group.

The preparation of the novel compounds was decided according to their solubility profiles, which significantly influenced the formulation strategy. NV848, a hydrophilic molecule, was dissolved in water to achieve a final volume of 250 µL, ensuring optimal bioavailability. On the other hand,

both NV914 and NV930, which exhibited lipophilic characteristics, were prepared in initial stock solutions of dimethyl sulfoxide (DMSO) before dilution in olive oil to a final volume of 250 µL. A standardized dosing regimen of 60 mg/kg was chosen for all compounds, a dosage based on previous studies on Ataluren, which indicated therapeutic potential at comparable dosing levels. Post-administration, mice were sacrificed using cervical dislocation at predetermined time points. For NV848 and NV930, mice were sacrificed at four different time points (n=5 per time point): 45 minutes, 2 hours, 4 hours, and 24 hours. In comparison, NV914 included additional sampling time points to allow for a more detailed pharmacokinetic profile. Specifically, for NV914, mice were sacrificed at seven time points (n=5 per time point): 45 minutes, 1 hour, 2 hours, 3 hours, 4 hours, 6 hours, and 24 hours.

Sample preparation for HPLC-MS analyses. The preparation of tissue samples for HPLC-MS analysis was carefully personalized for each compound, to ensure accurate quantification of the molecules in the biodistribution studies. Each step in the process was designed to minimize potential errors and maximize the reliability of the results.

Blood samples were collected using syringes treated with EDTA (0.5 M, pH 8.0) to prevent coagulation, followed by centrifugation at 3000 rpm for 10 minutes to facilitate the separation of plasma from cellular components. Both plasma and cellular fractions were preserved for subsequent analyses. Additionally, a collection of organs was harvested, washed thoroughly in sterile 0.9% sodium chloride solution, and cryopreserved in liquid nitrogen before storage at -80°C until further processing. The extraction of compounds from tissue samples involved homogenization, using the Omni TH Tissue Homogenizer (Kennesaw GA, USA), in a 10 mL tube containing 200 µL of 0.9% followed by the addition of 600 µL of ice-cold acetonitrile (ACN, CHROMASOLV™ LC-MS, Honeywell, U.S.) to facilitate protein precipitation.

After thorough vortexing, samples were centrifuged at 14,000 rpm at 4°C to separate the supernatant, which was subsequently lyophilized at -100°C under vacuum (CoolSafe, SCANVAC, Labogene, Allerød, Denmark) and stored at -20°C until analytical evaluation. For analysis, lyophilized samples were reconstituted with 100 µL of a 3:1 acetonitrile-to-water mixture (CHROMASOLV™ LC-MS, Honeywell, U.S.) for NV848. The samples were vortexed for 5 minutes and then centrifuged at 14,000 rpm for 10 minutes to obtain the supernatant for injection into the HPLC-MS system (Agilent 1250 Infinity HPLC, Agilent Technologies 6540 UHD accurate mass Q-TOF LC/MS).

The preparation of NV914 followed a similar process, with a critical addition of an internal standard during reconstitution. After homogenization and protein precipitation steps similar to

those for NV848, lyophilized residues were reconstituted in 100 µL of acetonitrile containing the internal standard, improving accuracy by accounting for potential matrix effects. The samples were vortexed, centrifuged, and 1 µL of the supernatant was injected for HPLC-MS analysis.
The approach for NV930 was nearly identical to that for NV914, reinforcing the consistency of the preparation process across the different compounds. Following homogenization, precipitation, freeze-drying, and reconstitution, the samples were vortexed, centrifuged, and 5 µL of the supernatant was injected into the HPLC-MS system.
To validate extraction efficiency, recovery tests were performed for both plasma and individual organs. Standard solutions of each NV compound were spiked into blank tissues, with extractions conducted and recovery rates calculated by comparing concentrations of pre- and post-extraction spiked samples. This comparison accounted for matrix effects on extraction efficiency.

Proteomic analysis of fibroblast cell lines. Fibroblast LRBA$^{R1683X/R1683X}$ cell lines, along with a heterozygous line, were cultured and treated under five different conditions: untreated, and treated with NV848, NV914, NV930, and Ataluren. Initially, cells were seeded at a density of 250,000 cells per 60 mm plate and allowed to adhere for 24 hours, with each condition prepared in six replicates. Following this incubation, the medium was replaced with either a solvent control (DMSO) or one of the compounds at half the IC50 concentration, achieving a final concentration of 12 µM. Cells were then incubated with the treatments for 72 hours. After this period, plates were transferred to ice, and the medium was removed. Each plate was washed twice with 1 mL of PBS to eliminate residual media and treatment compounds.
After completely removing the PBS, cells were lysed by adding 80 µL of SDC buffer. The cells were scraped into labeled Eppendorf tubes, and an additional 50 µL of SDC buffer was added to ensure full collection, bringing the final lysate volume to 130 µL per sample. The lysates were heated at 95°C for 5 minutes at 1400 rpm to facilitate complete cell lysis.
Following this initial lysis step, a sample preparation protocol was performed to ensure optimal conditions for downstream analyses. The lysates were subjected to a BCA assay to determine protein concentration, which is crucial for normalizing the subsequent steps. Each sample was diluted to achieve a total of 200 µg of protein in 270 µL of lysis buffer, allowing for accurate comparison of protein levels across samples.
For further processing, reduction and alkylation steps were performed using a reduction/alkylation buffer (TCEP 100 mM and 2-CAM 400 mM). A volume of 1:10 of this buffer was added to the samples, which were then incubated in the dark at 45°C for 5 minutes while being gently mixed at 1400 rpm. This step ensures the reduction of disulfide bonds and alkylation

of cysteine residues, which is essential for effective enzyme digestion. Following this, the samples were allowed to cool to room temperature before enzymatic digestion began. One vial of trypsin/Lys-C was reconstituted in 20 µL of trypsin buffer, and the enzyme was added to the samples at an enzyme-to-substrate ratio of 1:100, resulting in 2 µg of enzyme for 200 µg of protein. This mixture was then digested overnight at 37°C with continuous mixing at 1400 rpm, allowing for comprehensive peptide generation.

After digestion, the resulting peptides were prepared for analysis using SDB-RPS StageTips. Initially, 100 µL of SDB-RPS loading buffer (99% v/v Isopropanol; 1% v/v Trifluoroacetic acid) was added to the nearly dried samples to facilitate resuspension. The samples were then transferred to the top of the StageTips, which were placed in centrifuge adapters within waste Eppendorf tubes for further processing. The StageTips were centrifuged to dryness at 1500g for 8 minutes at room temperature to ensure that the peptides adhered properly to the sorbent.

To clean the samples, 100 µL of SDB-RPS wash buffer 1 (99% v/v Isopropanol; 1% v/v Trifluoroacetic acid) was added to each StageTip, and the centrifugation step was repeated. Next, 100 µL of SDB-RPS wash buffer 2 (94.8% v/v Water; 5% v/v Acetonitrile; 0.2% v/v Trifluoroacetic acid) was used for a second wash to remove any residual contaminants and non-specific peptides.

Following this, phosphopeptides were eluted from the StageTips. The tips were placed in new Eppendorf tubes containing glass inserts, and 60 µL of SDB-RPS elution buffer (83.33% v/v Ammonium hydroxide; 10% v/v Acetonitrile; 6.67% v/v Water) was added to each StageTip. Following centrifugation to dryness at 1500g for 5 minutes, the samples were dried in a SpeedVac at 45°C for approximately 30 to 40 minutes to remove any residual solvents.

For reconstitution, the glass vial inlet containing the dried samples was removed, and 400 µL of water was added to the empty 2 mL storage tube. The inlet was then reinserted into the tube, and 5 µL of peptide standard mix and 40 µL of loading eluent were added to reconstitute the samples. The samples were ultrasonicated for 5 minutes to help break down any aggregates, ensuring the peptides were fully dissolved. Following this, the samples were centrifuged at 5000g for 7 minutes, and the glass vial inlet was transferred into a glass vial for subsequent analysis.

NanoLC-MS/MS analysis for peptide identification and quantification. The samples were analyzed by nLC-MS/MS using a Dionex Ultimate3000 nano-LC (Thermo Fisher Scientific, Bremen, Germany) coupled to a timsTOF pro mass spectrometer (Bruker Daltonics, Bremen,Germany). Peptides were identified and quantified based on their fragmentation patterns in the mass spectrometer. Data analysis was conducted using MaxQuant software, employing the

Label-Free Quantification (LFQ) method to determine relative protein abundances across samples. The LFQ approach enabled the comparison of protein expression levels without the need for isotope labels. The graphical representations have been done using Perseus software.

Quantification of NV compounds via HPLC-MS. Various methodologies were employed to ensure accurate quantification and to address potential matrix effects in the analysis of NV molecules across multiple experimental conditions.

For the *in vitro* experiments with HLMs, calibration standards were prepared in acetonitrile to quantify NV914 and NV930. NV914 standards ranged from 0.1 to 1.5 µM (0.1, 0.5, 1, 1.5 µM), and linear regression was applied using the unweighted least squares method. For NV930, a second calibration was required in a higher concentration range (5, 25, 50, 100 µM). Homoscedasticity was confirmed, and a new calibration curve using the same matrix was created with heat-deactivated microsomes to correct for matrix effects, revealing some signal suppression. Calibration was performed in triplicate, and sample analyses in duplicate, with recovery rates calculated to account for extraction losses.

For NV848, a matrix-matching technique was used to evaluate and correct for any matrix effects that may influence the results. Calibration standards for NV848 were prepared by mixing 50 µL of NV848 at concentrations ranging from 0.1 to 50 µg/mL with 50 µL of a blank matrix, yielding final concentrations between 0.05 and 25 µg/mL. A linear regression analysis was conducted using the least squares method on these calibration standards to generate a calibration curve for the quantification of NV848.

In contrast, for NV914, the coeluting internal standard method was implemented to assess matrix effects effectively. Calibration standards for NV914 were prepared by mixing 50 µL of a 1 µg/mL solution of IP30 with 50 µL of NV914 solutions at varying concentrations: 0.2, 0.6, 1, 1.4, 2 µg/mL. This mixture was brought to a final volume of 100 µL, maintaining a consistent internal standard concentration of 0.5 µg/mL across all solutions. Consequently, the final concentrations of NV930 were established at 0.1, 0.3, 0.5, 0.7, 1 µg/mL in acetonitrile.

The calibration curve for NV914 was constructed by plotting the ratio of the peak area of NV914 to the peak area of the internal standard against the concentration of NV914.

For NV930, a similar internal standard method was utilized, employing a coeluting internal standard specific to NV930. Calibration standards for NV930 were prepared by mixing 50 µL of a 10 µg/mL solution of IP31 with 50 µL of NV930 solutions at varying concentrations: 1.8, 5.4, 16.4, 48, 148, 444, and 1332 ng/mL. This mixture was brought to a final volume of 100 µL, maintaining a consistent internal standard concentration of 5 µg/mL across all solutions.

Consequently, the final concentrations of NV930 were established at 0.9, 2.7, 8.2, 24, 74, 222, and 666 ng/mL in acetonitrile.

Fabrication of PDMS casting molds. To fabricate the Polydimethylsiloxane (PDMS) casting molds, the polymeric base and curing agent (SYLGARD® 184**)** were mixed at a weight ratio of 10:1 for 5 minutes. The mixture was then placed in a vacuum desiccator to eliminate air bubbles. Next, the uncured PDMS mixture was poured onto the negative mold. To ensure complete filling of the pillar holes, air was removed using a syringe equipped with a dispensing tip, followed by another round of vacuum desiccation to remove any remaining bubbles. Once prepared, the negative mold was covered with a glass slide to facilitate even curing. Finally, the PDMS was cured overnight at 65 °C in a Petri dish.

Encapsulation. PDMS casting molds were sterilized using UV light in a biosafety cabinet for 15 minutes. These molds were then filled with 50 µL of a filtered 1% w/v Pluronic solution in cold PBS and stored at 4ºC for 2 hours. Prior to use, excess Pluronic was carefully removed with autoclaved filter paper, ensuring the molds remained cold until the encapsulation step.
For cell encapsulation, approximately 50 µL of the final solution was needed per sample. This final solution was prepared by combining fibrinogen (8 mg/mL in D-PBS without calcium and magnesium) and a Matrigel mixture (60% Matrigel, 38.4% growth medium, and 1.6% thrombin) in a 1:1 ratio. The fibrinogen solution was prepared by incubating it at 37ºC to dissolve, after which it was kept on ice. Cells were treated with trypsin, counted, and spun down according to the cell line protocol, with the cell suspension prepared at a concentration of 2.5×10^7 cells/mL. The suspension was transferred into an Eppendorf tube, where Matrigel is added first, followed by thrombin, and the mixture was carefully combined to avoid bubble formation. Once the fibrinogen and Matrigel solutions were ready, 35 µL of each were mixed to fill two wells with 30 µL of the final solution per well, ensuring that polymerization did not occur before the solution was applied to the casting mold. Samples were incubated for 30 minutes at 37ºC to allow polymerization. For media preparation, ACA was dissolved at a concentration of 1 mg/mL in either GM or DM, and the solution was filtered. Each sample, plated in a 48-well plate, received 1 mL of GM supplemented with ACA. After two days, the GM was completely replaced with DM, and half of the DM was renewed every two days.

Cryosectioning. Samples were fixed in a 10% formalin solution for 30 minutes at room temperature and washed three times with PBS. They were then placed in a 30% sucrose solution

in PBS for 48 hours at 4ºC. Following this, the samples were embedded in optimal cutting temperature compound (PolyFreeze, Sigma-Aldrich) and frozen using isopentane chilled with liquid nitrogen. Using a cryostat, transverse sections of 20 µm thickness were obtained and mounted on SuperFrost Plus™ Adhesion slides. Prior to immunostaining, the slides were permeabilized with PBS-T and incubated in blocking buffer. The sections were then treated with primary antibodies overnight at 4ºC. After washing, they were incubated with fluorophore-conjugated secondary antibodies. Finally, DAPI was applied for nuclear staining.

Electrical Pulse Stimulation (EPS). After seven days of differentiation, human 3D skeletal muscle tissues were subjected to electrical stimulation to promote muscle contraction. This was achieved using a custom-built device comprising a 12-well plate fitted with two graphite electrodes per well located on the lid. The PDMS casting molds containing the muscle tissues were placed in the 12-well plate, which was then filled with fresh differentiation medium. The entire setup was maintained in a Zeiss Axio Observer Z1/7 equipped with an XL S1 cell incubator, set at 37 °C with 5% CO2 to provide optimal growth conditions. The system was connected to a pulse generator (Multifunction Generator WF1974, NF Corporation), allowing for the application of electrical square-wave pulses at a strength of 1 V/mm, with a pulse width of 1 ms. The frequency of the electrical pulses was varied between 1 and 50 Hz to assess muscle tissue responsiveness.

APPENDIX A

NV848

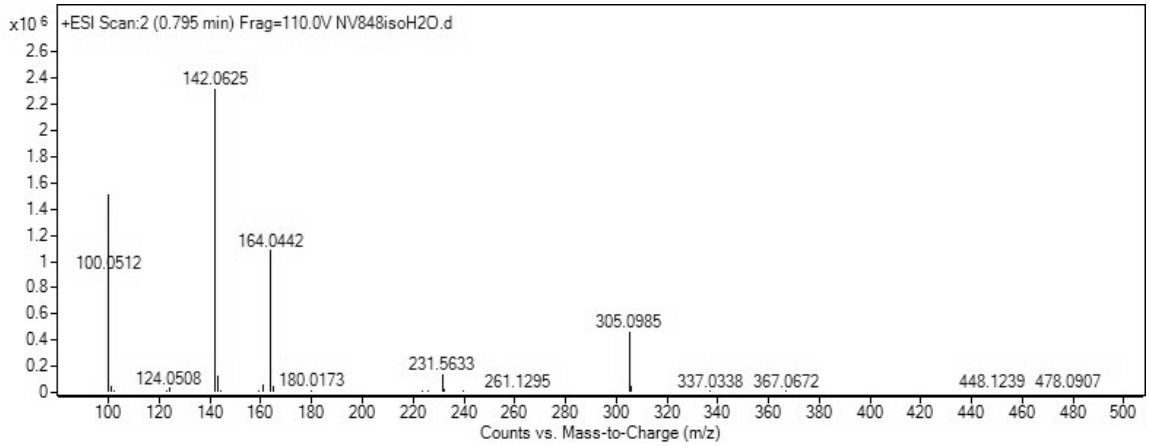

Figure 44. *Mass spectrum of compound (4). The molecular ion peak at m/z 142,0625 corresponds to* $[M+H]^+$ *for the formula* $C_5H_7N_3O_2$. *The molecular ion peak at m/z 164,0442 corresponds to* $[M+Na]^+$ *for the formula* $C_5H_7N_3O_2$.

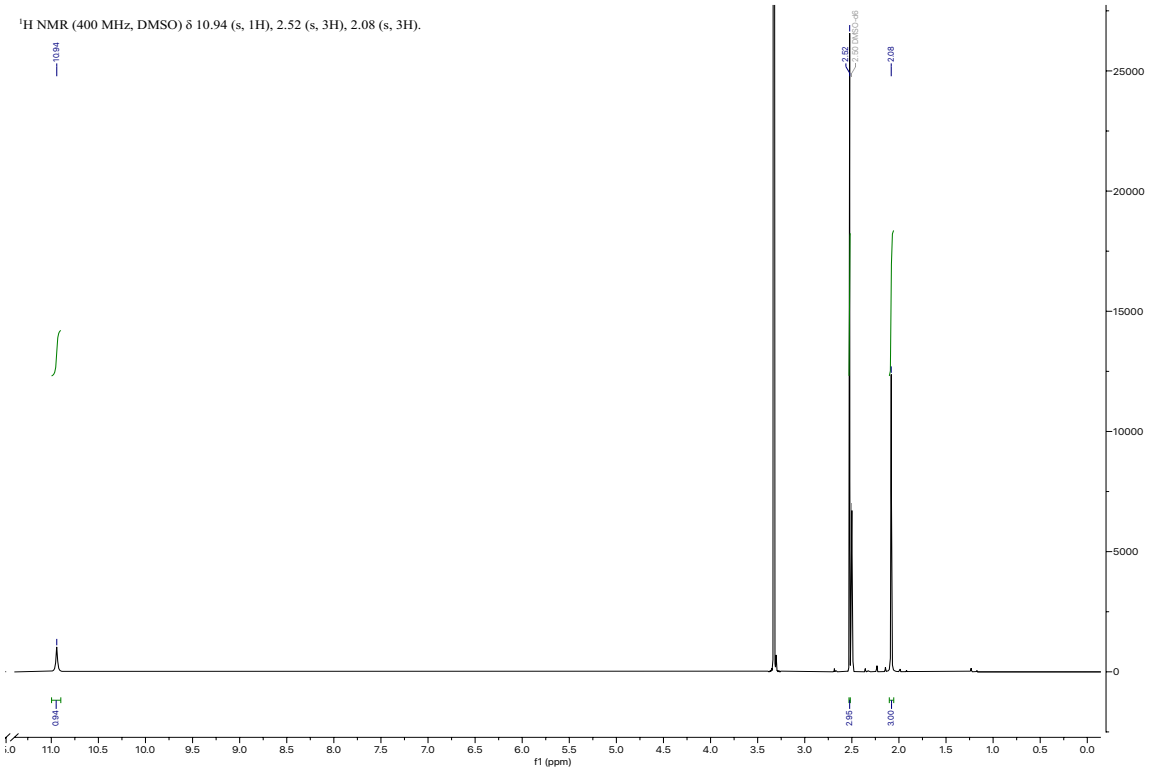

Figure 45. *¹H NMR spectrum in DMSO-d6 of compound (4) purified after column chromatography. δ (ppm): 2.08 (s, 3H), 2.52 (s, 3H), 10.94 (s, 1H).*

3-amino-5-perfluorophenyl-1,2,4-oxadiazole

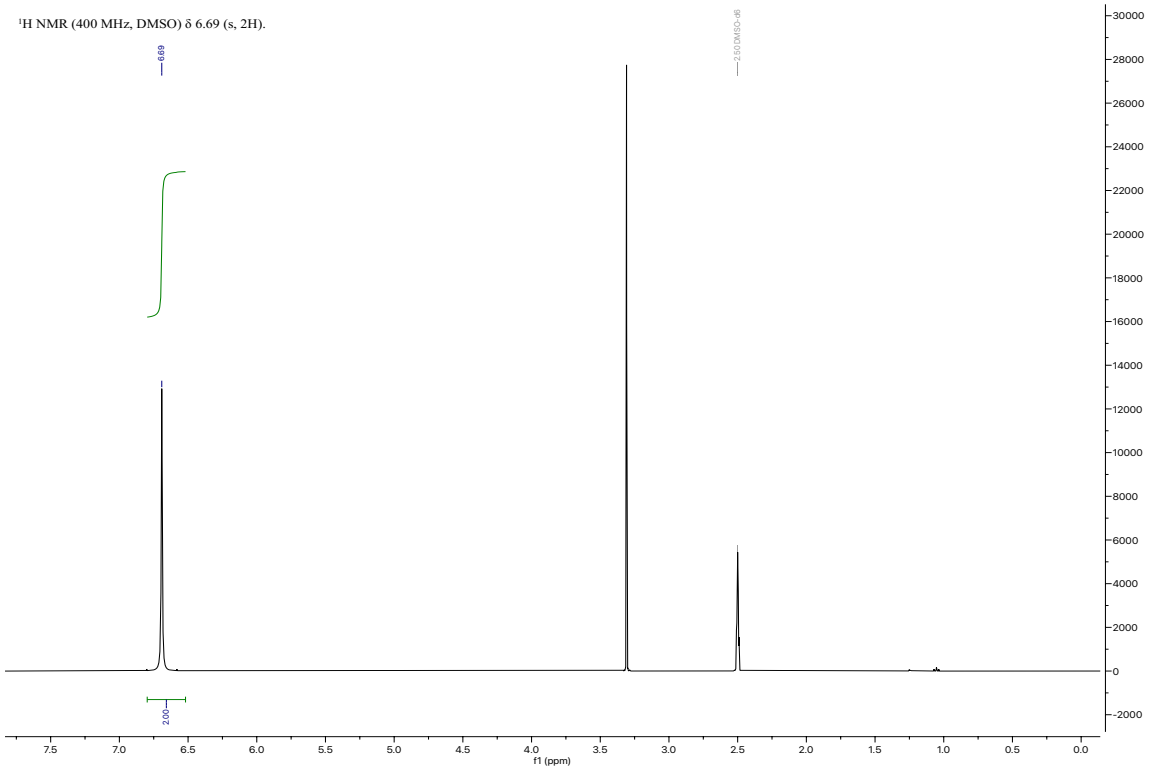

Figure 46. *¹H NMR spectrum in DMSO-d6 of compound (3) purified after column chromatography. δ (ppm): 6.69 (s, 2H).*

NV914

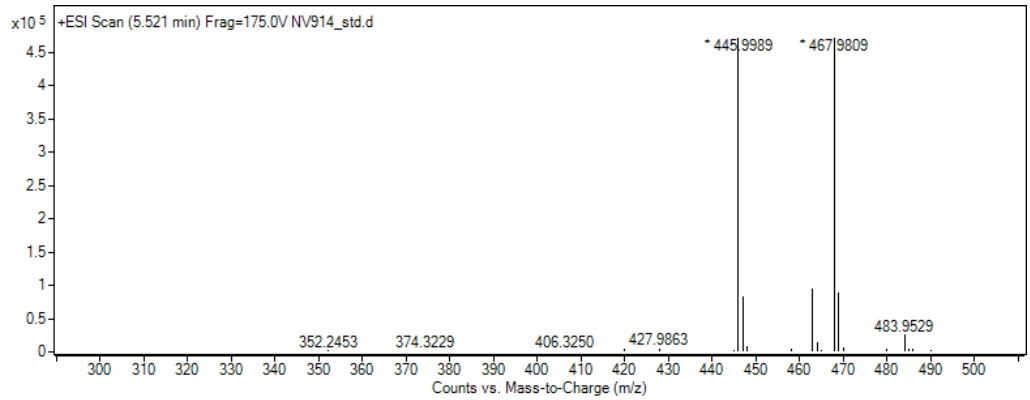

Figure 47. *Mass spectrum of compound (4). The molecular ion peak at m/z 445,9989 corresponds to $[M+H]^+$ for the formula $C_{15}HF_{10}N_3O_2$. The molecular ion peak at m/z 467,9809 corresponds to $[M+Na]^+$ for the formula $C_{15}HF_{10}N_3O_2$.*

NV930

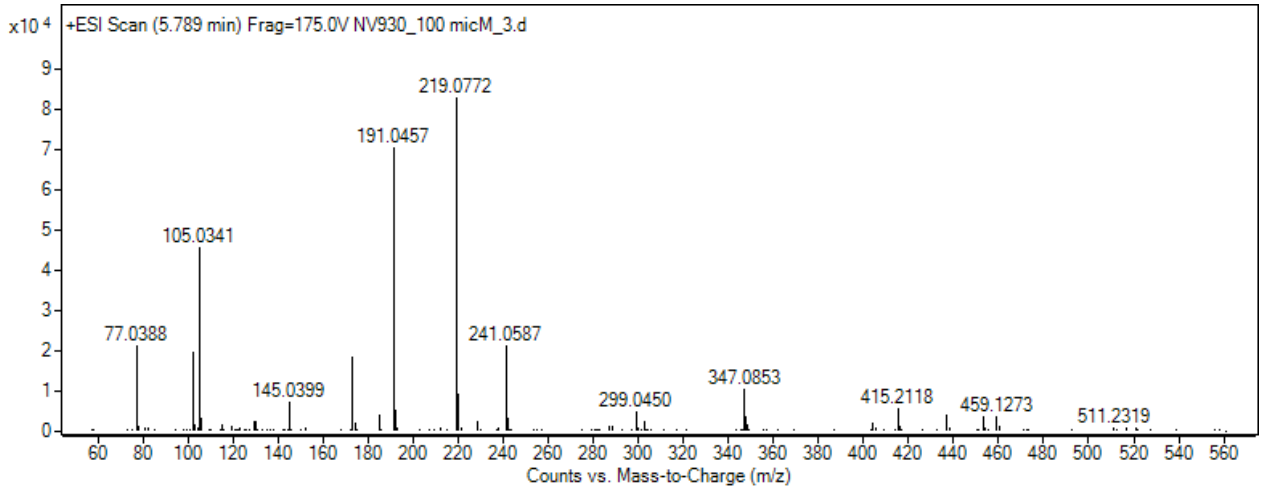

Figure 48. *Mass spectrum of compound (4). The molecular ion peak at m/z 445,9989 corresponds to* $[M+H]^+$ *for the formula* $C_{15}HF_{10}N_3O_2$. *The molecular ion peak at m/z 467,9809 corresponds to* $[M+Na]^+$ *for the formula* $C_{15}HF_{10}N_3O_2$.

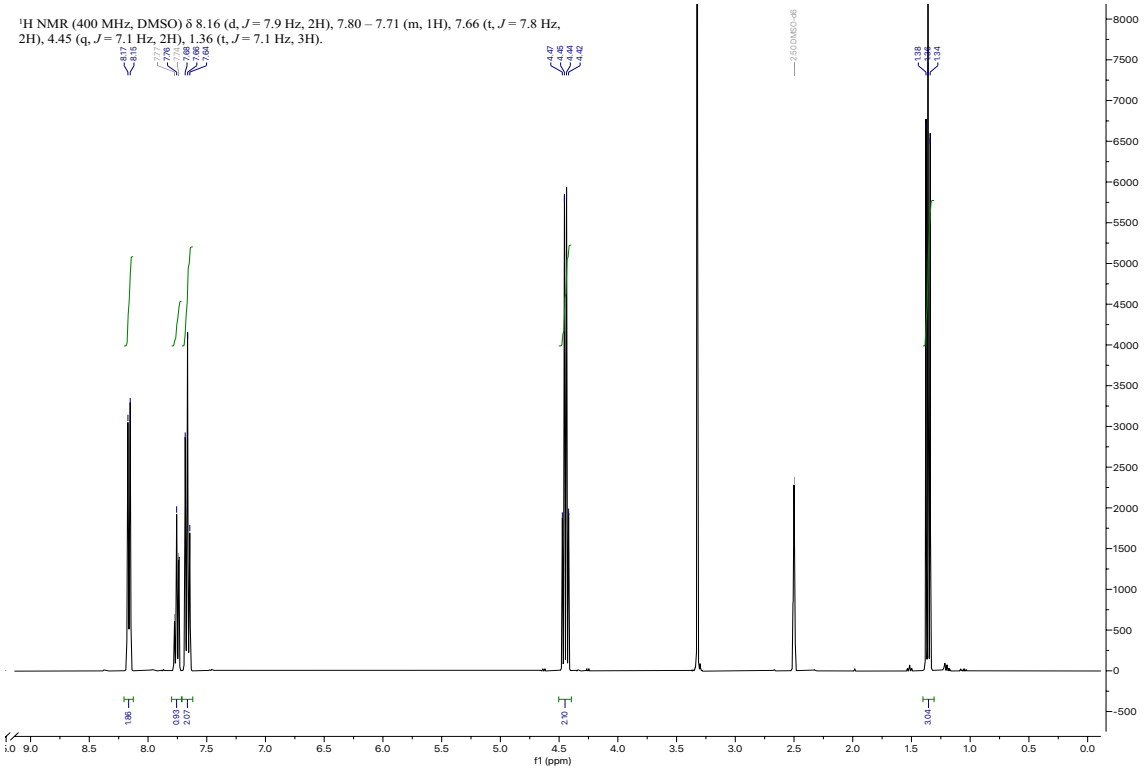

Figure 49. *¹H NMR spectrum in DMSO-d6 of compound (4) purified after column chromatography. δ (ppm): 8.16 (d, 2H), 7.80 – 7.71 (m, 1H), 7.66 (t, 2H), 4.45 (q, 2H), 1.36 (t, 3H).*

PTC124

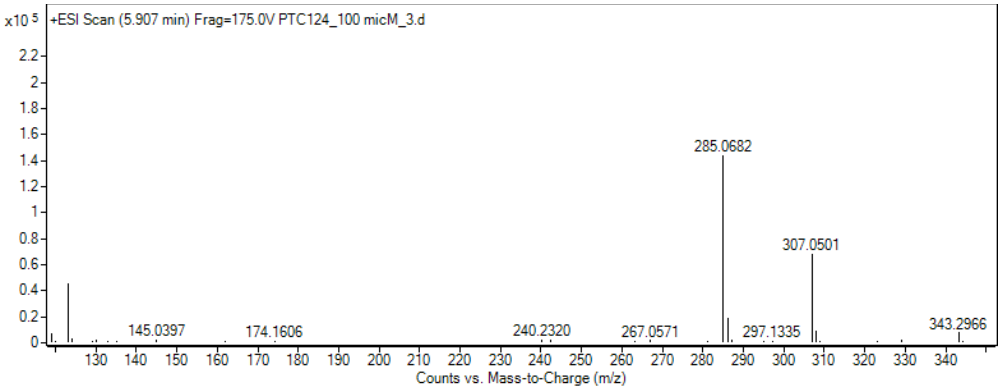

Figure 50. *Mass spectrum of compound (6). The molecular ion peak at m/z 285,0682 corresponds to* $[M+H]^+$ *for the formula* $C_{15}H_9FN_2O_3$. *The molecular ion peak at m/z 307,0501 corresponds to* $[M+Na]^+$ *for the formula* $C_{15}H_9FN_2O_3$.

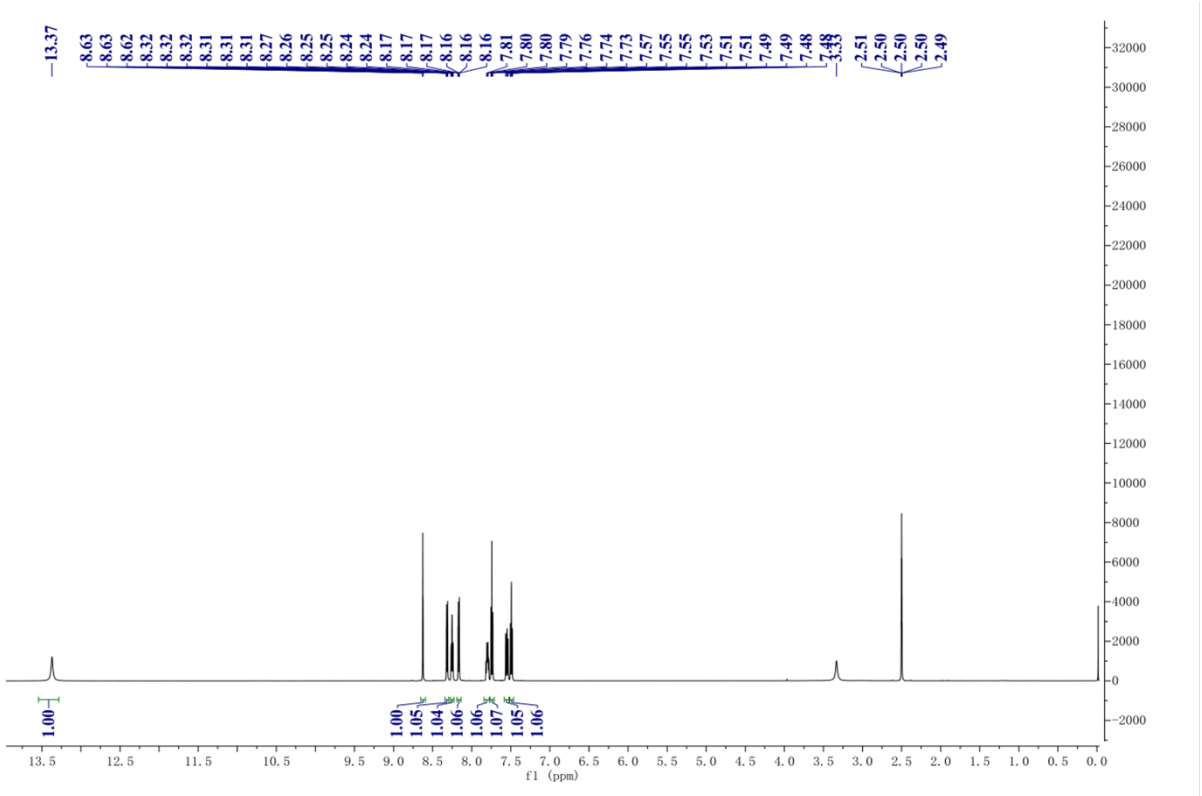

Figure 51. ^1H *NMR spectrum in DMSO-d6 of compound (6) purified after column chromatography. δ (ppm): 13.37(s, 1H), 8.63 (td, 1H), 8.39 – 8.31 (m, 1H), 8.18 (dt, 2H), 7.87 – 7.71 (m, 2H), 7.62 – 7.45 (m, 2H).*

IP30

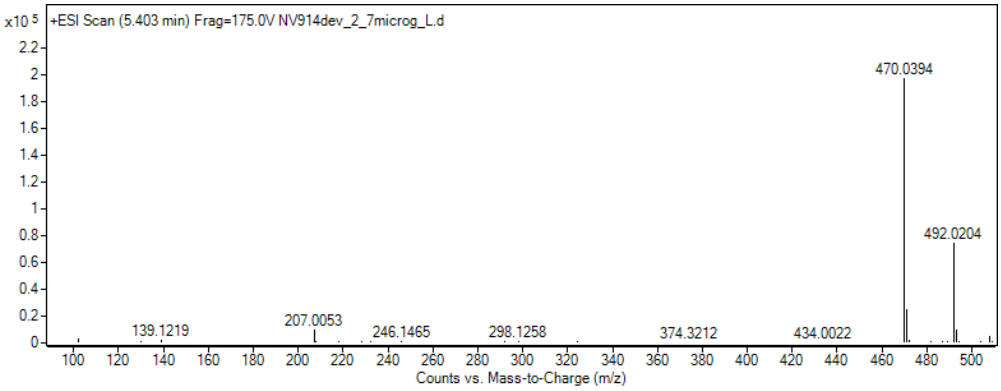

Figure 52. *Mass spectrum of compound (2). The molecular ion peak at m/z 470,0394 corresponds to* $[M+H]^+$ *for the formula* $C_{15}H_7F_8N_3O_4$. *The molecular ion peak at m/z 492,0204 corresponds to* $[M+Na]^+$ *for the formula* $C_{15}H_7F_8N_3O_4$.

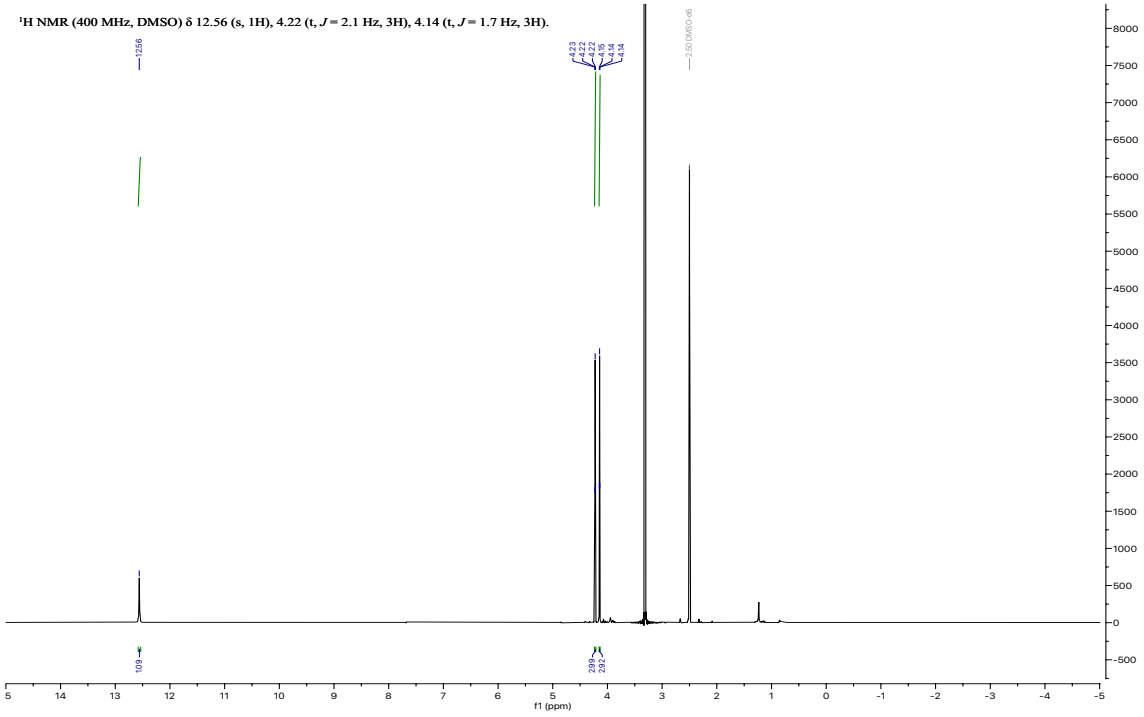

Figure 53. *^{1}H NMR spectrum in DMSO-d6 of compound (6) purified after column chromatography. δ (ppm): 12.72 (s, 1H), 4.23 (t, 3H), 4.15 (t, 1H).*

IP31

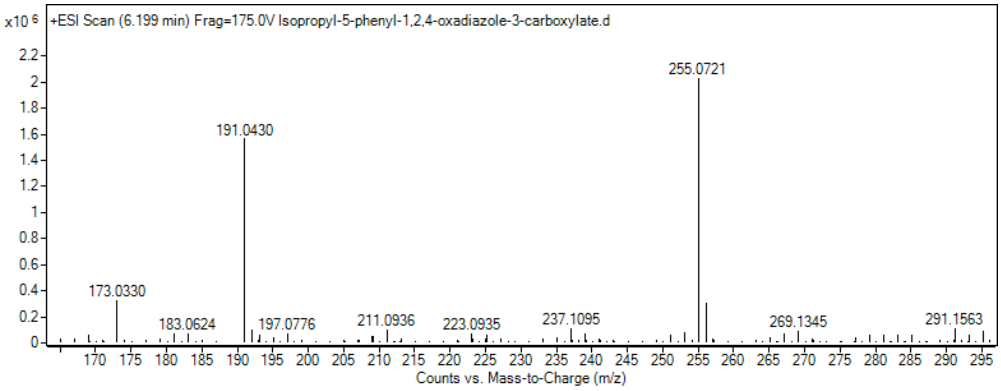

Figure 54. *Mass spectrum of compound (2). The molecular ion peak at m/z 233,0935 corresponds to* $[M+H]^+$ *for the formula* $C_{12}H_{12}N_2O_3$. *The molecular ion peak at m/z 255,0723 corresponds to* $[M+Na]^+$ *for the formula* $C_{12}H_{12}N_2O_3$.

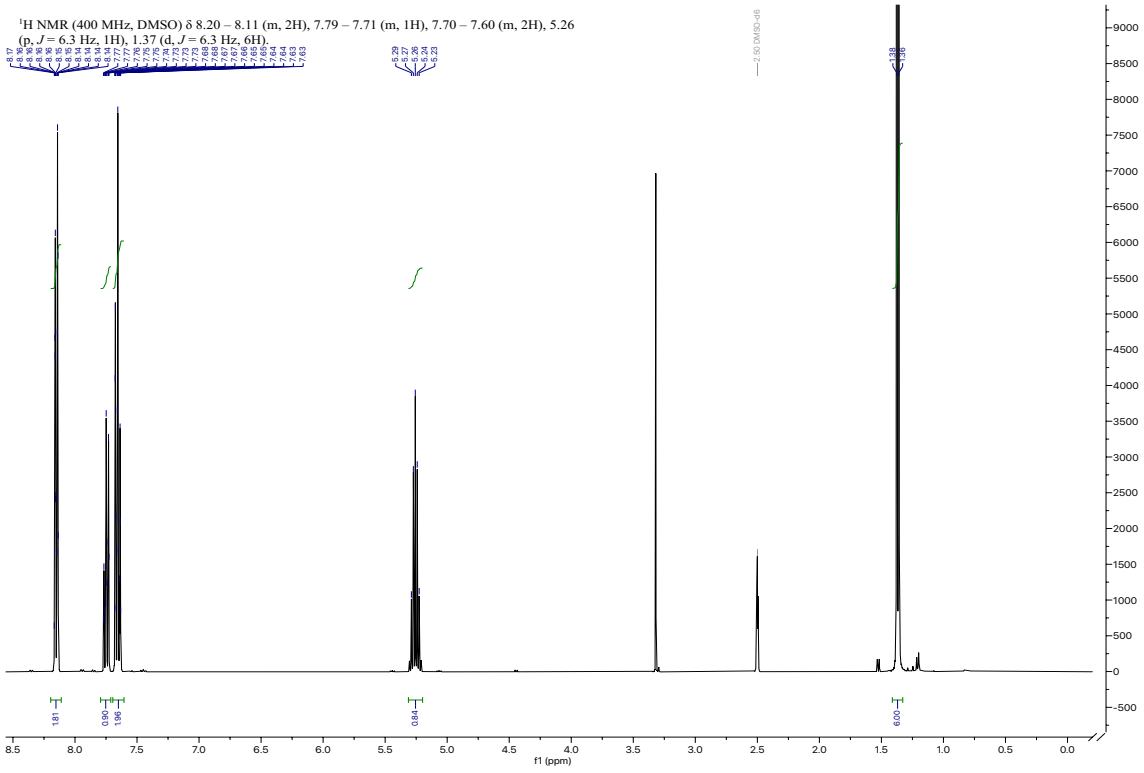

Figure 55. *¹H NMR spectrum in DMSO-d6 of compound (2) purified after column chromatography. δ (ppm): 8.20 – 8.11 (m, 2H), 7.79 – 7.71 (m, 1H), 7.70 – 7.60 (m, 2H), 5.26 (p, 1H), 1.37 (d, 6H).*

IP32

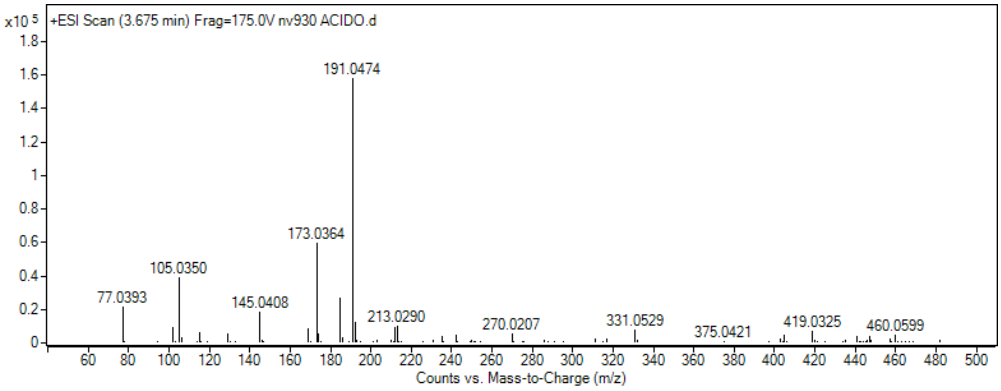

Figure 56. *Mass spectrum of compound (2). The molecular ion peak at m/z 191,0429 corresponds to* $[M+H]^+$ *for the formula* $C_9H_6N_2O_3$.

Bibliography

1. Ahn, A.H., Kunkel, L.M., 1993. The structural and functional diversity of dystrophin. Nat Genet 3, 283–291. https://doi.org/10.1038/ng0493-283
2. Alkalaeva, E.Z., Pisarev, A.V., Frolova, L.Y., Kisselev, L.L., Pestova, T.V., 2006. In vitro reconstitution of eukaryotic translation reveals cooperativity between release factors eRF1 and eRF3. Cell 125, 1125–1136. https://doi.org/10.1016/j.cell.2006.04.035
3. Baradaran-Heravi, A., Balgi, A.D., Hosseini-Farahabadi, S., Choi, K., Has, C., Roberge, M., 2021. Effect of small molecule eRF3 degraders on premature termination codon readthrough. Nucleic Acids Res 49, 3692–3708. https://doi.org/10.1093/nar/gkab194
4. Bar-Nun, S., Shneyour, Y., Beckmann, J.S., 1983. G-418, an elongation inhibitor of 80 S ribosomes. Biochim Biophys Acta 741, 123–127. https://doi.org/10.1016/0167-4781(83)90018-0
5. Bedwell, D.M., Kaenjak, A., Benos, D.J., Bebok, Z., Bubien, J.K., Hong, J., Tousson, A., Clancy, J.P., Sorscher, E.J., 1997. Suppression of a CFTR premature stop mutation in a bronchial epithelial cell line. Nat Med 3, 1280–1284. https://doi.org/10.1038/nm1197-1280
6. Bertram, G., Bell, H.A., Ritchie, D.W., Fullerton, G., Stansfield, I., 2000. Terminating eukaryote translation: domain 1 of release factor eRF1 functions in stop codon recognition. RNA 6, 1236–1247. https://doi.org/10.1017/s1355838200000777
7. Beryozkin, A., Nagel-Wolfum, K., Banin, E., Sharon, D., 2023. Factors Affecting Readthrough of Natural Versus Premature Termination Codons. Adv Exp Med Biol 1415, 149–155. https://doi.org/10.1007/978-3-031-27681-1_23
8. Bez Batti Angulski, A., Hosny, N., Cohen, H., Martin, A.A., Hahn, D., Bauer, J., Metzger, J.M., 2023. Duchenne muscular dystrophy: disease mechanism and therapeutic strategies. Front Physiol 14, 1183101. https://doi.org/10.3389/fphys.2023.1183101
9. Beznosková, P., Wagner, S., Jansen, M.E., von der Haar, T., Valášek, L.S., 2015. Translation initiation factor eIF3 promotes programmed stop codon readthrough. Nucleic Acids Res 43, 5099–5111. https://doi.org/10.1093/nar/gkv421
10. Bezzerri, V., Api, M., Allegri, M., Fabrizzi, B., Corey, S.J., Cipolli, M., 2020. Nonsense Suppression Therapy: New Hypothesis for the Treatment of Inherited Bone Marrow Failure Syndromes. Int J Mol Sci 21, 4672. https://doi.org/10.3390/ijms21134672
11. Bezzerri, V., Lentini, L., Api, M., Busilacchi, E.M., Cavalieri, V., Pomilio, A., Diomede, F., Pegoraro, A., Cesaro, S., Poloni, A., Pace, A., Trubiani, O., Lippi, G., Pibiri, I., Cipolli, M., 2022. Novel Translational Read-through-Inducing Drugs as a Therapeutic Option for Shwachman-Diamond Syndrome. Biomedicines 10, 886.

https://doi.org/10.3390/biomedicines10040886

12. Bladen, C.L., Salgado, D., Monges, S., Foncuberta, M.E., Kekou, K., Kosma, K., Dawkins, H., Lamont, L., Roy, A.J., Chamova, T., Guergueltcheva, V., Chan, S., Korngut, L., Campbell, C., Dai, Y., Wang, J., Barišić, N., Brabec, P., Lahdetie, J., Walter, M.C., Schreiber-Katz, O., Karcagi, V., Garami, M., Viswanathan, V., Bayat, F., Buccella, F., Kimura, E., Koeks, Z., van den Bergen, J.C., Rodrigues, M., Roxburgh, R., Lusakowska, A., Kostera-Pruszczyk, A., Zimowski, J., Santos, R., Neagu, E., Artemieva, S., Rasic, V.M., Vojinovic, D., Posada, M., Bloetzer, C., Jeannet, P.-Y., Joncourt, F., Díaz-Manera, J., Gallardo, E., Karaduman, A.A., Topaloğlu, H., El Sherif, R., Stringer, A., Shatillo, A.V., Martin, A.S., Peay, H.L., Bellgard, M.I., Kirschner, J., Flanigan, K.M., Straub, V., Bushby, K., Verschuuren, J., Aartsma-Rus, A., Béroud, C., Lochmüller, H., 2015. The TREAT-NMD DMD Global Database: analysis of more than 7,000 Duchenne muscular dystrophy mutations. Hum Mutat 36, 395–402. https://doi.org/10.1002/humu.22758
13. Bonetti, B., Fu, L., Moon, J., Bedwell, D.M., 1995. The efficiency of translation termination is determined by a synergistic interplay between upstream and downstream sequences in Saccharomyces cerevisiae. J Mol Biol 251, 334–345. https://doi.org/10.1006/jmbi.1995.0438
14. Boycott, K.M., Rath, A., Chong, J.X., Hartley, T., Alkuraya, F.S., Baynam, G., Brookes, A.J., Brudno, M., Carracedo, A., den Dunnen, J.T., Dyke, S.O.M., Estivill, X., Goldblatt, J., Gonthier, C., Groft, S.C., Gut, I., Hamosh, A., Hieter, P., Höhn, S., Hurles, M.E., Kaufmann, P., Knoppers, B.M., Krischer, J.P., Macek, M., Matthijs, G., Olry, A., Parker, S., Paschall, J., Philippakis, A.A., Rehm, H.L., Robinson, P.N., Sham, P.-C., Stefanov, R., Taruscio, D., Unni, D., Vanstone, M.R., Zhang, F., Brunner, H., Bamshad, M.J., Lochmüller, H., 2017. International Cooperation to Enable the Diagnosis of All Rare Genetic Diseases. Am J Hum Genet 100, 695–705. https://doi.org/10.1016/j.ajhg.2017.04.003
15. Brasell, E.J., Chu, L.L., Akpa, M.M., Eshkar-Oren, I., Alroy, I., Corsini, R., Gilfix, B.M., Yamanaka, Y., Huertas, P., Goodyer, P., 2019. The novel aminoglycoside, ELX-02, permits CTNSW138X translational read-through and restores lysosomal cystine efflux in cystinosis. PLoS One 14, e0223954. https://doi.org/10.1371/journal.pone.0223954
16. Bühler, M., Steiner, S., Mohn, F., Paillusson, A., Mühlemann, O., 2006. EJC-independent degradation of nonsense immunoglobulin-mu mRNA depends on 3' UTR length. Nat Struct Mol Biol 13, 462–464. https://doi.org/10.1038/nsmb1081
17. Burke, J.F., Mogg, A.E., 1985. Suppression of a nonsense mutation in mammalian cells in vivo by the aminoglycoside antibiotics G-418 and paromomycin. Nucleic Acids Res 13, 6265–6272. https://doi.org/10.1093/nar/13.17.6265

18. Bushby, K., Finkel, R., Birnkrant, D.J., Case, L.E., Clemens, P.R., Cripe, L., Kaul, A., Kinnett, K., McDonald, C., Pandya, S., Poysky, J., Shapiro, F., Tomezsko, J., Constantin, C., DMD Care Considerations Working Group, 2010. Diagnosis and management of Duchenne muscular dystrophy, part 2: implementation of multidisciplinary care. Lancet Neurol 9, 177–189. https://doi.org/10.1016/S1474-4422(09)70272-8
19. C, W., B, R., F, H., K, Y., A, J., 2020. Poly(A)-Binding Protein Regulates the Efficiency of Translation Termination. Cell reports 33. https://doi.org/10.1016/j.celrep.2020.108399
20. Calvo, S.E., Pagliarini, D.J., Mootha, V.K., 2009. Upstream open reading frames cause widespread reduction of protein expression and are polymorphic among humans. Proc Natl Acad Sci U S A 106, 7507–7512. https://doi.org/10.1073/pnas.0810916106
21. Carnes, J., Jacobson, M., Leinwand, L., Yarus, M., 2003. Stop codon suppression via inhibition of eRF1 expression. RNA 9, 648–653. https://doi.org/10.1261/rna.5280103
22. Clarke, L.A., Awatade, N.T., Felício, V.M., Silva, I.A., Calucho, M., Pereira, L., Azevedo, P., Cavaco, J., Barreto, C., Bertuzzo, C., Gartner, S., Beekman, J., Amaral, M.D., 2019. The effect of premature termination codon mutations on CFTR mRNA abundance in human nasal epithelium and intestinal organoids: a basis for read-through therapies in cystic fibrosis. Hum Mutat 40, 326–334. https://doi.org/10.1002/humu.23692
23. Cohn, R.D., Campbell, K.P., 2000. Molecular basis of muscular dystrophies. Muscle Nerve 23, 1456–1471. https://doi.org/10.1002/1097-4598(200010)23:10<1456::aid-mus2>3.0.co;2-t
24. Colombo, M., Karousis, E.D., Bourquin, J., Bruggmann, R., Mühlemann, O., 2017. Transcriptome-wide identification of NMD-targeted human mRNAs reveals extensive redundancy between SMG6- and SMG7-mediated degradation pathways. RNA 23, 189–201. https://doi.org/10.1261/rna.059055.116
25. Corrao, F., Zizzo, M.G., Tutone, M., Melfi, R., Fiduccia, I., Carollo, P.S., Leonardo, A.D., Caldara, G., Perriera, R., Pace, A., Belmonte, B., Sammataro, S., Pibiri, I., Lentini, L., 2022. Nonsense codons suppression. An acute toxicity study of three optimized TRIDs in murine model, safety and tolerability evaluation. Biomed Pharmacother 156, 113886. https://doi.org/10.1016/j.biopha.2022.113886
26. Cridge, A.G., Crowe-McAuliffe, C., Mathew, S.F., Tate, W.P., 2018. Eukaryotic translational termination efficiency is influenced by the 3' nucleotides within the ribosomal mRNA channel. Nucleic Acids Res 46, 1927–1944. https://doi.org/10.1093/nar/gkx1315
27. Dabrowski, M., Bukowy-Bieryllo, Z., Zietkiewicz, E., 2015. Translational readthrough potential of natural termination codons in eucaryotes--The impact of RNA sequence. RNA

Biol 12, 950–958. https://doi.org/10.1080/15476286.2015.1068497

28. Degli Esposti, M., Tour, J., Ouasti, S., Ivanova, S., Matarrese, P., Malorni, W., Khosravi-Far, R., 2009. Fas death receptor enhances endocytic membrane traffic converging into the Golgi region. Mol Biol Cell 20, 600–615. https://doi.org/10.1091/mbc.e08-09-0925
29. Du, M., Liu, X., Welch, E.M., Hirawat, S., Peltz, S.W., Bedwell, D.M., 2008. PTC124 is an orally bioavailable compound that promotes suppression of the human CFTR-G542X nonsense allele in a CF mouse model. Proc Natl Acad Sci U S A 105, 2064–2069. https://doi.org/10.1073/pnas.0711795105
30. Duan, D., Goemans, N., Takeda, S., Mercuri, E., Aartsma-Rus, A., 2021. Duchenne muscular dystrophy. Nat Rev Dis Primers 7, 13. https://doi.org/10.1038/s41572-021-00248-3
31. Durand, S., Lykke-Andersen, J., 2013. Nonsense-mediated mRNA decay occurs during eIF4F-dependent translation in human cells. Nat Struct Mol Biol 20, 702–709. https://doi.org/10.1038/nsmb.2575
32. Emery, A.E.H., 2002. The muscular dystrophies. Lancet 359, 687–695. https://doi.org/10.1016/S0140-6736(02)07815-7
33. Ervasti, J.M., Sonnemann, K.J., 2008. Biology of the striated muscle dystrophin-glycoprotein complex. Int Rev Cytol 265, 191–225. https://doi.org/10.1016/S0074-7696(07)65005-0
34. Fernández-Costa, J.M., Fernández-Garibay, X., Velasco-Mallorquí, F., Ramón-Azcón, J., 2021. Bioengineered in vitro skeletal muscles as new tools for muscular dystrophies preclinical studies. J Tissue Eng 12, 2041731420981339. https://doi.org/10.1177/2041731420981339
35. Fiduccia, I., Corrao, F., Zizzo, M.G., Perriera, R., Genovese, F., Vitale, E., Ricci, D., Melfi, R., Tutone, M., Pace, A., Lentini, L., Pibiri, I., 2024. Promoting Translational Readthrough of Nonsense Mutations in Cystic Fibrosis Mouse Model: Assessing the Biodistribution and Efficacy of the NV848 1,2,4-Oxadiazole Compound for the Rescue of the CFTR protein Expression. Molecular Therapy S1525001624006889. https://doi.org/10.1016/j.ymthe.2024.10.028
36. Firth, A.E., Wills, N.M., Gesteland, R.F., Atkins, J.F., 2011. Stimulation of stop codon readthrough: frequent presence of an extended 3’ RNA structural element. Nucleic Acids Res 39, 6679–6691. https://doi.org/10.1093/nar/gkr224
37. Floquet, C., Hatin, I., Rousset, J.-P., Bidou, L., 2012. Statistical analysis of readthrough levels for nonsense mutations in mammalian cells reveals a major determinant of response to gentamicin. PLoS Genet 8, e1002608. https://doi.org/10.1371/journal.pgen.1002608
38. Frischmeyer, P.A., Dietz, H.C., 1999. Nonsense-mediated mRNA decay in health and disease.

Hum Mol Genet 8, 1893–1900. https://doi.org/10.1093/hmg/8.10.1893

39. Frolova, L.Y., Tsivkovskii, R.Y., Sivolobova, G.F., Oparina, N.Y., Serpinsky, O.I., Blinov, V.M., Tatkov, S.I., Kisselev, L.L., 1999. Mutations in the highly conserved GGQ motif of class 1 polypeptide release factors abolish ability of human eRF1 to trigger peptidyl-tRNA hydrolysis. RNA 5, 1014–1020. https://doi.org/10.1017/s135583829999043x
40. Gámez-Díaz, L., August, D., Stepensky, P., Revel-Vilk, S., Seidel, M.G., Noriko, M., Morio, T., Worth, A.J.J., Blessing, J., Van de Veerdonk, F., Feuchtinger, T., Kanariou, M., Schmitt-Graeff, A., Jung, S., Seneviratne, S., Burns, S., Belohradsky, B.H., Rezaei, N., Bakhtiar, S., Speckmann, C., Jordan, M., Grimbacher, B., 2016. The extended phenotype of LPS-responsive beige-like anchor protein (LRBA) deficiency. J Allergy Clin Immunol 137, 223–230. https://doi.org/10.1016/j.jaci.2015.09.025
41. Gebauer, D., Li, J., Jogl, G., Shen, Y., Myszka, D.G., Tong, L., 2004. Crystal structure of the PH-BEACH domains of human LRBA/BGL. Biochemistry 43, 14873–14880. https://doi.org/10.1021/bi049498y
42. Ghelfi, M.D., Bhat, S.Y., Li, H., Cooperman, B.S., 2023. A High-Throughput Assay for In Vitro Determination of Release Factor-Dependent Peptide Release from a Pretermination Complex by Fluorescence Anisotropy-Application to Nonsense Suppressor Screening and Mechanistic Studies. Biomolecules 13, 242. https://doi.org/10.3390/biom13020242
43. Gutierrez, M.G., Munafó, D.B., Berón, W., Colombo, M.I., 2004. Rab7 is required for the normal progression of the autophagic pathway in mammalian cells. J Cell Sci 117, 2687–2697. https://doi.org/10.1242/jcs.01114
44. Hansen, T.E., Johansen, T., 2011. Following autophagy step by step. BMC Biol 9, 39. https://doi.org/10.1186/1741-7007-9-39
45. Hauryliuk, V., Zavialov, A., Kisselev, L., Ehrenberg, M., 2006. Class-1 release factor eRF1 promotes GTP binding by class-2 release factor eRF3. Biochimie 88, 747–757. https://doi.org/10.1016/j.biochi.2006.06.001
46. Hellen, C.U.T., 2018. Translation Termination and Ribosome Recycling in Eukaryotes. Cold Spring Harb Perspect Biol 10, a032656. https://doi.org/10.1101/cshperspect.a032656
47. Hirawat, S., Welch, E.M., Elfring, G.L., Northcutt, V.J., Paushkin, S., Hwang, S., Leonard, E.M., Almstead, N.G., Ju, W., Peltz, S.W., Miller, L.L., 2007. Safety, tolerability, and pharmacokinetics of PTC124, a nonaminoglycoside nonsense mutation suppressor, following single- and multiple-dose administration to healthy male and female adult volunteers. J Clin Pharmacol 47, 430–444. https://doi.org/10.1177/0091270006297140
48. Hobbie, S.N., Akshay, S., Kalapala, S.K., Bruell, C.M., Shcherbakov, D., Böttger, E.C., 2008.

Genetic analysis of interactions with eukaryotic rRNA identify the mitoribosome as target in aminoglycoside ototoxicity. Proc Natl Acad Sci U S A 105, 20888–20893. https://doi.org/10.1073/pnas.0811258106

49. Hoffman, E.P., Brown, R.H., Kunkel, L.M., 1987. Dystrophin: the protein product of the Duchenne muscular dystrophy locus. Cell 51, 919–928. https://doi.org/10.1016/0092-8674(87)90579-4
50. Hogg, J.R., Goff, S.P., 2010. Upf1 senses 3'UTR length to potentiate mRNA decay. Cell 143, 379–389. https://doi.org/10.1016/j.cell.2010.10.005
51. Hoshino, S., Imai, M., Kobayashi, T., Uchida, N., Katada, T., 1999. The eukaryotic polypeptide chain releasing factor (eRF3/GSPT) carrying the translation termination signal to the 3'-Poly(A) tail of mRNA. Direct association of erf3/GSPT with polyadenylate-binding protein. J Biol Chem 274, 16677–16680. https://doi.org/10.1074/jbc.274.24.16677
52. Howard, M., Frizzell, R.A., Bedwell, D.M., 1996. Aminoglycoside antibiotics restore CFTR function by overcoming premature stop mutations. Nat Med 2, 467–469. https://doi.org/10.1038/nm0496-467
53. Huang, S., Bhattacharya, A., Ghelfi, M.D., Li, H., Fritsch, C., Chenoweth, D.M., Goldman, Y.E., Cooperman, B.S., 2022. Ataluren binds to multiple protein synthesis apparatus sites and competitively inhibits release factor-dependent termination. Nat Commun 13, 2413. https://doi.org/10.1038/s41467-022-30080-6
54. Jiang, M., Karasawa, T., Steyger, P.S., 2017. Aminoglycoside-Induced Cochleotoxicity: A Review. Front Cell Neurosci 11, 308. https://doi.org/10.3389/fncel.2017.00308
55. Karousis, E.D., Mühlemann, O., 2022. The broader sense of nonsense. Trends Biochem Sci 47, 921–935. https://doi.org/10.1016/j.tibs.2022.06.003
56. Karousis, E.D., Mühlemann, O., 2019. Nonsense-Mediated mRNA Decay Begins Where Translation Ends. Cold Spring Harb Perspect Biol 11, a032862. https://doi.org/10.1101/cshperspect.a032862
57. Karp, G.M., Hwang, S., Chen, G., Almstead, N.G., Moon, Y.-C., 2006. 1,2,4-oxadiazole benzoic acid compounds and their use for nonsense suppression and the treatment of disease. US6992096B2.
58. Kayali, R., Ku, J.-M., Khitrov, G., Jung, M.E., Prikhodko, O., Bertoni, C., 2012. Read-through compound 13 restores dystrophin expression and improves muscle function in the mdx mouse model for Duchenne muscular dystrophy. Hum Mol Genet 21, 4007–4020. https://doi.org/10.1093/hmg/dds223
59. Keeling, K.M., Wang, D., Conard, S.E., Bedwell, D.M., 2012. Suppression of premature

termination codons as a therapeutic approach. Crit Rev Biochem Mol Biol 47, 444–463. https://doi.org/10.3109/10409238.2012.694846

60. Kennedy, A., Waters, E., Rowshanravan, B., Hinze, C., Williams, C., Janman, D., Fox, T.A., Booth, C., Pesenacker, A.M., Halliday, N., Soskic, B., Kaur, S., Qureshi, O.S., Morris, E.C., Ikemizu, S., Paluch, C., Huo, J., Davis, S.J., Boucrot, E., Walker, L.S.K., Sansom, D.M., 2022. Differences in CD80 and CD86 transendocytosis reveal CD86 as a key target for CTLA-4 immune regulation. Nat Immunol 23, 1365–1378. https://doi.org/10.1038/s41590-022-01289-w
61. Kerem, E., Konstan, M.W., De Boeck, K., Accurso, F.J., Sermet-Gaudelus, I., Wilschanski, M., Elborn, J.S., Melotti, P., Bronsveld, I., Fajac, I., Malfroot, A., Rosenbluth, D.B., Walker, P.A., McColley, S.A., Knoop, C., Quattrucci, S., Rietschel, E., Zeitlin, P.L., Barth, J., Elfring, G.L., Welch, E.M., Branstrom, A., Spiegel, R.J., Peltz, S.W., Ajayi, T., Rowe, S.M., Cystic Fibrosis Ataluren Study Group, 2014. Ataluren for the treatment of nonsense-mutation cystic fibrosis: a randomised, double-blind, placebo-controlled phase 3 trial. Lancet Respir Med 2, 539–547. https://doi.org/10.1016/S2213-2600(14)70100-6
62. Kk, M., Cm, B., Me, D., Mj, B., Wp, T., 1995. Translational termination efficiency in mammals is influenced by the base following the stop codon. Proceedings of the National Academy of Sciences of the United States of America 92. https://doi.org/10.1073/pnas.92.12.5431
63. Kmth, R., M, T.-G., 2020. Genetic Modifiers and Rare Mendelian Disease. Genes 11. https://doi.org/10.3390/genes11030239
64. Kong, C., Ito, K., Walsh, M.A., Wada, M., Liu, Y., Kumar, S., Barford, D., Nakamura, Y., Song, H., 2004. Crystal structure and functional analysis of the eukaryotic class II release factor eRF3 from S. pombe. Mol Cell 14, 233–245. https://doi.org/10.1016/s1097-2765(04)00206-0
65. Kong, R., Ma, J., Hwang, S., Goodwin, E., Northcutt, V., Babiak, J., Almstead, N., McIntosh, J., 2020a. Metabolism and Disposition of Ataluren after Oral Administration to Mice, Rats, Dogs, and Humans. Drug Metab Dispos 48, 317–325. https://doi.org/10.1124/dmd.119.089391
66. Kong, R., Ma, J., Hwang, S., Moon, Y.-C., Welch, E.M., Weetall, M., Colacino, J.M., Almstead, N., Babiak, J., Goodwin, E., 2020b. In vitro metabolism, reaction phenotyping, enzyme kinetics, CYP inhibition and induction potential of ataluren. Pharmacol Res Perspect 8, e00576. https://doi.org/10.1002/prp2.576
67. Kozlov, G., Gehring, K., 2010. Molecular basis of eRF3 recognition by the MLLE domain of

poly(A)-binding protein. PLoS One 5, e10169. https://doi.org/10.1371/journal.pone.0010169

68. Lee, K.-H., Feig, C., Tchikov, V., Schickel, R., Hallas, C., Schütze, S., Peter, M.E., Chan, A.C., 2006. The role of receptor internalization in CD95 signaling. EMBO J 25, 1009–1023. https://doi.org/10.1038/sj.emboj.7601016
69. Leroy, C., Spelier, S., Essonghe, N.C., Poix, V., Kong, R., Gizzi, P., Bourban, C., Amand, S., Bailly, C., Guilbert, R., Hannebique, D., Persoons, P., Arhant, G., Prévotat, A., Reix, P., Hubert, D., Gérardin, M., Chamaillard, M., Prevarskaya, N., Rebuffat, S., Shapovalov, G., Beekman, J., Lejeune, F., 2023. Use of 2,6-diaminopurine as a potent suppressor of UGA premature stop codons in cystic fibrosis. Mol Ther 31, 970–985. https://doi.org/10.1016/j.ymthe.2023.01.014
70. Leubitz, A., Frydman-Marom, A., Sharpe, N., van Duzer, J., Campbell, K.C.M., Vanhoutte, F., 2019. Safety, Tolerability, and Pharmacokinetics of Single Ascending Doses of ELX-02, a Potential Treatment for Genetic Disorders Caused by Nonsense Mutations, in Healthy Volunteers. Clin Pharmacol Drug Dev 8, 984–994. https://doi.org/10.1002/cpdd.647
71. Linde, L., Boelz, S., Nissim-Rafinia, M., Oren, Y.S., Wilschanski, M., Yaacov, Y., Virgilis, D., Neu-Yilik, G., Kulozik, A.E., Kerem, E., Kerem, B., 2007. Nonsense-mediated mRNA decay affects nonsense transcript levels and governs response of cystic fibrosis patients to gentamicin. J Clin Invest 117, 683–692. https://doi.org/10.1172/JCI28523
72. Lo, B., Zhang, K., Lu, W., Zheng, L., Zhang, Q., Kanellopoulou, C., Zhang, Y., Liu, Z., Fritz, J.M., Marsh, R., Husami, A., Kissell, D., Nortman, S., Chaturvedi, V., Haines, H., Young, L.R., Mo, J., Filipovich, A.H., Bleesing, J.J., Mustillo, P., Stephens, M., Rueda, C.M., Chougnet, C.A., Hoebe, K., McElwee, J., Hughes, J.D., Karakoc-Aydiner, E., Matthews, H.F., Price, S., Su, H.C., Rao, V.K., Lenardo, M.J., Jordan, M.B., 2015. AUTOIMMUNE DISEASE. Patients with LRBA deficiency show CTLA4 loss and immune dysregulation responsive to abatacept therapy. Science 349, 436–440. https://doi.org/10.1126/science.aaa1663
73. Loenarz, C., Sekirnik, R., Thalhammer, A., Ge, W., Spivakovsky, E., Mackeen, M.M., McDonough, M.A., Cockman, M.E., Kessler, B.M., Ratcliffe, P.J., Wolf, A., Schofield, C.J., 2014. Hydroxylation of the eukaryotic ribosomal decoding center affects translational accuracy. Proc Natl Acad Sci U S A 111, 4019–4024. https://doi.org/10.1073/pnas.1311750111
74. Lopez-Herrera, G., Tampella, G., Pan-Hammarström, Q., Herholz, P., Trujillo-Vargas, C.M., Phadwal, K., Simon, A.K., Moutschen, M., Etzioni, A., Mory, A., Srugo, I., Melamed, D., Hultenby, K., Liu, C., Baronio, M., Vitali, M., Philippet, P., Dideberg, V., Aghamohammadi,

A., Rezaei, N., Enright, V., Du, L., Salzer, U., Eibel, H., Pfeifer, D., Veelken, H., Stauss, H., Lougaris, V., Plebani, A., Gertz, E.M., Schäffer, A.A., Hammarström, L., Grimbacher, B., 2012. Deleterious mutations in LRBA are associated with a syndrome of immune deficiency and autoimmunity. Am J Hum Genet 90, 986–1001. https://doi.org/10.1016/j.ajhg.2012.04.015

75. Lopez-Novoa, J.M., Quiros, Y., Vicente, L., Morales, A.I., Lopez-Hernandez, F.J., 2011. New insights into the mechanism of aminoglycoside nephrotoxicity: an integrative point of view. Kidney Int 79, 33–45. https://doi.org/10.1038/ki.2010.337
76. Lubamba, B., Dhooghe, B., Noel, S., Leal, T., 2012. Cystic fibrosis: insight into CFTR pathophysiology and pharmacotherapy. Clin Biochem 45, 1132–1144. https://doi.org/10.1016/j.clinbiochem.2012.05.034
77. Mangodt, T.C., Vanden Driessche, K., Norga, K.K., Moes, N., De Bruyne, M., Haerynck, F., Bordon, V., Jansen, A.C., Jonckheere, A.I., 2023. Central nervous system manifestations of LRBA deficiency: case report of two siblings and literature review. BMC Pediatr 23, 353. https://doi.org/10.1186/s12887-023-04182-z
78. Mantsyzov, A.B., Ivanova, E.V., Birdsall, B., Alkalaeva, E.Z., Kryuchkova, P.N., Kelly, G., Frolova, L.Y., Polshakov, V.I., 2010. NMR solution structure and function of the C-terminal domain of eukaryotic class 1 polypeptide chain release factor. FEBS J 277, 2611–2627. https://doi.org/10.1111/j.1742-464X.2010.07672.x
79. Manuvakhova, M., Keeling, K., Bedwell, D.M., 2000. Aminoglycoside antibiotics mediate context-dependent suppression of termination codons in a mammalian translation system. RNA 6, 1044–1055. https://doi.org/10.1017/s1355838200000716
80. Maquat, L.E., Tarn, W.-Y., Isken, O., 2010. The pioneer round of translation: features and functions. Cell 142, 368–374. https://doi.org/10.1016/j.cell.2010.07.022
81. Martínez Jaramillo, C., Trujillo-Vargas, C.M., 2018. LRBA in the endomembrane system. Colomb Med (Cali) 49, 236–243. https://doi.org/10.25100/cm.v49i2.3802
82. Martins-Dias, P., Romão, L., 2021. Nonsense suppression therapies in human genetic diseases. Cell Mol Life Sci 78, 4677–4701. https://doi.org/10.1007/s00018-021-03809-7
83. Matheisl, S., Berninghausen, O., Becker, T., Beckmann, R., 2015. Structure of a human translation termination complex. Nucleic Acids Res 43, 8615–8626. https://doi.org/10.1093/nar/gkv909
84. McHugh, D.R., Cotton, C.U., Hodges, C.A., 2020. Synergy between Readthrough and Nonsense Mediated Decay Inhibition in a Murine Model of Cystic Fibrosis Nonsense Mutations. Int J Mol Sci 22, 344. https://doi.org/10.3390/ijms22010344

85. Mendell, J.R., Shilling, C., Leslie, N.D., Flanigan, K.M., al-Dahhak, R., Gastier-Foster, J., Kneile, K., Dunn, D.M., Duval, B., Aoyagi, A., Hamil, C., Mahmoud, M., Roush, K., Bird, L., Rankin, C., Lilly, H., Street, N., Chandrasekar, R., Weiss, R.B., 2012. Evidence-based path to newborn screening for Duchenne muscular dystrophy. Ann Neurol 71, 304–313. https://doi.org/10.1002/ana.23528
86. Meng, W., Dong, Y., Liu, J., Wang, Z., Zhong, X., Chen, R., Zhou, H., Lin, M., Jiang, L., Gao, F., Xu, T., Chen, Q., Zeng, X., 2009. A clinical evaluation of amlexanox oral adhesive pellicles in the treatment of recurrent aphthous stomatitis and comparison with amlexanox oral tablets: a randomized, placebo controlled, blinded, multicenter clinical trial. Trials 10, 30. https://doi.org/10.1186/1745-6215-10-30
87. Mercuri, E., Bönnemann, C.G., Muntoni, F., 2019. Muscular dystrophies. Lancet 394, 2025–2038. https://doi.org/10.1016/S0140-6736(19)32910-1
88. Merrick, L., Campbell, A., Muenchrath, D., Fei, S.-Z., Beavis, W., 2023. Chapter 9: Mutations and Variation.
89. Metze, S., Herzog, V.A., Ruepp, M.-D., Mühlemann, O., 2013. Comparison of EJC-enhanced and EJC-independent NMD in human cells reveals two partially redundant degradation pathways. RNA 19, 1432–1448. https://doi.org/10.1261/rna.038893.113
90. Mitkevich, V.A., Kononenko, A.V., Petrushanko, I.Y., Yanvarev, D.V., Makarov, A.A., Kisselev, L.L., 2006. Termination of translation in eukaryotes is mediated by the quaternary eRF1*eRF3*GTP*Mg2+ complex. The biological roles of eRF3 and prokaryotic RF3 are profoundly distinct. Nucleic Acids Res 34, 3947–3954. https://doi.org/10.1093/nar/gkl549
91. Monaghan, L., Longman, D., Cáceres, J.F., 2023. Translation-coupled mRNA quality control mechanisms. EMBO J 42, e114378. https://doi.org/10.15252/embj.2023114378
92. Morais, P., Zhang, R., Yu, Y.-T., 2024. Therapeutic Nonsense Suppression Modalities: From Small Molecules to Nucleic Acid-Based Approaches. Biomedicines 12, 1284. https://doi.org/10.3390/biomedicines12061284
93. Mort, M., Ivanov, D., Cooper, D.N., Chuzhanova, N.A., 2008. A meta-analysis of nonsense mutations causing human genetic disease. Hum Mutat 29, 1037–1047. https://doi.org/10.1002/humu.20763
94. Muhs, M., Hilal, T., Mielke, T., Skabkin, M.A., Sanbonmatsu, K.Y., Pestova, T.V., Spahn, C.M.T., 2015. Cryo-EM of ribosomal 80S complexes with termination factors reveals the translocated cricket paralysis virus IRES. Mol Cell 57, 422–432. https://doi.org/10.1016/j.molcel.2014.12.016
95. Nallamilli, B.R.R., Chaubey, A., Valencia, C.A., Stansberry, L., Behlmann, A.M., Ma, Z.,

Mathur, A., Shenoy, S., Ganapathy, V., Jagannathan, L., Ramachander, V., Ferlini, A., Bean, L., Hegde, M., 2021. A single NGS-based assay covering the entire genomic sequence of the DMD gene facilitates diagnostic and newborn screening confirmatory testing. Hum Mutat 42, 626–638. https://doi.org/10.1002/humu.24191

96. Nasif, S., Contu, L., Mühlemann, O., 2018. Beyond quality control: The role of nonsense-mediated mRNA decay (NMD) in regulating gene expression. Semin Cell Dev Biol 75, 78–87. https://doi.org/10.1016/j.semcdb.2017.08.053
97. Neri, M., Rossi, R., Trabanelli, C., Mauro, A., Selvatici, R., Falzarano, M.S., Spedicato, N., Margutti, A., Rimessi, P., Fortunato, F., Fabris, M., Gualandi, F., Comi, G., Tedeschi, S., Seia, M., Fiorillo, C., Traverso, M., Bruno, C., Giardina, E., Piemontese, M.R., Merla, G., Cau, M., Marica, M., Scuderi, C., Borgione, E., Tessa, A., Astrea, G., Santorelli, F.M., Merlini, L., Mora, M., Bernasconi, P., Gibertini, S., Sansone, V., Mongini, T., Berardinelli, A., Pini, A., Liguori, R., Filosto, M., Messina, S., Vita, Gianluca, Toscano, A., Vita, Giuseppe, Pane, M., Servidei, S., Pegoraro, E., Bello, L., Travaglini, L., Bertini, E., D'Amico, A., Ergoli, M., Politano, L., Torella, A., Nigro, V., Mercuri, E., Ferlini, A., 2020. The Genetic Landscape of Dystrophin Mutations in Italy: A Nationwide Study. Front Genet 11, 131. https://doi.org/10.3389/fgene.2020.00131
98. Neu-Yilik, G., Raimondeau, E., Eliseev, B., Yeramala, L., Amthor, B., Deniaud, A., Huard, K., Kerschgens, K., Hentze, M.W., Schaffitzel, C., Kulozik, A.E., 2017. Dual function of UPF3B in early and late translation termination. EMBO J 36, 2968–2986. https://doi.org/10.15252/embj.201797079
99. Oren, Y.S., Pranke, I.M., Kerem, B., Sermet-Gaudelus, I., 2017. The suppression of premature termination codons and the repair of splicing mutations in CFTR. Curr Opin Pharmacol 34, 125–131. https://doi.org/10.1016/j.coph.2017.09.017
100. Patel, R., Barker, J., ElShaer, A., 2020. Pharmaceutical Excipients and Drug Metabolism: A Mini-Review. Int J Mol Sci 21, 8224. https://doi.org/10.3390/ijms21218224
101. Perriera, R., Vitale, E., Pibiri, I., Carollo, P.S., Ricci, D., Corrao, F., Fiduccia, I., Melfi, R., Zizzo, M.G., Tutone, M., Pace, A., Lentini, L., 2023. Readthrough Approach Using NV Translational Readthrough-Inducing Drugs (TRIDs): A Study of the Possible Off-Target Effects on Natural Termination Codons (NTCs) on TP53 and Housekeeping Gene Expression. Int J Mol Sci 24, 15084. https://doi.org/10.3390/ijms242015084
102. Petrof, B.J., Shrager, J.B., Stedman, H.H., Kelly, A.M., Sweeney, H.L., 1993. Dystrophin protects the sarcolemma from stresses developed during muscle contraction. Proc Natl Acad Sci U S A 90, 3710–3714. https://doi.org/10.1073/pnas.90.8.3710

103. Pibiri, I., Melfi, R., Tutone, M., Di Leonardo, A., Pace, A., Lentini, L., 2020. Targeting Nonsense: Optimization of 1,2,4-Oxadiazole TRIDs to Rescue CFTR Expression and Functionality in Cystic Fibrosis Cell Model Systems. Int J Mol Sci 21, 6420. https://doi.org/10.3390/ijms21176420

104. Piccionello, A.P., Pace, A., Buscemi, S., 2017. Rearrangements of 1,2,4-Oxadiazole: "One Ring to Rule Them All." Chem Heterocycl Comp 53, 936–947. https://doi.org/10.1007/s10593-017-2154-1

105. Poncová, K., Wagner, S., Jansen, M.E., Beznosková, P., Gunišová, S., Herrmannová, A., Zeman, J., Dong, J., Valášek, L.S., 2019. uS3/Rps3 controls fidelity of translation termination and programmed stop codon readthrough in co-operation with eIF3. Nucleic Acids Res 47, 11326–11343. https://doi.org/10.1093/nar/gkz929

106. Potapova, N.A., 2022. Nonsense Mutations in Eukaryotes. Biochemistry (Mosc) 87, 400–412. https://doi.org/10.1134/S0006297922050029

107. Qureshi, O.S., Kaur, S., Hou, T.Z., Jeffery, L.E., Poulter, N.S., Briggs, Z., Kenefeck, R., Willox, A.K., Royle, S.J., Rappoport, J.Z., Sansom, D.M., 2012. Constitutive clathrin-mediated endocytosis of CTLA-4 persists during T cell activation. J Biol Chem 287, 9429–9440. https://doi.org/10.1074/jbc.M111.304329

108. Qureshi, O.S., Zheng, Y., Nakamura, K., Attridge, K., Manzotti, C., Schmidt, E.M., Baker, J., Jeffery, L.E., Kaur, S., Briggs, Z., Hou, T.Z., Futter, C.E., Anderson, G., Walker, L.S.K., Sansom, D.M., 2011. Trans-endocytosis of CD80 and CD86: a molecular basis for the cell-extrinsic function of CTLA-4. Science 332, 600–603. https://doi.org/10.1126/science.1202947

109. Rendic, S.P., 2021. Metabolism and interactions of Ivermectin with human cytochrome P450 enzymes and drug transporters, possible adverse and toxic effects. Arch Toxicol 95, 1535–1546. https://doi.org/10.1007/s00204-021-03025-z

110. Ricotti, V., Mandy, W.P.L., Scoto, M., Pane, M., Deconinck, N., Messina, S., Mercuri, E., Skuse, D.H., Muntoni, F., 2016. Neurodevelopmental, emotional, and behavioural problems in Duchenne muscular dystrophy in relation to underlying dystrophin gene mutations. Dev Med Child Neurol 58, 77–84. https://doi.org/10.1111/dmcn.12922

111. Romanov, G.A., Sukhoverov, V.S., 2017. Arginine CGA codons as a source of nonsense mutations: a possible role in multivariant gene expression, control of mRNA quality, and aging. Mol Genet Genomics 292, 1013–1026. https://doi.org/10.1007/s00438-017-1328-y

112. Rufener, S.C., Mühlemann, O., 2013. eIF4E-bound mRNPs are substrates for

nonsense-mediated mRNA decay in mammalian cells. Nat Struct Mol Biol 20, 710–717. https://doi.org/10.1038/nsmb.2576

113. Ryter, S.W., Mizumura, K., Choi, A.M.K., 2014. The impact of autophagy on cell death modalities. Int J Cell Biol 2014, 502676. https://doi.org/10.1155/2014/502676

114. Saijo, T., Kuriki, H., Ashida, Y., Makino, H., Maki, Y., 1985. Mechanism of the action of amoxanox (AA-673), an orally active antiallergic agent. Int Arch Allergy Appl Immunol 78, 43–50. https://doi.org/10.1159/000233861

115. Salas-Marco, J., Bedwell, D.M., 2004. GTP hydrolysis by eRF3 facilitates stop codon decoding during eukaryotic translation termination. Mol Cell Biol 24, 7769–7778. https://doi.org/10.1128/MCB.24.17.7769-7778.2004

116. Sanz, J., von Känel, T., Schneider, M., Steiner, B., Schaller, A., Gallati, S., 2010. The CFTR frameshift mutation 3905insT and its effect at transcript and protein level. Eur J Hum Genet 18, 212–217. https://doi.org/10.1038/ejhg.2009.140

117. Shalev, M., Baasov, T., 2014. When Proteins Start to Make Sense: Fine-tuning Aminoglycosides for PTC Suppression Therapy. Medchemcomm 5, 1092–1105. https://doi.org/10.1039/C4MD00081A

118. Shao, S., Murray, J., Brown, A., Taunton, J., Ramakrishnan, V., Hegde, R.S., 2016. Decoding Mammalian Ribosome-mRNA States by Translational GTPase Complexes. Cell 167, 1229-1240.e15. https://doi.org/10.1016/j.cell.2016.10.046

119. Sigismund, S., Argenzio, E., Tosoni, D., Cavallaro, E., Polo, S., Di Fiore, P.P., 2008. Clathrin-mediated internalization is essential for sustained EGFR signaling but dispensable for degradation. Dev Cell 15, 209–219. https://doi.org/10.1016/j.devcel.2008.06.012

120. Singleton, R.S., Liu-Yi, P., Formenti, F., Ge, W., Sekirnik, R., Fischer, R., Adam, J., Pollard, P.J., Wolf, A., Thalhammer, A., Loenarz, C., Flashman, E., Yamamoto, A., Coleman, M.L., Kessler, B.M., Wappner, P., Schofield, C.J., Ratcliffe, P.J., Cockman, M.E., 2014. OGFOD1 catalyzes prolyl hydroxylation of RPS23 and is involved in translation control and stress granule formation. Proc Natl Acad Sci U S A 111, 4031–4036. https://doi.org/10.1073/pnas.1314482111

121. Song, H., Mugnier, P., Das, A.K., Webb, H.M., Evans, D.R., Tuite, M.F., Hemmings, B.A., Barford, D., 2000. The crystal structure of human eukaryotic release factor eRF1--mechanism of stop codon recognition and peptidyl-tRNA hydrolysis. Cell 100, 311–321. https://doi.org/10.1016/s0092-8674(00)80667-4

122. Starosta, A., Konieczny, P., 2021. Therapeutic aspects of cell signaling and communication in Duchenne muscular dystrophy. Cell Mol Life Sci 78, 4867–4891.

https://doi.org/10.1007/s00018-021-03821-x

123. Straub, V., Bittner, R.E., Léger, J.J., Voit, T., 1992. Direct visualization of the dystrophin network on skeletal muscle fiber membrane. J Cell Biol 119, 1183–1191. https://doi.org/10.1083/jcb.119.5.1183

124. Study Details | A Study of ELX-02 in Patients With Alport Syndrome | ClinicalTrials.gov [WWW Document], n.d. URL https://clinicaltrials.gov/study/NCT05448755?intr=ELX-02&rank=1 (accessed 9.24.24).

125. Taghizade, N., Babayeva, R., Kara, A., Karakus, I.S., Catak, M.C., Bulutoglu, A., Haskologlu, Z.S., Akay Haci, I., Tunakan Dalgic, C., Karabiber, E., Bilgic Eltan, S., Yorgun Altunbas, M., Sefer, A.P., Sezer, A., Kokcu Karadag, S.I., Arik, E., Karali, Z., Ozhan Kont, A., Tuzer, C., Karaman, S., Mersin, S.S., Kasap, N., Celik, E., Kocacik Uygun, D.F., Aydemir, S., Kiykim, A., Aydogmus, C., Ozek Yucel, E., Celmeli, F., Karatay, E., Bozkurtlar, E., Demir, S., Metin, A., Karaca, N.E., Kutukculer, N., Aksu, G., Guner, S.N., Keles, S., Reisli, I., Kendir Demirkol, Y., Arikoglu, T., Gulez, N., Genel, F., Kilic, S.S., Aytekin, C., Keskin, O., Yildiran, A., Ozcan, D., Altintas, D.U., Ardeniz, F.O., Dogu, E.F., Ikinciogullari, K.A., Karakoc-Aydiner, E., Ozen, A., Baris, S., 2023. Therapeutic modalities and clinical outcomes in a large cohort with LRBA deficiency and CTLA4 insufficiency. J Allergy Clin Immunol 152, 1634–1645. https://doi.org/10.1016/j.jaci.2023.08.004

126. Tate, W.P., Mannering, S.A., 1996. Three, four or more: the translational stop signal at length. Mol Microbiol 21, 213–219. https://doi.org/10.1046/j.1365-2958.1996.6391352.x

127. Taylor, P.J., Maroulis, S., Mullan, G.L., Pedersen, R.L., Baumli, A., Elakis, G., Piras, S., Walsh, C., Prósper-Gutiérrez, B., De La Puente-Alonso, F., Bell, C.G., Mowat, D.R., Johnston, H.M., Buckley, M.F., 2007. Measurement of the clinical utility of a combined mutation detection protocol in carriers of Duchenne and Becker muscular dystrophy. J Med Genet 44, 368–372. https://doi.org/10.1136/jmg.2006.047464

128. Tejedera-Villafranca, A., Montolio, M., Ramón-Azcón, J., Fernández-Costa, J.M., 2023. Mimicking sarcolemmal damagein vitro: a contractile 3D model of skeletal muscle for drug testing in Duchenne muscular dystrophy. Biofabrication 15. https://doi.org/10.1088/1758-5090/acfb3d

129. Tø, T., T, S., Ms, J., Mj, M., 2005. Biochemical analysis of the EJC reveals two new factors and a stable tetrameric protein core. RNA (New York, N.Y.) 11. https://doi.org/10.1261/rna.2155905

130. Tork, S., Hatin, I., Rousset, J.-P., Fabret, C., 2004. The major 5' determinant in stop codon read-through involves two adjacent adenines. Nucleic Acids Res 32, 415–421.

https://doi.org/10.1093/nar/gkh201

131. Translarna | European Medicines Agency (EMA) [WWW Document], 2014. URL https://www.ema.europa.eu/en/medicines/human/EPAR/translarna (accessed 9.24.24).

132. Tsuda, T., 2018. Clinical Manifestations and Overall Management Strategies for Duchenne Muscular Dystrophy. Methods Mol Biol 1687, 19–28. https://doi.org/10.1007/978-1-4939-7374-3_2

133. Vieira, E., Huwyler, J., Jolidon, S., Knoflach, F., Mutel, V., Wichmann, J., 2005. 9H-Xanthene-9-carboxylic acid [1,2,4]oxadiazol-3-yl- and (2H-tetrazol-5-yl)-amides as potent, orally available mGlu1 receptor enhancers. Bioorg Med Chem Lett 15, 4628–4631. https://doi.org/10.1016/j.bmcl.2005.05.135

134. Wagner, R.N., Wießner, M., Friedrich, A., Zandanell, J., Breitenbach-Koller, H., Bauer, J.W., 2023. Emerging Personalized Opportunities for Enhancing Translational Readthrough in Rare Genetic Diseases and Beyond. Int J Mol Sci 24, 6101. https://doi.org/10.3390/ijms24076101

135. Walter, P., Ron, D., 2011. The unfolded protein response: from stress pathway to homeostatic regulation. Science 334, 1081–1086. https://doi.org/10.1126/science.1209038

136. Wang, J.-W., Gamsby, J.J., Highfill, S.L., Mora, L.B., Bloom, G.C., Yeatman, T.J., Pan, T., Ramne, A.L., Chodosh, L.A., Cress, W.D., Chen, J., Kerr, W.G., 2004. Deregulated expression of LRBA facilitates cancer cell growth. Oncogene 23, 4089–4097. https://doi.org/10.1038/sj.onc.1207567

137. Wang, J.W., Howson, J., Haller, E., Kerr, W.G., 2001. Identification of a novel lipopolysaccharide-inducible gene with key features of both A kinase anchor proteins and chs1/beige proteins. J Immunol 166, 4586–4595. https://doi.org/10.4049/jimmunol.166.7.4586

138. Wee, P., Wang, Z., 2017. Epidermal Growth Factor Receptor Cell Proliferation Signaling Pathways. Cancers (Basel) 9, 52. https://doi.org/10.3390/cancers9050052

139. Welch, E.M., Barton, E.R., Zhuo, J., Tomizawa, Y., Friesen, W.J., Trifillis, P., Paushkin, S., Patel, M., Trotta, C.R., Hwang, S., Wilde, R.G., Karp, G., Takasugi, J., Chen, G., Jones, S., Ren, H., Moon, Y.-C., Corson, D., Turpoff, A.A., Campbell, J.A., Conn, M.M., Khan, A., Almstead, N.G., Hedrick, J., Mollin, A., Risher, N., Weetall, M., Yeh, S., Branstrom, A.A., Colacino, J.M., Babiak, J., Ju, W.D., Hirawat, S., Northcutt, V.J., Miller, L.L., Spatrick, P., He, F., Kawana, M., Feng, H., Jacobson, A., Peltz, S.W., Sweeney, H.L., 2007. PTC124 targets genetic disorders caused by nonsense mutations. Nature 447, 87–91. https://doi.org/10.1038/nature05756

140. Wilschanski, M., 2012. Class 1 CF Mutations. Front Pharmacol 3, 117. https://doi.org/10.3389/fphar.2012.00117

141. Xie, J., Talaska, A.E., Schacht, J., 2011. New developments in aminoglycoside therapy and ototoxicity. Hear Res 281, 28–37. https://doi.org/10.1016/j.heares.2011.05.008

142. Zhang, M., Yang, D., Gold, B., 2021. Origins of nonsense mutations in human tumor suppressor genes. Mutat Res 823, 111761. https://doi.org/10.1016/j.mrfmmm.2021.111761

143. Zhao, J., Kodippili, K., Yue, Y., Hakim, C.H., Wasala, L., Pan, X., Zhang, K., Yang, N.N., Duan, D., Lai, Y., 2016. Dystrophin contains multiple independent membrane-binding domains. Hum Mol Genet 25, 3647–3653. https://doi.org/10.1093/hmg/ddw210

144. Zhao, M., Ma, J., Li, M., Zhang, Y., Jiang, B., Zhao, X., Huai, C., Shen, L., Zhang, N., He, L., Qin, S., 2021. Cytochrome P450 Enzymes and Drug Metabolism in Humans. International Journal of Molecular Sciences 22, 12808. https://doi.org/10.3390/ijms222312808